eXPRESS Polymer Letters Vol.1, No.1 (2007) 1
Available online at www.expresspolymlett.com
DOI: 10.3144/expresspolymlett.2007.1

Preface

J. Karger-Kocsis[1], T. Czigány[2]*

[1]Institut für Verbundwerkstoffe GmbH (Institute for Composite Materials), Kaiserslautern University of Technology, Erwin Schrödinger Str. 58, D-67663 Kaiserslautern, Germany
[2]Department of Polymer Engineering, Budapest University of Technology and Economics, Műegyetem rkp. 3., H-1111 Budapest, Hungary

Dear Readers,

You are reading the first issue of the journal of *eXPRESS Polymer Letters* appearing twelve times a year with 8–10 original articles monthly. The main scope of *eXPRESS Polymer Letters* is to provide a fast publication platform for papers related to the following topics: polymers; polymer composites; blends and alloys; nanomaterials; molecular engineering; tailor-made polymers; biodegradable and biocompatible polymers; smart materials; polymer gels and membranes; polymer processing technologies; rubbers and rubber technologies; interface issues including adhesion; thin layer technologies; material testing and properties; recycling; modeling and simulation. We intend to publish short original work, new research results as well as review articles. We try to keep the peer reviewing process as short as possible. This is, however, only possible by the support of 'willing' reviewers whose activities are highly appreciated. As the editing is fast, the accepted papers will be published without delay. The International Advisory Board, the composition of which will change with the time, is responsible for the high quality of the articles in our journal. The Board members are internationally recognized experts on their research fields.

The journal is electronically published (www.expresspolymlett.com) and indexed accordingly. It is recommended to produce a printed version of *eXPRESS Polymer Letters* at the end of each year and place it in your library. *eXPRESS Polymer Letters* has joined the international CrossRef system so searching an article published in the journal is quick and simple through the DOI number. *eXPRESS Polymer Letters* is, however, not only a scientific journal, it contains information about other journals and periodicals dedicated to similar topics, as well as announcements of planned conferences. We hope that this journal will be a primary source for researchers, teachers and students active in the fields of science and engineering of polymers and composites and related multidisciplinary topics.

eXPRESS Polymer Letters is expected to become popular accompanied with a high impact factor soon and hopefully we, its editors, may welcome you as readers, authors or reviewers in the future. Your opinions, suggestions are greatly appreciated in advance!

Sincerely yours,

Prof. Dr.-Ing. Dr.hc. J. Karger-Kocsis
Editor-in-chief

Prof. Dr. T. Czigány
Editor

---

*Corresponding author, e-mail: czigany@eik.bme.hu

eXPRESS Polymer Letters Vol.1, No.1 (2007) 2–7
Available online at www.expresspolymlett.com
DOI: 10.3144/expresspolymlett.2007.2

Interfacial effects in nano-silica/polypropylene composites fabricated by in-situ chemical blowing

L. F. Cai[1,2,3], *Y. L. Mai*[3], *M. Z. Rong*[2], *W. H. Ruan*[2], *M. Q. Zhang*[2*]

[1]Key Laboratory for Polymeric Composite and Functional Materials of Ministry of Education, OFCM Institute, School of Chemistry and Chemical Engineering, Zhongshan University, Guangzhou 510275, P. R. China
[2]Materials Science Institute, Zhongshan University, Guangzhou 510275, P. R. China
[3]Guangdong Public Laboratory of Chemical Engineering, Guangzhou 510665, P. R. China

Received 23 October 2006; accepted in revised form 15 November 2006

Abstract. By mixing macromolecular blowing agent grafted nano-SiO_2 with polypropylene (PP) melt, the nanoparticle agglomerates can be pulled apart due to the in-situ bubble-stretching resulting from gasification of the side foaming groups on the grafted polymer. The present work evaluated the interfacial effect in the PP based nanocomposites prepared using the aforesaid technique through introducing rubbery components to the backbone of the grafted polymer chains. The results indicated that deagglomeration of the nanoparticles was not bound to yield the highest properties of the composites. The positive effect of the nanoparticles was brought into full play because of the joint contributions of particles dispersion status and interfacial interaction. An interlayer with proper flexibility ensured an overall enhancement of mechanical properties, especially impact strength, of the nanocomposites.

Keywords: *nanomaterials, processing technologies, nanoparticles, nanocomposites, interfacial effect*

1. Introduction

Polymer/inorganic nanocomposites prepared via melt compounding have become a popular topic in material science because of their markedly improved properties and relatively facile preparation procedures [1, 2]. Enhanced characteristics in such composites have so far been reported as a synergistic contribution resulting from the effective combination of nanoparticles and polymer matrix. However, whether nanoparticles are able to bring positive effects into play depends on their dispersibility in the matrix. Because of the high surface energy, these particles have a great inclination for agglomeration, especially in polymer melts that are characterized by high viscosity. Therefore, preparation of nanocomposites with uniformly distributed nanoparticles is a challenging task [3].

Recently, a novel approach for preparing nanoparticles/polymer composites was developed in the authors' lab based on in-situ bubble-stretching model [4]. That is, macromolecular blowing agent, poly(p-vinylphenylsulfonylhydrazide), was firstly grafted onto nano-silica [5]. The foamable side groups were then gasified during melt compounding with polypropylene (PP). The rapid inflation of the surrounding matrix is able to effectively pull apart the agglomerated nanoparticles, while the remaining backbone of the grafted polymer helped to strengthen the filler/matrix interaction through chain entanglement and interdiffusion at the interface. As a result, mechanical properties of the PP composites were significantly improved. Owing to the trace dosage of the attached foaming groups, the amount of the purposely produced polymer bubbles were kept at rather low level, so that

---

[*]Corresponding author, e-mail: ceszmq@mail.sysu.edu.cn

defoaming of the compounds was not necessary prior to injection molding. It implies that this technique could lead to deagglomeration of the nanoparticles when nanocomposites are being manufactured, without side effect that might deteriorate performance.

For polymer-based nanocomposites, an appropriate surface treatment of inorganic nanoparticles should not only improve dispersion of the fillers, but also bring about notable influence on the interfacial characteristics, and subsequently enhance the mechanical properties of the ultimate composites [6]. Considering that graft treatment of nanoparticles leads to specific interfacial structures that can be tailored by changing graft monomers and graft conditions [7], the authors of the present work planned to introduce polymer chain units with relatively higher molecular mobility (i.e., poly(butyl acrylate)) into the aforesaid grafted polymeric foaming agent poly(p-vinylphenylsulfonylhydrazide) through copolymerization. It is hoped that the stiffness of the interlayer in the nanocomposites originally constructed by the grafted poly(p-vinylphenylsulfonylhydrazide) containing rigid phenyl groups can be somewhat balanced.

In accordance with this idea, poly(p-vinylphenylsulfonylhydrazide-co-butyl acrylate) grafted nanosilica was synthesized. Afterwards, the treated nanoparticles were melt compounded with PP. With the help of in-situ bubble-stretching effect and the flexible interphase, agglomerated silica nanoparticles should be disconnected from each other and adhered to the matrix polymer via the grafted copolymer chains (Figure 1). In this paper, the feasibility of this technical route was analyzed by characterizing the grafted nano-silica and their influence on the structure and properties of PP based composites.

2. Experimental

2.1. Materials

Silica (Aerosil 200) was supplied by Degussa Co., Germany with an average diameter of 12 nm and a specific surface area of 200 m^2/g. The particles were dried at 120°C under vacuum for 24 h to eliminate the physically absorbed and weakly chemically absorbed species. Isotactic PP homopolymer (trade name: HZ730L) with melt flow index (MI) of 5.52 g/10 min (ASTM D569-90), provided by Samsung ATOFINA Co. Ltd., Korea, was used as the matrix polymer of the nano-silica filled composites in this work.

Silane coupling agent (γ-methacryloxypropyl trimethoxy silane, trade name: KH570) was provided by Liao Ning Gaizhou Chemical Industry Co. Ltd., China. 4-styrenesulfonic acid sodium salt hydrate was obtained from Aldrich Chemical Company, Inc., USA. Butyl acrylate (BA) monomer was distilled under low pressure prior to the graft polymerization. N, N-dimethylformamide (DMF) was purified to obtain anhydrous solvent. 2, 2'-azobisisobutyronitrile (AIBN) was recrystallized from ethanol before use.

2.2. Synthesis of grafted nano-SiO$_2$

The procedure of grafting of poly(p-vinylphenylsulfonylhydrazide-co-butyl acrylate) onto nanosilica was similar to that of grafting poly(p-vinyl-

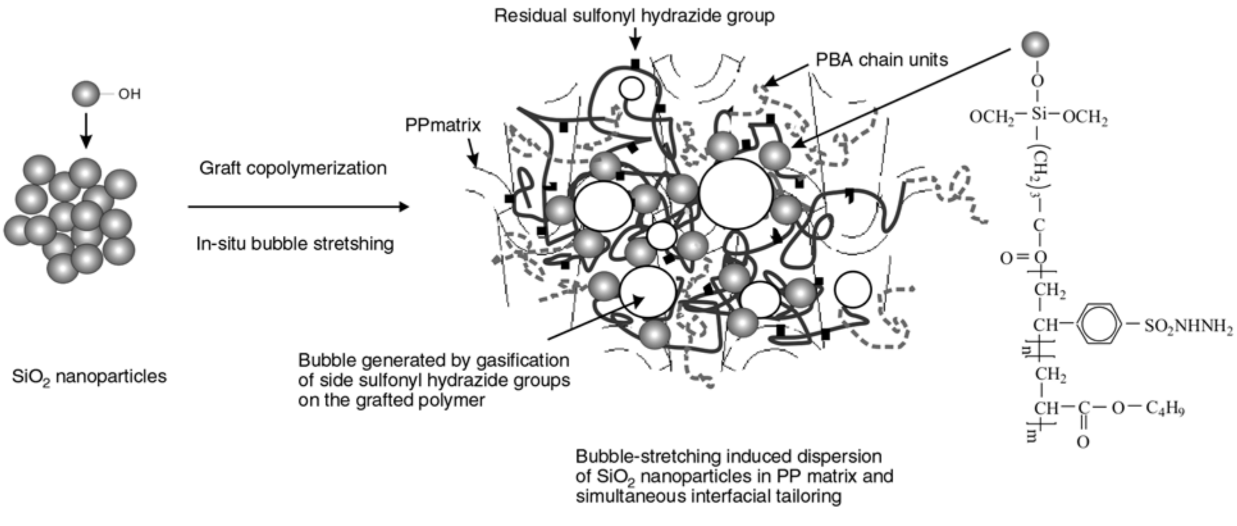

Figure 1. Schematic drawing of the proposed route for making nano-SiO$_2$/PP composites

phenylsulfonylhydrazide) onto nano-silica, which has been described elsewhere [5], despite the fact that butyl acrylate was charged in one batch after p-vinylphenylsulfonylhydrazide had been polymerized for a period of time. A NETZSCH TG 209C thermogravimetric analyzer was used to determine percentage grafting of the grafted nano-silica, and a JXA-8800R electron probe micro-analyzer was employed to investigate the composition the grafted copolymer. Accordingly, poly(p-vinylphenylsulfonylhydrazide-co-butyl acrylate) grafted nano-silica (with a percent grafting of 13.58%, and poly(p-vinylphenylsulfonylhydrazide/poly(butyl acrylate) = 1.00/2.63 (weight ratio)) was used for the subsequent characterization and composites preparation.

2.3. Composites preparation

To prepare PP composites, ungrafted or grafted nano-silica was compounded with PP in the mixer of a Haake Rheocord 300p torque rheometer at 180°C for 10 min. Rotation speed of the mixing rotors was set at 60 rpm. Then, the mixture was injection molded into nanocomposites standard bars for mechanical tests with a Y-350 vertical injection molding machine. The dimensions of deformable region of tensile dumbbell specimens are 25.0×3.2×2.0 mm^3, while those of the rectangular bars for testing impact strength are 80×10×4 mm^3. The bars were further notched in the middle using a CSI cutter to produce 'V' type notches with a depth of 2 mm.

2.4. Characterization

Fourier-transform infrared (FTIR) spectroscopy was employed to investigate the variation in surface chemical structure of the nanoparticles. The spectra were recorded in KBr pellets on a Nicolet 5DX FTIR spectrometer. Blank scanning was performed before measurements to eliminate the influence of water vapor and CO_2 in air.

Thermal degradation measurements were performed on the aforesaid thermogravimetric analyzer from 30 to 800°C at a heating rate of 10°C/min under the flow of anhydrous air.

To assess dispersion of the nanoparticles in PP matrix, ultrathin sections of the compounds obtained from the melt mixing were examined by a FEI TECNAI 12 transmission electron microscope (TEM) at an accelerating voltage of 100 kV.

Tensile properties of the nanocomposites were determined with a Hounsfield 10K-S universal tester at a crosshead speed of 50 mm/min according to ASTM D638-98. Notched Charpy impact strength was measured by an Atlas advanced pendulum impact device in accordance with ISO 179–2. All of the specimens were stored at 30°C and 50% relative humidity for 48 h in advance.

3. Results and discussion

Prior to study of the nanocomposites, surface feature of the grafted nano-silica should be known. It is shown in Figure 2 that in comparison with the spectrum of nano-silica as-received, the additional characteristic adsorptions of carbonyl groups (~1730 cm^{-1}), phenyl (~576 cm^{-1} and 1458 cm^{-1}, respectively) and C–H stretching modes (multiple peaks at 2820~2962 cm^{-1}) appear on the spectrum of grafted nano-silica. Evidently, poly(p-vinylphenylsulfonylhydrazide-co-butyl acrylate) has been covalently bonded to the nanoparticles as expected.

Since the modified nanoparticles are intended to bring the macromolecular foaming agent into PP, pyrolytic behaviors of the related substances were measured (Figure 3). The visible differences among the grafted nano-silica, untreated nano-silica and silane treated silica should be indicative of the role of the grafted polymer. There is an obvious weight loss at around 138°C on the thermogram of the grafted nanoparticles, which is similar to the

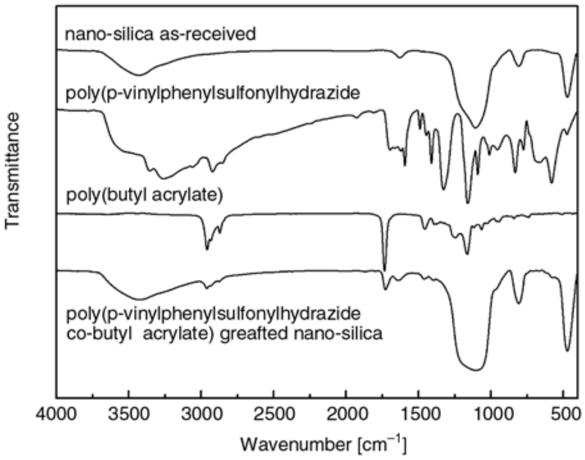

Figure 2. FTIR spectra of the related materials. For the grafted nano-silica, the ungrafted polymer had been removed by solvent extraction before the FTIR measurement

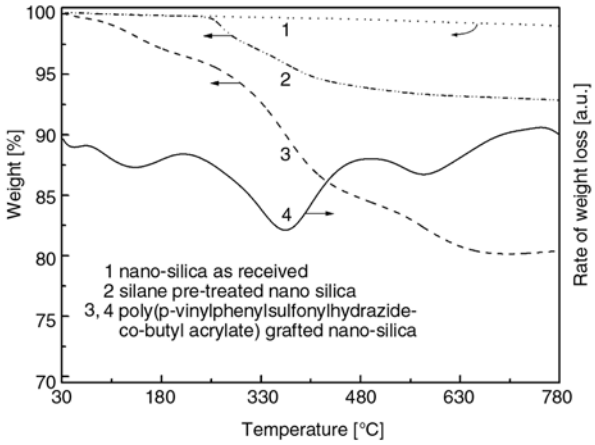

Figure 3. TGA thermograms of the related materials. For the grafted nano-silica, the ungrafted polymer had been removed by solvent extraction before the TGA measurement

result of poly(p-vinylphenylsulfonylhydrazide) grafted ones and ranks between the gasification temperatures of p-vinylphenylsulfonylhydrazide (120°C) and poly(p-vinylphenylsulfonylhydrazide) (169°C) as reported in our previous work [5]. It must originate from gasification of the sulfonyl hydrazide groups. Clearly, copolymerization of p-vinylphenylsulfonylhydrazide with butyl acrylate does not change blowing ability of the former. As a result, poly(p-vinylphenylsulfonylhydrazide-co-butyl acrylate) grafted silica nanoparticles should be able to arouse in-situ bubble-stretching when the particles are blended with PP melt.

To demonstrate the effect of the grafted nanoparticles, TEM photos of the PP composites were compared. As shown in Figure 4, the grafted nanoparticles seems to be much smaller than the untreated ones in the polymer matrix. Distribution of the treated nano-silica is rather homogeneous (Figure 4b). Evidently, the local rapid expansion of the matrix polymer nearby the nanoparticles caused by gasification of the sulfonyl hydrazide groups on the grafted polymer must have taken effect. It forces SiO_2 nanoparticle agglomerates to be deagglomerated in the course of melt compounding.

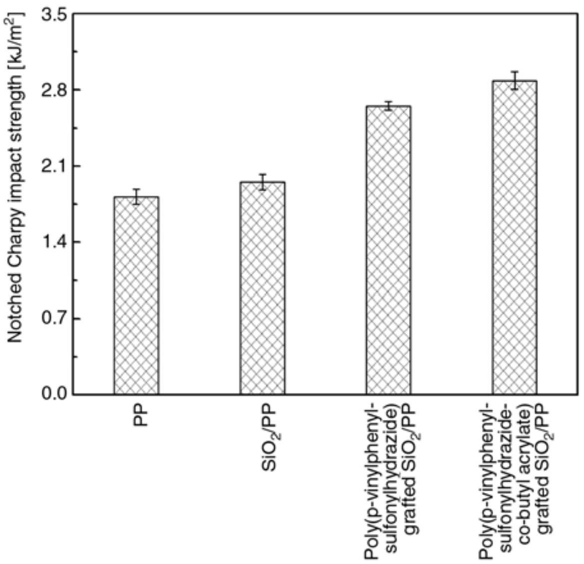

Figure 5. Notched Charpy impact strength of PP and its composites. Content of nano-silica in all the composites: 1.43vol%

With respect to mechanical properties of the nanocomposites, Figure 5 shows the results of notched Charpy impact strength. It is seen that the contribution of the untreated fillers to the improvement of toughness under high speed deformation and to the reduction of notch sensitivity is nearly negligible as compared with the grafted ones. This should be attributed to the worse dispersion of the untreated nanoparticles in PP matrix. Besides, the loose clusters of the nanoparticles might act as weak sites of the composites. For poly(p-vinylphenylsulfonylhydrazide-co-butyl acrylate) grafted SiO_2/PP composite, its notched impact strength is higher than

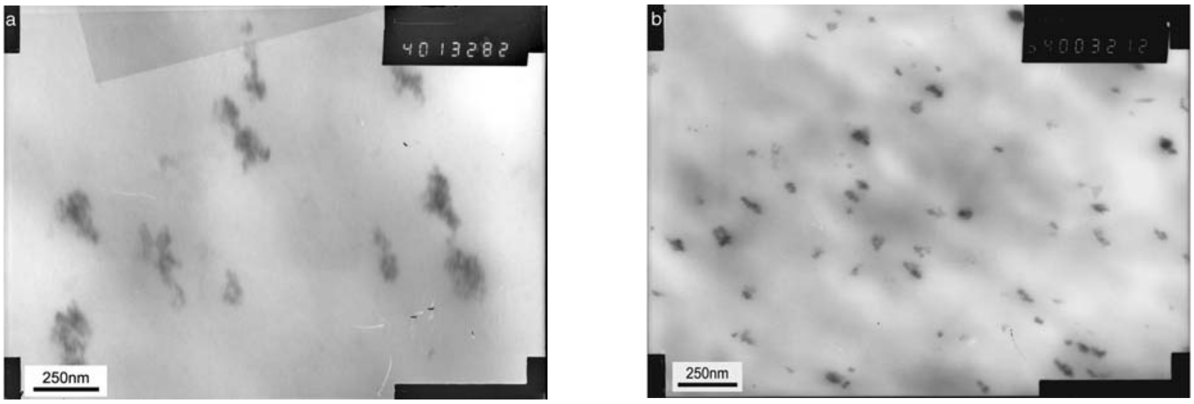

Figure 4. TEM images of ultrathin sections of (a) untreated nano-SiO_2/PP, (b) poly(p-vinylphenylsulfonylhydrazide-co-butyl acrylate) grafted nano-SiO_2/PP composites

that of poly(p-vinylphenylsulfonylhydrazide) grafted SiO_2/PP system. According to Rong et al. [7], the grafted polymer, especially the one with higher molecular mobility, might play the role of a bumper interlayer around the fillers, while absorbing impact energy and preventing initiation of cracks. The data in Figure 5 coincide with the above conclusion. It means that even dispersion of the nanoparticles driven by in-situ bubble stretching does not guarantee the optimal toughening effect. An increase in flexibility of the grafted polymer chains facilitates a further improvement of nanocomposites' ductility.

Tensile properties of PP composites are illustrated in Figure 6. In comparison with neat PP, all the composites exhibit higher tensile strength. A careful survey indicates that the increase in strength of untreated nano-silica/PP composite is marginal while that of grafted nano-silica/PP composites are more prominent. The chain entanglement/ interdiffusion at the interface between the grafted polymer and PP matrix should account for the strengthening effect, due to the enhanced stress transfer efficiency [8]. This is different from the situation of microparticulates/polymer composites, which is characterized by a drastic decrease in tensile strength with the incorporation of the fillers [9].

It is interesting to see that tensile strengths of poly(p-vinylphenylsulfonylhydrazide) grafted nano-silica/PP and poly(p-vinylphenylsulfonylhydrazide-co-butyl acrylate) grafted nano-silica/PP composites are almost the same regardless of species of the grafted polymer. Obviously, the difference in rigidity of the interphase in the two nanocomposites is not extremely great, which ensures similar stress transfer behavior under static tensile condition. The analysis receives support from Young's modulus of the composites, as both grafted nano-silica/PP composites possess nearly the same stiffness (Figure 6). It suggests that the mechanical responses of the composites containing two types of grafted polymer resemble each other within Hooke's limit. On the other hand, because Young's modulus of particulate composites is highly related to the filler-matrix interfacial interaction [10], appearance of grafted polymer on the nanoparticles has to shield the matrix from the particles and leads to insufficient impartation of the fillers' rigidity to PP. Therefore, the untreated SiO_2/PP composite has the highest Young's modulus.

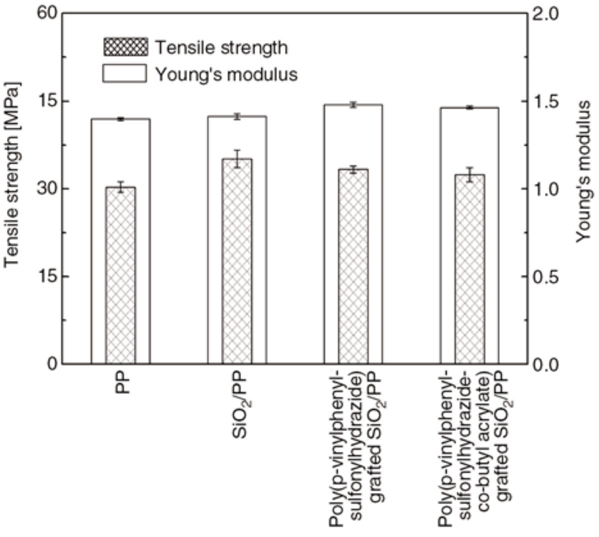

Figure 6. Tensile strength and Young's modulus of PP and its composites. Content of nano-silica in all the composites: 1.43vol%

4. Conclusions

The above investigation reveals the importance of both deagglomeration of nanoparticles and interfacial design in making polymer nanocomposites with improved properties. Taking the advantage of graft polymerization, the specific structural requirements can be satisfied in one step. The key issue lies in the introduction of polymeric foaming agent containing soft segments (i.e. poly(p-vinylphenylsulfonylhydrazide-co-butyl acrylate)) onto the surface of nano-SiO_2. In the case of melt blending with PP, the side sulfonyl hydrazide groups on the grafted copolymer are able to be gasified like foaming agent to induce localized bubble-stretching effect that pulls apart nanoparticles agglomerates. Meanwhile, the skeleton of the grafted copolymer would get entangled with the matrix polymer forming strong interfacial interaction, and the poly(butyl acrylate) units in the grafted copolymer help to raise ductility of the interlayer. Compared to the composite containing rigid macromolecular foaming agent grafted nano-SiO_2 (i.e., poly(p-vinylphenylsulfonylhydrazide) grafted nano-SiO_2/PP), the composite fabricated in this work (i.e., poly(p-vinylphenylsulfonylhydrazide-co-butyl acrylate) grafted nano-SiO_2/PP) shows much greater increment in notched impact strength without expense of lowing tensile performance. In consideration of structure adjustability of copolymers attached to nanoparticles, the present work has opened up a simple way to manufacture polymer nanocomposites with tailorable properties.

Acknowledgements

The authors are grateful for the support of the National Natural Science Foundation of China (Grant: 50473019), the Natural Science Foundation of Guangdong, China (Grants: 2004A10702001, 2005A10702001 and 5003267), the Science and Technology Department of Guangzhou, China (Grant: 2004Z3-D2061), and the Guangdong Economic & Trade Commission, China (Grant: 20040112).

References

[1] Zhang M. Q., Rong M. Z., Friedrich K.: Processing and properties of nonlayered nanoparticle reinforced thermoplastic composites. in: 'Handbook of organic-inorganic hybrid materials and nanocomposites' (ed.: Nalwa H. S.) American Science Publishers, Los Angeles, Vol 2, 113–150 (2003).

[2] Leuteritz A., Pospiech D., Kretzschmar B., Willeke M., Jehnichen D., Jentzsch U., Grundke K., Janke A.: Progress in polypropylene nanocomposites development. Advanced Engineering Materials, **5**, 678–681 (2003).

[3] Rong M. Z., Zhang M. Q., Ruan W. H.: Surface modification of nanoscale fillers for improving properties of polymer nanocomposites: a review. Materials Science and Technology, **22**, 787–796 (2006).

[4] Meng Q. Y., Wu D. M.: A study of bubble inflation in polymers and its applications. Physics Letters A., **327**, 61–66 (2004).

[5] Cai L. F., Huang X. B., Rong M. Z., Ruan W. H., Zhang M. Q.: Effect of grafted polymeric foaming agent on the structure and properties of nano-silica/polypropylene composites. Polymer, **47**, 7043–7050 (2006).

[6] Keszei S., Matko S., Bertalan G., Anna P., Marosi G., Toth A.: Progress in interface modifications: from compatibilization to adaptive and smart interphases. European Polymer Journal, **41**, 697–705 (2005).

[7] Rong M. Z., Zhang M. Q., Pan S. L., Friedrich K.: Interfacial effects in polypropylene-silica nanocomposites. Journal of Applied Polymer Science, **92**, 1771–1781 (2004).

[8] Wu C. L., Zhang M. Q., Rong M. Z., Friedrich K.: Tensile performance improvement of low nanoparticles filled-polypropylene composites. Composites Science and Technology, **62**, 1327–1340 (2002).

[9] Nicolais L., Narkis M.: Stress-strain behavior of styrene-acrylonitrile/glass bead composites in the glassy region. Polymer Engineering and Science, **11**, 194–199 (1971).

[10] Walter R., Friedrich K., Privalko V., Savadori A.: On modulus and fracture toughness of rigid particulate filled high density polyethylene. Journal of Adhesion, **64**, 87–109 (1997).

eXPRESS Polymer Letters Vol.1, No.1 (2007) 8–14
Available online at www.expresspolymlett.com
DOI: 10.3144/expresspolymlett.2007.3

Effect of blend ratio on aging, oil and ozone resistance of silica-filled chloroprene rubber/natural rubber (CR/NR) blends

P. Sae-oui[1,2*], *C. Sirisinha*[2,3], *K. Hatthapanit*[1]

[1]National Metal and Materials Technology Center, 114 Thailand Science Park, Paholyothin Rd., Klong 1, Klong-Luang, Pathumthani 12120, Thailand
[2]Rubber Research Unit, Faculty of Science, Mahidol University, Salaya Campus, Phutthamonthon 4 Rd., Salaya, Nakornprathom 73170, Thailand
[3]Department of Chemistry, Faculty of Science, Mahidol University, Rama 6 Rd., Rajdhevee, Bangkok, 10400, Thailand

Received 18 October 2006; accepted in revised form 2 December 2006

Abstract. The effect of blend ratio on properties of chloroprene rubber/natural rubber (CR/NR) blends was investigated. In addition to the mechanical properties, attention was also given to the resistance to thermal aging, oil and ozone of the blends. Silica was selected as a reinforcing filler in this study due to its unique characteristic to interact with CR. The results reveal that, due to the better filler dispersion and the greater crosslink density, the silica-filled CR possesses lower compound viscosity and better mechanical properties, compared to the silica-filled NR. The aging properties, oil and ozone resistance of the silica-filled CR are also significantly better than those of the silica-filled NR. The mechanical properties and the resistance to degradation of the silica-filled CR/NR blends are mainly governed by the blend morphology. It is found that good mechanical properties in association with adequately high resistance to degradation from thermal aging and oil are obtained when CR remains the matrix in the blends. Even though the ozone cracks are found in all blends, a thorough look at the results reveals that considerable improvement in ozone resistance is achieved with increasing CR content.

***Keywords:** rubber, blend, oil resistance, aging resistance, mechanical properties*

1. Introduction

Rubber blends have gained much attention in the rubber industry because, when properly formulated, the blend could combine the best features of the individual blend partner. Desirable outcome is therefore easily obtained. Natural rubber (NR) is widely known to possess good mechanical properties such as high tensile and tear strengths due to its ability to crystallize upon stretching. The elasticity and dynamic properties of NR are also excellent. However, due to the existence of numerous reactive double bonds on the molecular backbone, NR is highly susceptible to degradation by thermal aging and ozone attack. In addition, oil resistance of NR is relatively poor, compared to some polar synthetic rubbers such as chloroprene rubber (CR) or acrylonitrile butadiene rubber (NBR). To overcome such shortcomings, NR is frequently blended with synthetic rubbers such as NBR or CR. Recently, blends of NR/CR have been extensively studied [1–4]. The incorporation of CR into NR helps to improve oil and thermal resistance of NR. As CR and NR are cured in different manners, careful adjustment of the cure system must be taken into account to avoid maldistribution of crosslinks within the two phases. Cure system of NR/CR blend therefore generally includes sulfur, thiourea derivatives with the addition of other conventional

---

[*]Corresponding author, e-mail: pongdhor@mtec.or.th

accelerators [5]. Apart from the curing system, the difference in polarity of the blend partners could also bring about high interfacial tension which is detrimental to the mechanical properties of the blend [6]. The addition of suitable compatibilizer is therefore recommended.

It has currently been reported that precipitated silica, widely used as reinforcing filler for most rubbers, could form strong interaction with CR through hydrogen bonds [7–8]. The presence of silica in CR could also give rise to additional crosslinks due to the chemical reaction between the silanol groups on silica surface and the allylic chlorine atoms in CR [9–10]. These reports confirm that silica interacts with CR in a special manner which is different from the most commonly used filler, carbon black. It is therefore interesting to use silica as a reinforcing filler for this CR/NR blend. In the present study, the effect of blend ratio on properties of silica-filled CR/NR blend was investigated. The mechanical properties as well as the resistance to aging, oil and ozone of the blends were focused.

2. Experimental

2.1. Materials

All mixing ingredients were used as received. Polychloroprene (CR, Neoprene W) with the Mooney viscosity of 44-ML1+4 @ 100°C was supplied by DuPont Dow Elastomers PTE Ltd. Natural rubber (NR, STR 5L) with the Mooney viscosity of 74-ML1+4 @ 100°C was manufactured in Thailand by Union Rubber Products Corp. Ltd. Silica (HiSil 255s with specific surface area of 175 m^2/g) was supplied by Tokuyama Siam Silica Co., Ltd. N-tert-butyl-2-benzothiazole sulfenamide (Santocure-TBBS) was obtained from Reliance Technochem (Flexsys) Co., Ltd. Stearic acid, zinc oxide (ZnO, white seal) and sulfur (S_8) were obtained from Kij Paiboon Chemical Ltd. (Thailand). Ethylene thiourea (ETU 22S) and magnesium oxide (MgO) were manufactured in Japan by Kawakushi Co., Ltd. and Konoshima Chemical Co., Ltd., respectively.

2.2. Preparation and testing of rubber compounds

The compound formulation used in the present study is given in Table 1. The mixing process was carried out using a laboratory-sized internal mixer (Haake Rheomix 3000p). The mixing conditions were set as follows; fill factor = 0.7, initial chamber temperature = 60°C, rotor speed = 40 rpm and mixing time = 12 minutes. After mixing, the compounds were sheeted out on a two-roll mill (Collin W100T). Measurement of Mooney viscosity (MS1+4 @ 100°C) was carried out using the Mooney viscometer (TechPro viscTECH+). The cure characteristics, e.g., scorch time (t_s2) and optimum cure time (t_c90) including minimum torque (ML) and maximum torque (MH) were determined using a moving die rheometer (MDR, TechPro MD+) at 155°C. As it is reported earlier that the torque difference (MH–ML) is directly proportional to the degree of crosslinking, it is therefore employed to indirectly represent the crosslink density of the blend vulcanizates herein [11].

Table 1. The compound formulation

Ingredient	Loading (parts per hundred of rubber, phr)				
Polychloroprene (CR)	100	75	50	25	0
Natural rubber (NR)	0	25	50	75	100
Zinc Oxide	5	5	5	5	5
Stearic acid	1	1	1	1	1
Magnesium Oxide	4	4	4	4	4
Silica	30	30	30	30	30
TBBS*	1	1	1	1	1
Ethylene thiourea	0.3	0.3	0.3	0.3	0.3
Sulfur	2	2	2	2	2

*N-tert-butyl-2-benzothiazole sulfenamide

2.3. Testing of rubber vulcanizates

Vulcanization of the compounds was carried out using compression molding technique at 155°C based on the optimum cure time obtained from MDR. The tensile properties were determined using a universal testing machine (Instron 4301 series) following ISO 37. The hardness was measured using a Wallace Shore A durometer according to ISO 868. Ozone resistance test was carried out according to ISO 1431/1. The rectangular specimens were stretched to 20% strain and conditioned at 40°C for 48 hours prior to testing. The conditioned specimens were then put into an ozone QUV resistance tester (Toyoseiki) at 40°C and 50 parts per hundred million (pphm) ozone concentration for 70 hours. The ozone cracks were thereafter determined. The thermal aging properties of the rubber vulcanizates were studied by placing the specimens in an aging oven at 100°C for 72 hours prior to the determination of tensile properties. Oil resistance was measured, according to ISO 1817, by immersing the specimens in non-polar hydraulic oil (Shell-Tellus 100) for 7 days at room temperature (23°C). After the immersion, the specimens were blotted off with filtered paper and rinsed with acetone prior to the determinations of mass change and tensile properties. In this study, the degree of filler dispersion and blend morphology were examined using a scanning electron microscope (SEM, JEOL JSM-5410) and an atomic force microscope (AFM, Multimode Nanoscope IIIA), respectively. The SEM micrographs were taken on the newly exposed surface of the rubber specimens fractured immediately after embrittling in liquid nitrogen. The specimens were then sputtered with gold to prevent charging on the surface. The AFM micrographs were taken on the newly exposed surface cut from the microtome under sub-ambient condition.

3. Result and discussion

The dependence of Mooney viscosity on blend ratio is illustrated in Figure 1. As can be seen, the viscosity of the CR/NR blend increases continuously with increasing NR content in the blends. This is attributed to the dilution effect because the results reveal that neat CR possesses the lowest viscosity whereas neat NR possesses the highest viscosity, i.e., the low viscosity CR portion is substituted by the high viscosity NR portion. Apart from the higher molecular weight of NR, the poor filler dispersion also contributes to the high viscosity of silica-filled NR. As silica is a highly polar filler whereas NR is considered as a non-polar elastomer, the rubber-filler interaction is therefore relatively low. On the contrary, the hydroxyl or silanol groups on silica surface could form hydrogen bonds towards each other resulting in a strong filler-filler interaction. Disagglomeration of silica is therefore more difficult to take place leading to poor filler dispersion. However, in neat CR, the rubber-filler interaction is relatively high because CR contains chlorine atoms which could interact strongly with the silanol groups on silica surface. The degree of filler dispersion in neat CR is there-

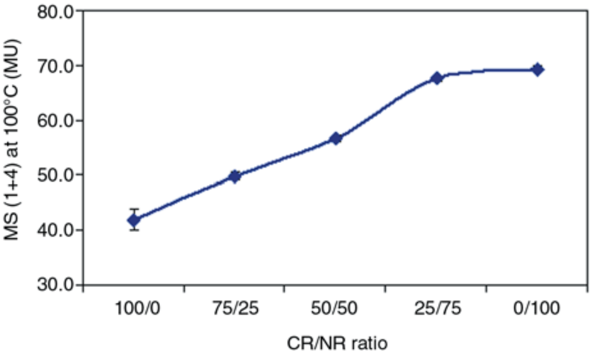

Figure 1. Effect of blend ratio on Mooney viscosity of the compounds

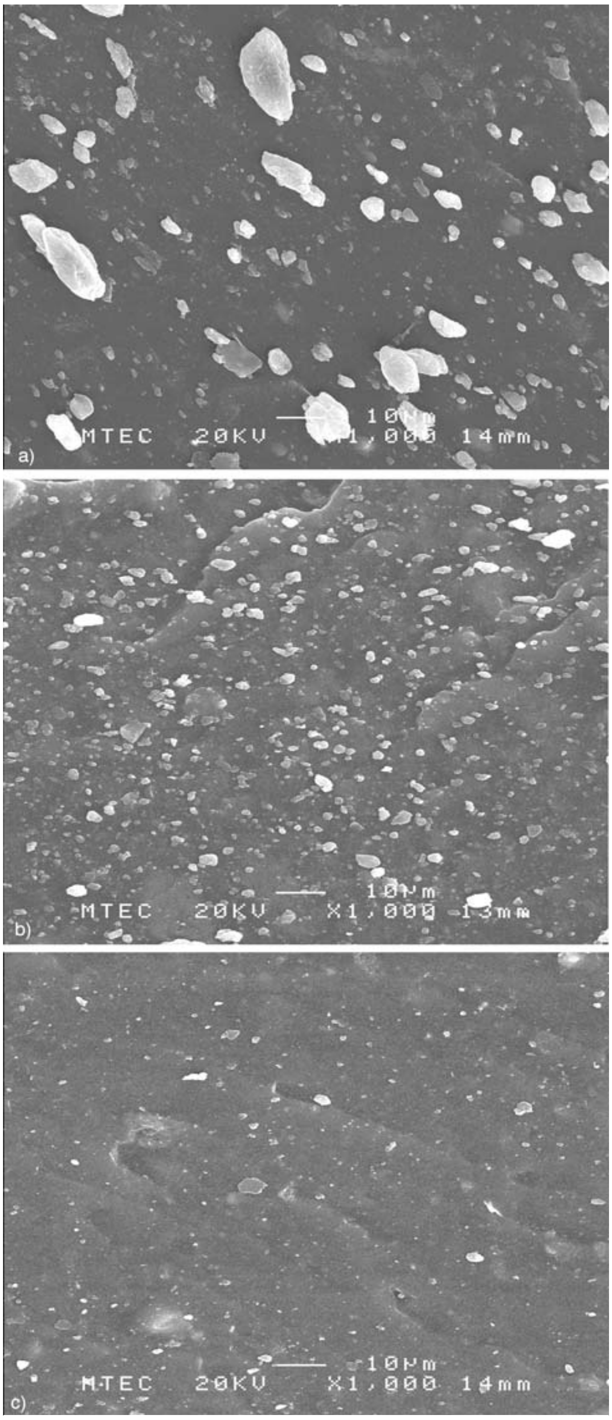

Figure 2. SEM micrographs of (a) silica-filled NR, (b) silica-filled 50/50 CR/NR blend and (c) silica-filled CR

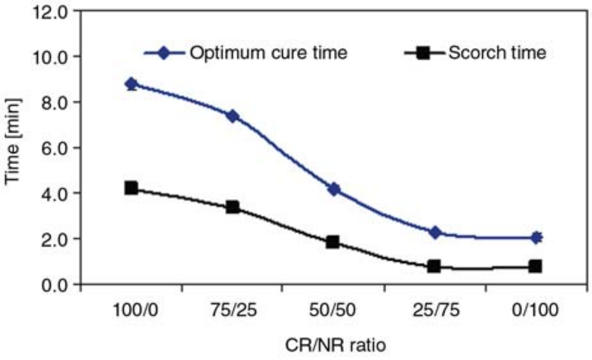

Figure 3. Effect of blend ratio on scorch time (t_s2) and optimum cure time (t_c90) of the compounds

fore higher than that in neat NR as shown in Figure 2.

Cure characteristics of the compounds were also investigated and the results are given in Figure 3. It is widely known that the double bonds in NR are more reactive to vulcanization reaction than those in CR and the non-rubber content in NR could also accelerate cure, neat NR therefore possesses significantly shorter scorch time and optimum cure time, compared to neat CR. Similar observation is also found in the work of Ismail, et al. [12] in which the longer Mooney scorch time of CR is explained by the curing nature of CR to prevent scorch [13]. Due to the dilution effect, both scorch time and optimum cure time are found to reduce consecutively with increasing NR content in the blend. Although cure rate is increased with increasing NR content, it is surprising that the state of cure or crosslink density, as measured from the torque difference (MH–ML), follows the opposite trend, i.e., the crosslink density tends to reduce with increasing NR content in the blends as shown in Figure 4. The highest state of cure found in neat CR is thought to arise from the combination of crosslink obtained from conventional vulcanization and additional crosslink from the chemical reaction between the silanol group on silica surface and the allylic chlorine atoms of CR [9]. On the other hand, the unexpectedly low state of cure found in neat NR is thought to take place from the retarding effect of silica. Due to the presence of sianol groups on silica surface, silica could adsorb zinc complex and amine accelerator giving rise to cure retardation and, thus, the reduction of crosslink density [14]. Again, due to the dilution effect, the state of cure of CR/NR blend is found to decrease with increasing NR content.

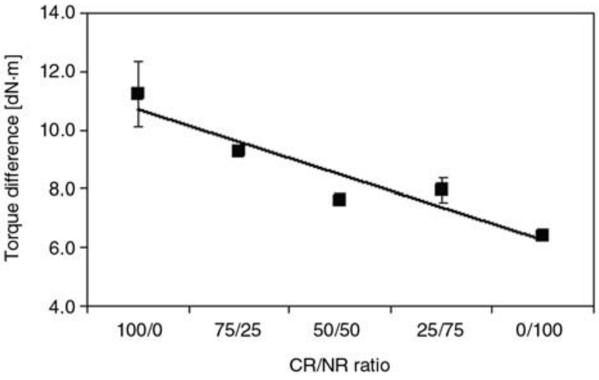

Figure 4. Dependence of torque difference on blend ratio

Table 2 represents the effect of blend ratio on tensile properties and hardness of the rubber vulcanizates. In this study, the tensile strength of neat NR is unexpectedly low because silica is added into the rubber without the addition of glycol, amine or silane coupling agent. The absence of such compound in neat NR leads to poor filler dispersion, poor rubber-filler interaction and low crosslink density. The tensile strength of neat NR is therefore relatively low, compared to neat CR. In addition, both 100% modulus and hardness of neat NR are lower than those of neat CR. Possible explanation is given to the lower state of cure of neat NR as mentioned earlier. As expected, these properties of the rubber blends tend to decrease with increasing NR content. This is attributed to the dilution effect. A thorough look at the tensile strength results also reveal that the reduction of tensile strength with increasing NR content does not follow the mixture rule, i.e., the tensile strength is reduced slightly with increasing NR content up to 50/50 CR/NR ratio. Further increase in NR content results in a sharp drop of tensile strength. The blend morphology could be used to explain the results. The AFM micrographs of the blends at various blend ratios are given in Figure 5. The results clearly reveal that, for both 75/25 and 50/50 CR/NR blends, CR is the continuous phase (represented by the dark area) and NR is the dispersed phase (represented by the light area). Most properties of these blends there-

Table 2. Effect of blend ratio on tensile properties and hardness of the vulcanizates

CR/NR Blend ratio	Tensile strength [MPa]	100% Modulus [MPa]	Hardness [Shore A]
100/0	25.8±0.5	1.54±0.05	59.9±0.4
75/25	23.8±0.9	1.35±0.03	57.1±0.6
50/50	24.0±1.0	1.14±0.06	53.2±0.4
25/75	18.2±1.0	1.07±0.04	51.7±0.6
0/100	12.4±1.1	0.92±0.02	50.3±1.2

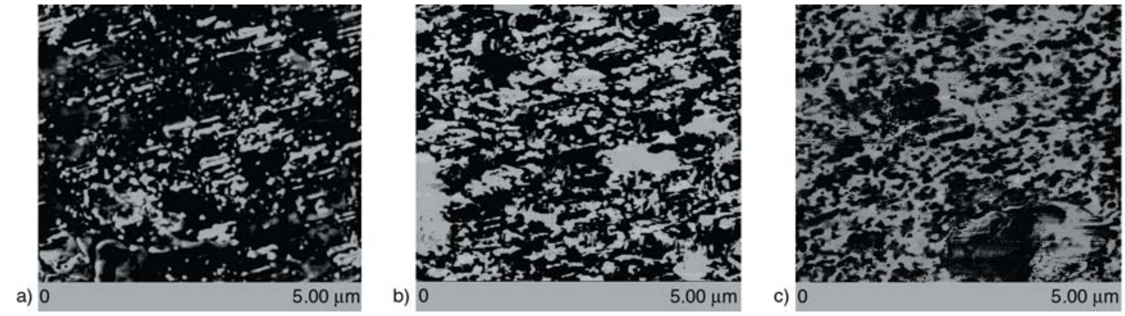

Figure 5. AFM micrographs of (a) 75/25 CR/NR blend, (b) 50/50 CR/NR blend and (c) 25/75 CR/NR blend

fore resemble those of neat CR. Similar observation has been previously reported for chlorinated polyethylene/natural rubber (CPE/NR) blend by Sirisinha, et al. [15] At 25/75 CR/NR ratio, phase inversion takes place and most properties of the blend are mainly controlled by the NR matrix. It could also be observed that both 100% modulus (M_{100}) and hardness are reduced with increasing NR content in the blends. This is understandable because silica accelerates and increases state of cure in CR whereas, for NR, it shows cure retarding effect resulting in the reduction of crosslink density and, thus, modulus and hardness. Increasing NR content in the blend therefore gives rise to a softer silica-filled vulcanizate.

The effect of blend ratio on aging resistance which is represented in terms of the relative value (the ratio of the properties after aging to those before aging) is illustrated in Figure 6. The results reveal that, regardless of blend ratio, aging at high temperature leads to the reduction of tensile strength (the relative tensile strength is less than 1). As the double bonds in CR are less reactive to thermal oxidative degradation, CR is more resistant to thermal aging than NR as can be seen from the higher relative tensile strength. Again, due to the dilution effect, the aging resistance of the blends is found to reduce with increasing NR content. At 25/75 CR/NR ratio where NR becomes the matrix, the aging resistance of the blend is similar to that of neat NR.

For the relative 100% modulus, different results are observed. After aging, the modulus of neat CR is increased due to the post curing effect whereas the modulus of neat NR is decreased due to the predominant chain scission induced by the thermal oxidative reaction. For rubber blends, the relative 100% modulus tends to decrease with increasing NR content due to the dilution effect. It could be observed that, at 75/25 and 50/50 CR/NR ratios in which CR still remains the matrix, the effect of post curing in CR phase could override the effect of chain scission in NR phase giving rise to the increase in modulus after aging (the relative modulus is greater than 1). However, at 25/75 CR/NR ratio where NR becomes the matrix, the effect of chain scission is more pronounced than the post curing effect giving rise to the overall decrease in modulus after aging. Similar trend is also found for the relative hardness. The same explanation is applied.

The effect of blend ratio on oil resistance, represented in terms of the relative value, is depicted in Figure 7. Generally, CR is classified as a polar rub-

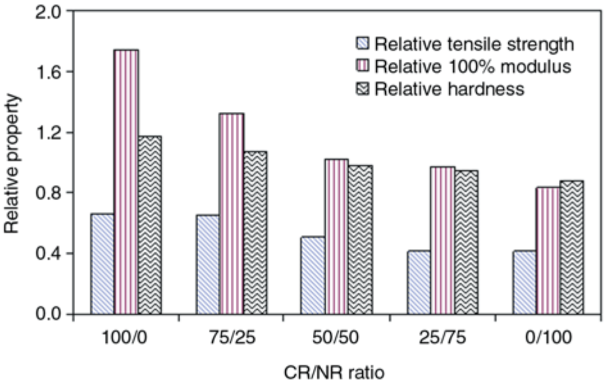

Figure 6. Effect of blend ratio on thermal aging resistance (represented in terms of the relative properties)

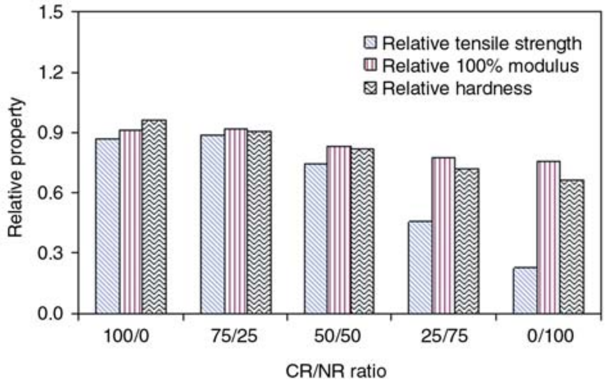

Figure 7. Effect of blend ratio on oil resistance (represented in terms of the relative properties)

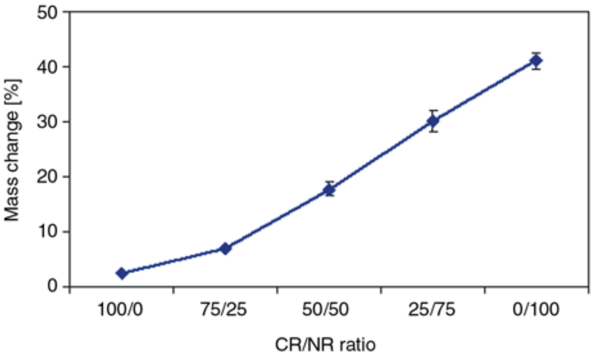

Figure 8. Dependence of oil resistance on blend ratio (represented in terms of the mass change)

ber due to the existence of chlorine (Cl) atoms in its molecule. CR is therefore more resistant to oil compared to the non-polar NR as can be seen from the higher values of relative tensile strength, relative modulus as well as relative hardness. For rubber blends, good resistance to oil is achieved as long as CR still remains the matrix. This is found in 75/25 and 50/50 CR/NR blends. For 25/75 CR/NR blend in which NR becomes the matrix, the oil resistance drops significantly. In addition to the relative properties, the oil resistance of the blends was also measured in terms of mass change after oil immersion and the results are given in Figure 8. As expected, the lowest mass change is found for neat CR and the highest mass change is found for neat NR. The mass change of the blends lies in between those of the individual blend partners. The higher the NR content in the blend, the greater the mass change or the poorer the oil resistance.

Ozone resistance of the rubber vulcanizates was also investigated and, after testing, the ozone cracks at the surface of the specimens were photographed as shown in Figure 9. Obviously, after exposing to 50 pphm of ozone concentration for 70 hours, no visual crack is found on the specimen surface for neat CR. The moderately high ozone resistance of CR arises from the lower reactivity of double bonds to ozone attack. However, for NR in which its double bonds are highly reactive to ozone attack, large and deep ozone cracks are found on the specimen surface. The severe ozone cracks are also found in 25/75 CR/NR blend in which NR is the matrix. Although the cracks are also observed in 75/25 and 50/50 CR/NR blends, it could be observed that the cracks found in these blends are less severe, compared to neat NR. The higher the CR content in the blend, the greater the ozone resistance of the vulcanizate.

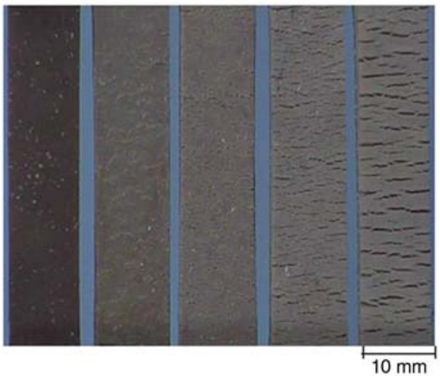

Figure 9. Influence of blend ratio on ozone resistance of CR/NR blends (from left to right: 100/0, 75/25, 50/50, 25/75 and 0/100)

4. Conclusions

Taken as a whole, the results reveal that increasing NR content in the silica-filled CR/NR blend gives rise to the increases of Mooney viscosity and cure rate. However, the state of cure and, thus, modulus and hardness are found to reduce with increasing NR content. The degree of filler dispersion is also reduced with increasing NR content due to the poor interaction between non-polar NR and highly polar silica. The highest state of cure found in silica-filled CR is thought to arise from the additional crosslinks obtained from the chemical reaction between allylic Cl atoms of CR and the silanol groups on silica surface. Resistance to thermal aging, oil and ozone attack of the rubber blend is mainly governed by the blend morphology. It is found that, at 50/50 CR/NR ratio, the silica-filled CR/NR blend possesses good mechanical properties in association with satisfactory aging and oil resistance because this blend still has CR as the matrix. At higher NR content, phase inversion takes place. Considerable reductions of both mechanical properties and resistance to degradation from thermal aging and oil are therefore observed. Although ozone cracks are found in all blends, great improvement in ozone resistance is observed when CR content is increased.

References

[1] Saad A. L. G., El-Sabbagh S.: Compatibility studies on some polymer blend systems by electrical and mechanical techniques. Journal of Applied Polymer Science, **79**, 60–71 (2001).

[2] Helaly F. M., El-Sabbagh S. H.: Bone meal waste and $Ca(HPO_4)_2$ as reinforcing filler for NR and CR and

their blends compared with conventional white filler. Journal of Elastomers and Plastics, **34**, 335–348 (2002).

[3] Das A., Ghosh A. K., Basu D. K.: Evaluation of physical and electrical properties of chloroprene rubber and natural rubber blends. Kautschuk Gummi Kunststoffe, **58**, 230–238 (2005).

[4] Ramesan M. T., Alex R., Khanh N. V.: Studies on the cure and mechanical properties of blends of natural rubber with dichlorocarbene modified styrene-butadiene rubber and chloroprene rubber. Reactive & Functional Polymers, **62**, 41–50 (2005).

[5] Hofmann W.: Rubber technology handbook. Hanser Publishers, Munich (1989).

[6] Tinker A. J., Jones K. P.: Blends of natural rubber: Novel techniques for blending with speciality polymers. Chapman & Hall Ltd., London (1998).

[7] Choi S.: Improvement of properties of silica-filled natural rubber compounds using polychloroprene. Journal of Applied Polymer Science, **83**, 2609–2616 (2002).

[8] Das A., Debnath S. C., De D., Basu D. K.: Evaluation of physical properties and curing characteristics of silica-filled ethylene-propylene-diene terpolymer in the presence of chloroprene rubber. Journal of Applied Polymer Science, **93**, 196–200 (2004).

[9] Wang G., Li M., Chen X.: Effects of filler on mechanical properties of a water-swellable rubber. Journal of Applied Polymer Science, **72**, 577–584 (1999).

[10] Sae-oui P., Sirisinha C., Thepsuwan U., Hatthapanit K.: Dependence of mechanical and aging properties of chloroprene rubber on silica and ethylene thiourea loadings, European Polymer Journal, **43**, 185-193, 2007.

[11] Sae-oui P., Sirisinha C., Thepsuwan U., Hatthapanit K.: Role of silane coupling agents on properties of silica-filled polychloroprene. European Polymer Journal, **42**, 479–486 (2006).

[12] Ismail H., Leong H. C.: Curing characteristics and mechanical properties of natural rubber/chloroprene rubber and epoxidized natural rubber/chloroprene rubber blends. Polymer Testing, **20**, 509–516 (2001).

[13] Vanderbilt R. T.: The Vanderbilt rubber handbook (13th Edition). R. T. Vanderbilt Co. Ltd., Norwalk (1990).

[14] Byers J. T.: Silane coupling agents for enhanced silica performance. Rubber World, **218**, 38–47 (1998).

[15] Sirisinha C., Sae-oui P., Guaysomboon J.: Mechanical properties, oil resistance and thermal aging properties in CPE/NR blends. Journal of Applied Polymer Science, **84**, 22–28 (2002).

eXPRESS Polymer Letters Vol.1, No.1 (2007) 15–23
Available online at www.expresspolymlett.com
DOI: 10.3144/expresspolymlett.2007.4

A continuum damage model to simulate failure in composite plates under uniaxial compression

D. Tumino[*], *F. Cappello, G. Catalanotti*

Dipartimento di Meccanica, Universita' degli Studi di Palermo, V.le delle Scienze - 90128 Palermo, Italy

Received 17 October 2006; accepted in revised form 9 December 2006

Abstract. Experimental investigations and numerical simulations are performed in order to numerically predict the buckling behaviour of thin composite laminated specimens. Experiments are aimed at two objectives: the first is to completely characterize the carbon/epoxy material under simple loading configurations, the second is to test this material in buckling and post-buckling situations. The data collected with the first campaign of experiments are used to obtain the strength parameters required to define a damage model based on the failure theory by Tsai-Wu. This model is implemented in a Finite Element (FE) code and numerical simulations of buckling are executed for unidirectional and cross-ply laminates; results are in good agreement with experiments both in terms of determination of the critical loads and prediction of failure during post-buckling.

Keywords: *polymer composites, mechanical properties, modelling and simulation*

1. Introduction

The diffusion of composite materials in several fields of engineering and their application to important aspects of human lives are only few reasons for the relevance of the complete comprehension of their behaviour. Differently from conventional materials, composites are subjected to particular damaging processes that lower their capabilities up to their final failure. Carbon Fibre Reinforced Plastics (CFRP) are widely used for hi-tech applications in mechanics, aeronautics and astronautics especially because, compared to conventional materials, they offer a higher specific modulus of elasticity. They are often used as thin plates or as slender beams.

When dealing with thin components, problems arise if compressive conditions are present, because small values of loads can cause instability and then failure of the material at lower load levels than those predicted by compressive strength. Different consequences of such phenomenon can be found: matrix failure, fibres failure, interlaminar delamination.

For beam-shaped isotropic structures these critical loads can be evaluated with the Euler's theory [1] or with more sophisticated shear-deformation theories [2, 3]. Analytical results carried out for laminated composites, are often affected by an overestimation of the critical loads [4]. Factors like orthotropy, asymmetry in traction-compression, edge effects or local damaging can provoke great differences between buckling tests and analytical theories.

Improvements are offered by numerical FE simulations [5–7] by which laminated composites can be reproduced with their intrinsic orthotropic behaviour. With FEM two different approaches can be adopted to solve buckling problems: linear and non-linear ones [8]. Linear buckling furnishes information when the structure has reached the neutral equilibrium between external loads and

---

[*]Corresponding author, e-mail: tumino@dima.unipa.it

elastic reactions (bifurcation point), under the assumptions that the load-displacements diagram is linear as load increases and large displacements occur just at the buckling moment. Non-linear buckling with FEM allows one to consider the presence of large deflections and damaging of material; this means that not only the bifurcation point but also pre- and post-buckling phases can be studied without any restrictive hypothesis. A previous work by the authors [8] demonstrates the influence of orthotropy, edge effect and stacking sequence of the plies on the lowering of the critical load predicted by analytical theories.

In this work a continuum damage model is proposed, based on the failure criterion by Tsai-Wu, to reproduce local damaging of composites. This model, together with an unsymmetric traction-compression constitutive model, is applied to the simulation of buckling and post-buckling of CFRP specimens. Results obtained by characterization tests give the parameters required to completely define the model. This model is used to study the buckling and post-buckling behaviour of composites. Results obtained by FEM simulations are compared with experimental tests on unidirectional and cross-ply laminates.

2. Method

Several failure criteria are available for composite materials, based on principles like the maximum stress, maximum strain or maximum energy for deformation [9]. Simple criteria like the maximum stress (or strain) state that failure occurs when the stress (or the strain) in one of the principal directions of the material reaches a limit value (assumed as the same in traction and compression). A more sophisticated criteria is the one by Tsai-Hill where failure is supposed to occur when an energy-related expression is satisfied; with this criterion the interaction between the various components of stress is accounted for.

Tsai-Wu criterion can be expressed in terms of stress or strain [10]; in this work the second formulation is used, where the failure condition can be written as:

$$\begin{aligned}\Psi = G_{11}\varepsilon_1^2 + 2G_{12}\varepsilon_1\varepsilon_2 + G_{22}\varepsilon_2^2 + \\ G_{66}\gamma_{12}^2 + G_1\varepsilon_1 + G_2\varepsilon_2 = 1\end{aligned} \quad (1)$$

where Ψ is the Tsai-Wu index, G_{ij} and G_i are known as strength parameters and are characteristic of the material; they can be related to experimental data from six types of test by measuring the level of strain at failure in cases of: traction and compression in longitudinal direction (direction 1), traction and compression in transversal direction (direction 2), pure shear and biaxial state. The following relations are used to estimate these parameters:

$$G_{11} = -\frac{1}{\varepsilon_{1uT}\varepsilon_{1uC}};\; G_1 = \frac{1}{\varepsilon_{1uT}} + \frac{1}{\varepsilon_{1uC}} \quad (2\text{ a,b})$$

$$G_{22} = -\frac{1}{\varepsilon_{2uT}\varepsilon_{2uC}};\; G_2 = \frac{1}{\varepsilon_{2uT}} + \frac{1}{\varepsilon_{2uC}} \quad (3\text{ a,b})$$

$$G_{66} = \frac{1}{\gamma_{12u}^2} \quad (4)$$

where ε_{iuT} (for i=1, 2) is the strain at failure in uniaxial traction, ε_{iuC} (for i=1, 2) is the strain at failure in uniaxial compression, γ_{12u} is the strain at failure in pure shear.

The term G_{12} must be obtained from biaxial tests, but is usually taken as either of the following two values:

$$G_{12} = 0 \;\text{ or }\; G_{12} = -0.5\sqrt{G_{11}G_{22}} \quad (5\text{ a,b})$$

2.1. Damage Mechanics

We consider a volume of material free of damage if no cracks or cavities can be observed at the microscopic scale. The opposite state is the fracture of the volume element. The theory of damage describes the phenomena between the virgin state of the material and the macroscopic onset of crack [11, 12]. The volume element must be of sufficiently large size compared to the inhomogeneities of the composite material. In Figure 1 this volume

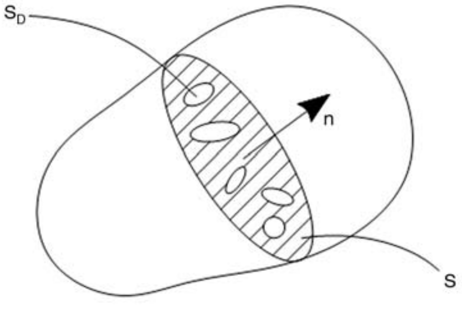

Figure 1. Representative volume element for damage mechanics

is depicted. One section of this element is related to its normal and to his area S. Due to the presence of defects, an effective area for resistance can be found. The total area of defects, therefore, is:

$$S_D = S - \tilde{S} \tag{6}$$

The local damage related to the direction $\mathbf{n}$ is defined as:

$$D_n = \frac{S_D}{S} \tag{7}$$

Under the hypothesis of isotropic damage, the dependence on the normal $\mathbf{n}$ can be neglected, i.e.:

$$D = D_n \forall \mathbf{n} \tag{8}$$

The damage D is a scalar assuming values between 0 and 1. For D=0 the material is undamaged, for 0<D<1 the material is damaged, for D=1 complete failure occurs.

The definition of damage leads to the introduction of the effective stress $\tilde{\sigma}$:

$$\tilde{\sigma} = \frac{\sigma S}{\tilde{S}} = \frac{\sigma}{(1-D)} \tag{9}$$

where σ is the nominal stress.

Assuming that the strain is affected only by the effective stress [11], we can write for uniaxial stress state:

$$\varepsilon = \frac{\tilde{\sigma}}{E} = \frac{\sigma}{(1-D)E} \tag{10}$$

Rewriting Eq. (10) as:

$$\sigma = E(1-D)\varepsilon = \tilde{E}\varepsilon \tag{11}$$

we can treat $\tilde{E}$ as the elastic modulus of the damaged material.

The quantitative evaluation of damage is not a trivial issue, it must be linked to a variable that is able to characterize the phenomenon. Several papers can be found in literature where the constitutive equations of the materials is function of a scalar variable of damage. Most of these works [11–14] assume that the damage is related to an equivalent expression of the strain and to the load-history of the material. In [15] a damage loading function f is defined as a threshold domain that the equivalent strain has to cross in order to generate damage in the material. In the works above mentioned, isotropic damage is considered. An orthotropic formulation of the damage can be found in [16] where different aspects of composite damaging are studied, i.e. debonding, matrix and fibre cracking.

In the present work we propose to link the damage D not directly to an equivalent expression of the strain but to the Tsai-Wu index Ψ, that, as mentioned before, is an entity representing the multiaxial strain state in a composite material and is tightly related to the experimental values of strength at failure. The crucial point is how to relate the damage D to the index Ψ. To do that, a simple power law is adopted:

$$D = \Psi^{\alpha} \tag{12}$$

where the parameter α must be tuned with experimental data obtained from characterization tests. Due to the definition of Ψ given in Eq. (1), Eq. (12) can be interpreted as a strain-based expression of the damage.

Because of the brittle behaviour characteristic of composite materials, damaging process should be represented in a way that once damage starts to grow then failure occurs very rapidly. Let us consider, for example, the case of uniaxial traction in direction 1, with the simplified assumption that $\varepsilon_{1uC} = -\varepsilon_{1uT}$. Replacing Eq. (2a) and (2b) in Eq. (1), we have:

$$\Psi = \left(\frac{\varepsilon_1}{\varepsilon_{1uT}}\right)^2 \tag{13}$$

Then, dividing both terms of Eq. (11) by ε_{1uT} and substituting Eq. (12), we can write:

$$\frac{\sigma_1}{E_{11}\varepsilon_{1uT}} = (1-D)\frac{\varepsilon_1}{\varepsilon_{1uT}} = \left[1 - \left(\frac{\varepsilon_1}{\varepsilon_{1uT}}\right)^{2\alpha}\right]\frac{\varepsilon_1}{\varepsilon_{1uT}} \tag{14}$$

In Figure 2, Eq. (14) is plotted for different values of α. The plot clearly explains how for very high values of α the damage model based on the Tsai-Wu index approaches to the maximum stress (or strain) failure criterion (MSC). An optimal value for α must be chosen considering two different aspects: high values well represent the brittle failure mechanism of composites, small values simplify the computational procedure. Furthermore, in order to satisfy the condition of isotropy, α must be unique and independent from the direction of the material.

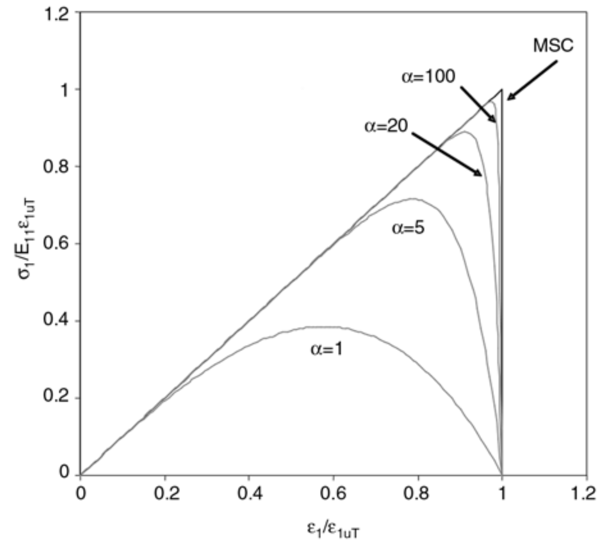

Figure 2. Constitutive model with damage for different values for α

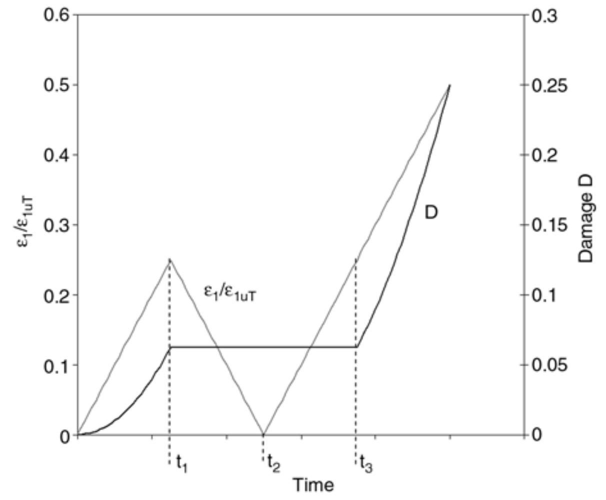

Figure 3. Deformation and related damage history with time (α=1)

Another important characteristic of this damage formulation is its irreversibility: D must grow monotonically from 0 to 1. In Figure 3 is reported an example of the damage history related to the strain history with time: D increases with $\varepsilon_1/\varepsilon_{1uT}$ (time 0–t_1), then as $\varepsilon_1/\varepsilon_{1uT}$ decreases D is constant (t_1–t_2), also when $\varepsilon_1/\varepsilon_{1uT}$ restarts growing D is constant (t_2–t_3); in the last interval (t_3–t_4), D and $\varepsilon_1/\varepsilon_{1uT}$ increase.

3. Results

The material used for the test is a carbon-epoxy composite, obtained laminating the dry patches of carbon fibre by PROCHIMA s.n.c., with an epoxy resin by MATES Italiana s.r.l.. The unidirectional 12-laminae plate so obtained is cured at room-temperature for 12 hours and then at 60°C for 12 hours. The specimens are machined from the original plate and instrumented with strain gauges. A cross-ply laminate is also manufactured with a $[0/90]_{3s}$ lay-up. A small difference in the fibre volume fraction is observed: $V_f = 50\%$ for the unidirectional laminate, while $V_f = 42\%$ for the cross-ply laminate.

3.1. Characterization tests

Elastic characteristics of the material are found by testing specimens whose geometric dimensions are indicated by the ASTM standards [17–19]. In Table 1, these characteristics are summarized for the unidirectional material. A slight difference between the modulii in traction and compression can be noticed. This can be due to the crimped aspect of the fibres and is the reason for the need of an unsymmetric traction-compression constitutive model for the FEM analyses. To obtain the strength parameters defined in Eq. (2, 3, 4), five test are performed on the material (G_{12} is estimated via Eq. (5b) because of the great difficulty in running a biaxial strain test): traction and compression in longitudinal direction 1, traction and compression in transversal direction 2 and pure shear. The ultimate values of deformation measured by the gauges at failure are reported in Table 2.

The numerical model previously defined is implemented using a macro routine compiled in the APDL language in the commercial FE code ANSYS®. The characterization tests are simulated in order to find the optimal value for α. The model is meshed using linear 3D brick elements and the undamaged elastic properties of the material are taken from Table 1. The slightly unsymmetric

Table 1. Elastic properties of the unidirectional laminate (superscript *T* for tension, *C* for compression)

$E_{11}^T = 90$ GPa	$E_{11}^C = 83.5$ GPa	$E_{22}^T = E_{33}^T = 9$ GPa	$E_{22}^C = E_{33}^C = 8.5$ GPa
$\nu_{12} = \nu_{13} = 0.23$	$\nu_{23} = 0.3$	$G_{12} = G_{13} = 2.6$ GPa	$G_{23} = 34$ GPa

Table 2. Deformation at failure for the unidirectional laminate (subscript *T* for tension, *C* for compression)

$\varepsilon_{1uT} = 0.9\%$	$\varepsilon_{1uC} = -0.3\%$	$\varepsilon_{2uT} = 0.5\%$	$\varepsilon_{2uC} = -0.6\%$	$\gamma_{12u} = 2\%$

behaviour in traction-compression is also accounted for, defining an internal procedure by which the proper modulus is chosen when the overall stress state in one element is in traction or in compression. The analysis is performed with a nonlinear incremental-iterative procedure. The value α=20 seems to be the best compromise to have accuracy in results and a reasonable computational time. Results, in terms of stress/strain plots, are shown as example in Figure 4 and 5 for the cases of traction in direction 2 and compression in direction 2. A good agreement with experimental results is achieved also for the other tests.

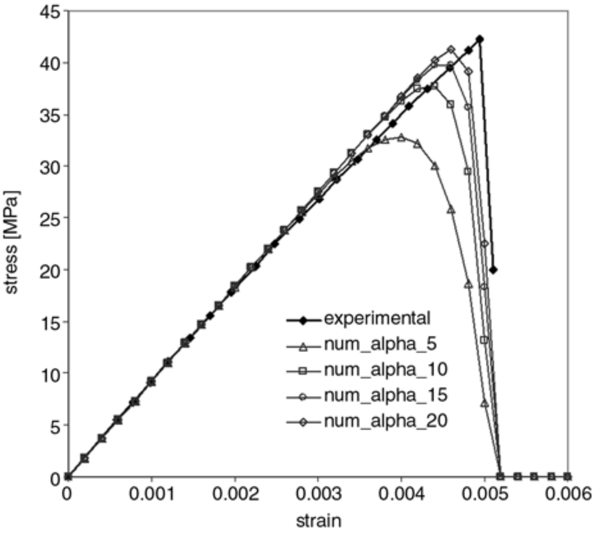

Figure 4. Comparison between experimental results and numerical simulations for tensile test in direction 2

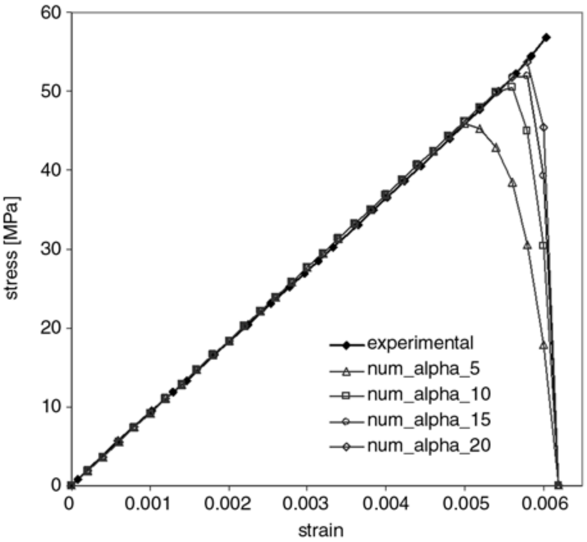

Figure 5. Comparison between experimental results and numerical simulations for compressive test in direction 2

3.2. Buckling tests

The buckling behaviour of thin composite specimens is studied with the aim to numerically reproduce the phenomenon during the entire process, that is pre-buckling, post-buckling and failure. Experimental tests are performed in laboratory with a DC servo-motor testing machine. Two different lay-ups are studied: unidirectional $[0]_{12}$ and cross-ply $[0/90]_{3s}$. The dimensions of the specimens for unidirectional specimens are: gage length $L = 120$ mm (80 mm must be added because of the portion required by the grips), width $B = 15$ mm, thickness $H = 2.65$ mm (Figure 6). For cross-ply specimens the dimensions are: gage length $L = 87$ mm (80 mm must be added because of the portion required by the grips), width $B = 15$ mm, thickness $H = 2.30$ mm. The gage length of the cross-ply specimens has been reduced with respect to unidirectional specimens because the lower value of E_x and of the thickness would lead to very small buckling loads for the cross-ply specimens and the results would be more influenced by possible errors in the experimental setup.

The specimens are fixed at the ends (Figure 7) and the tests are run under displacement control with a constant cross-head speed of 2 mm/min. During the tests the applied axial displacement, the out of plane displacement of the mid-span section and the reaction force of the specimen are recorded.

Five specimens are tested for the unidirectional composite. Each of the diagrams show the typical aspect of the load/displacement plot during a buckling test (Figure 8). During pre-buckling (up to an average applied displacements equal to 0.2 mm)

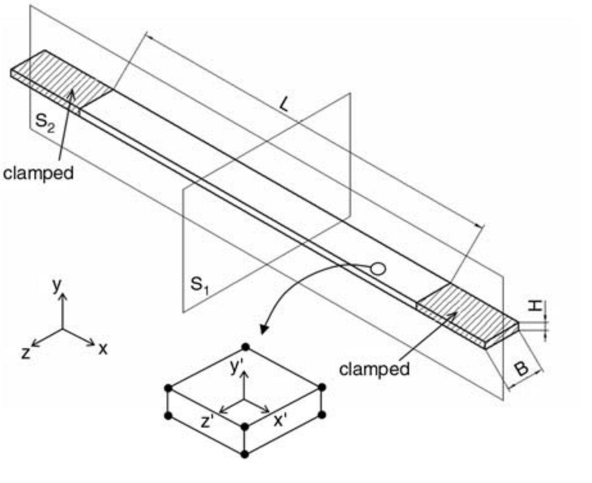

Figure 6. Analysed model (S1 and S2 are planes of symmetry) and a magnified SOLID45

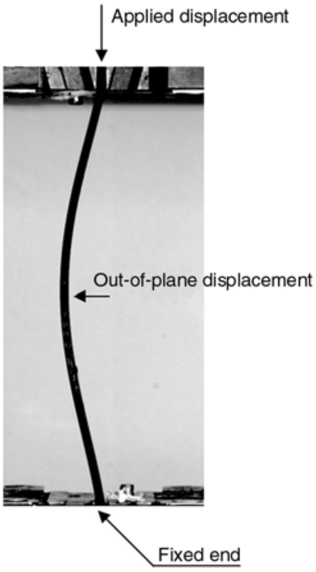

Figure 7. Specimen tested under buckling

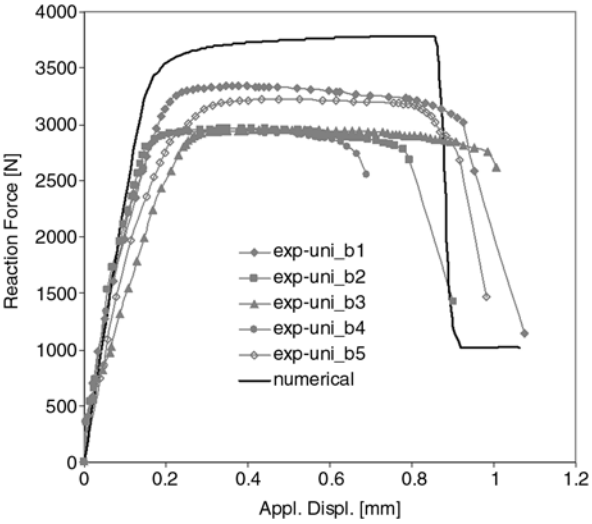

Figure 8. Load/applied displacement diagram for unidirectional specimens: experimental and numerical results

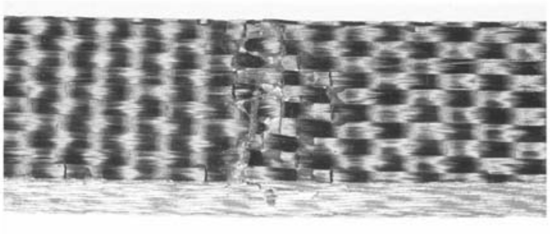

Figure 9. The damaged surface in compression during buckling of a unidirectional specimen

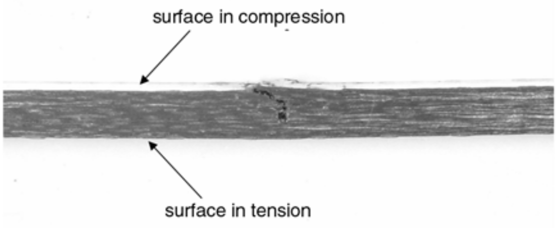

Figure 10. Particular of the through-the-thickness crack of the damaged unidirectional specimen

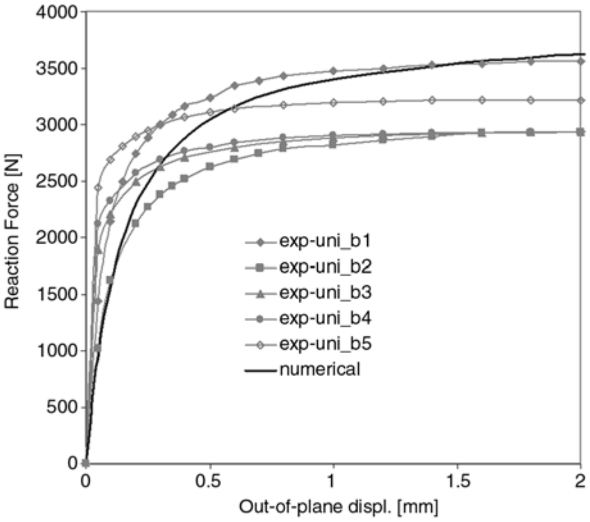

Figure 11. Load/out-of-plane displacement diagram for unidirectional specimens: experimental and numerical results

the reaction force increases pseudo-linearly with the applied displacement. Then, at the moment of buckling, the reaction force reaches a plateau and a macroscopic out-of-plane displacement becomes visible. At the end, the reaction force abruptly drops down when failure occurs in the specimens. A significant scattering in the displacements corresponding to the failure of the specimen is found with values that change from 0.7 mm to 1 mm. The scattering in the buckling load is within the 10% of the average value. Breakage of the material is observed in correspondence of the mid-span section on the side where compression is present. The crack grows very rapidly through the thickness from the side in compression to the side in traction.

Figure 9 shows the cracked region of one specimen (side in compression during buckling): there's no evidence of transverse tensile failure due to the Poisson ratio effect and neither delamination can be observed; a few fibre breakages appear on the surface; the main loss of load-carrying capability is due to the through-the-thickness failure of fibres and matrix, as the close-up in Figure 10 illustrates. Figure 11 shows the reaction force as function of the out of plane displacement of the mid-span section. It is evident that, before buckling occurs, very small displacements can be observed, but, at the moment of buckling, the shape of the specimen changes abruptly and the out-of-plane displacement grows up to the final failure.

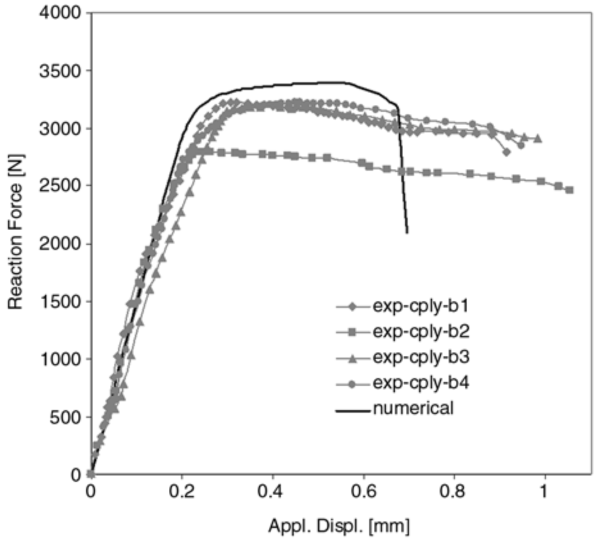

Figure 12. Load/applied displacement diagram for cross-ply specimens: experimental and numerical results

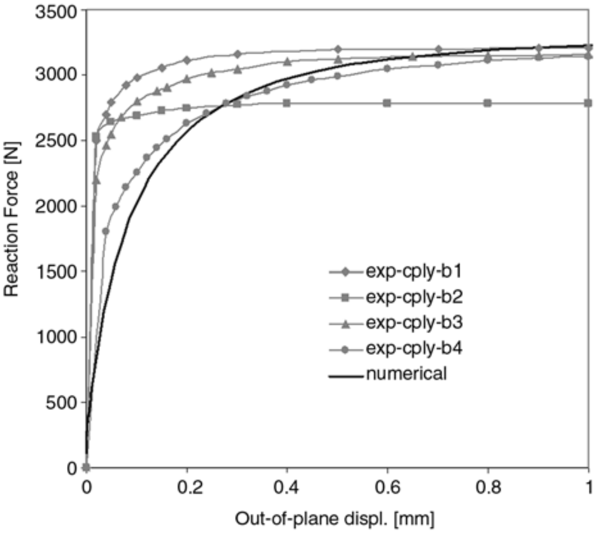

Figure 13. Load/out-of-plane displacement diagram for cross-ply specimens: experimental and numerical results

Similar behaviour is observed for cross-ply specimens. Four specimens are tested and very similar plots are obtained except for the specimen cply_b2 (Figure 12). Differently from unidirectional specimens, failure can be observed both in the mid-span section and in proximity of the grips. The out-of-plane displacements are shown in Figure 13.

3.3. Numerical simulation of buckling tests

The computational effort in FEM simulations can be lowered considering the symmetry of the problem with respect to plane S1 and plane S2 (Figure 6). For both the lay-ups a quarter of the entire model can be modelled. The elements adopted for the mesh are the linear 8-noded bricks SOLID45 and the material is defined as orthotropic whose elastic characteristics are summarized in Table 1. The axis 1 of the composite lamina is aligned with the x' axis of the local coordinate system of the element. Each ply of the laminate is meshed with a layer of bricks with the x' axis aligned to the global x or z axis depending if the lamina is oriented at 0° or 90° respectively. The dimensions of the elements are the result of previous convergence analyses [8]. For an accurate reproduction of experiments, also the clamped region of the specimen is modelled.

In such a situation of symmetry, small unbalance forces are needed to favour the instability. These forces are applied in the mid-span section of the specimens in the y direction and their entity can be quantified around 1/1000 of the critical loads.

Load/displacement responses obtained in the tests are compared with results of FEM analyses in Figure 8 for unidirectional specimens. A good agreement can be observed between the two procedures. The difference between FEM result and the average result from experiments can be calculated as the 16% of the critical load (P = 3700 N from FEM analyses, P = 3100 from experiments), and the displacement at failure from FEM is within the interval 0.7–1 mm observed from tests.

The simple Euler's theory leads to the calculation of the buckling load of a slender beam as follows:

$$P_{Eu} = \frac{4\pi^2 E_{11} I}{L^2} \tag{15}$$

where I is the moment of inertia, is P = 5870 N, definitely higher than the one carried out from tests. We must recall that analytical theory by Euler assumes some simplifications (ideal clamping at the ends, undamaged and isotropic material, validity of the elastic-beam theory) that can cause non-negligible overestimations of the critical load. Furthermore, the finite width effect must be accounted for, as the 3D FEM simulations confirms. In fact if we enlarge the map of the Tsai-Wu index Ψ in proximity of the mid-section (Figure 14) when failure takes place, we could notice a gradient of this index from the plane of symmetry S2 to the free edge. Failure starts to grow from the side in compression to the side in traction, as observed from experiments. In Figure 15 for the

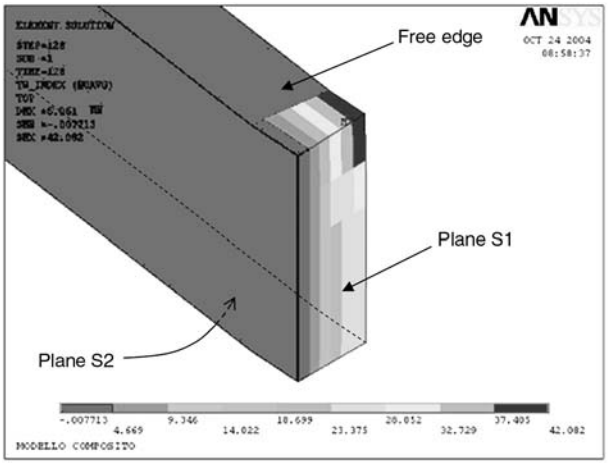

Figure 14. Map of the Tsai-Wu index at failure for a unidirectional specimen: particular in proximity of the mid-span section

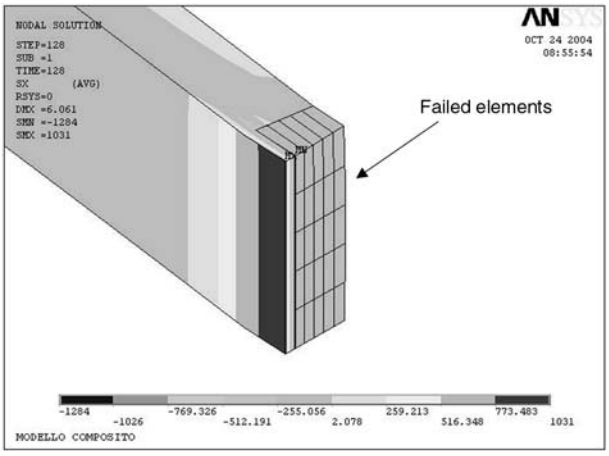

Figure 15. Map of the σ_x stress at failure for a unidirectional specimen: particular in proximity of the mid-span section

same region the map of σ_x stress is reported; all the highlighted elements are completely failed elements (D>1) and their elastic modulus is zero. Figure 13 shows comparison between experiments and simulations for the out-of-plane displacement of the mid-span section. Results are in very good agreement and the numerical plot lies between the experimental ones.

Figure 12 illustrates the load/displacement response of tests on cross-ply laminates compared with results from FEA. A very good correspondence can be observed between the load predicted by the simulations and the load from tests (P = 3300 N from simulations, an average value P = 3200 N from tests). Some differences, on the contrary, can be seen in the displacement at failure, underestimated by FEM. One of the possible reasons for this difference is that the strength parameter related to the biaxial strain at failure is evaluated with Eq. (5b) and is not obtained from tests: due to the different elastic characteristics between laminae at 0° and at 90°, for a cross-ply composite this strength parameter can play a significant role in the failure criterion. It is also remarkable that the zone of failure are similar to the one observed in the tests and are different from those characterizing failure in unidirectional composites. Figure 16 shows the map of the axial σ_x stress in the specimen: the failed regions are located in the mid-span section and in proximity of the grips. In both regions only 0° plies show cracked elements on the surface in compression; these cracks propagate in the axial direction (see highlighted elements). The out-of-plane displacement of the mid-span section is reported in Figure 13: results show that FEM displacement grows more slowly than the test results in the first part of the diagram.

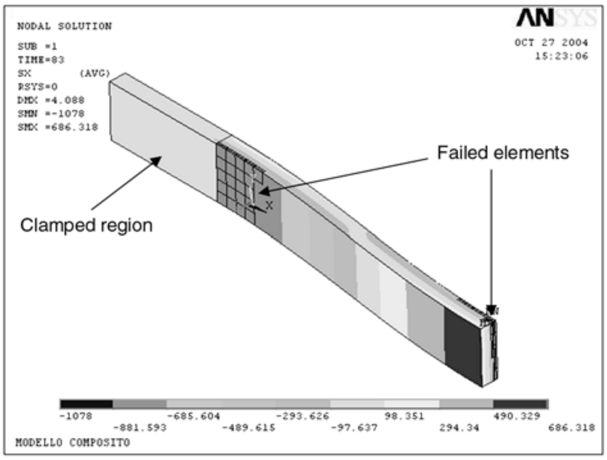

Figure 16. Map of the σ_x stress at failure for a cross-ply specimen

4. Conclusions

In this paper a continuum damage model for composite materials, based on the Tsai-Wu failure criterion, has been developed and implemented in a commercial FE code. This model is completely defined once the strength parameters of the failure criterion are known: to do that, few characterization tests must be done on the material. Buckling behaviour of thin composite specimens has been studied and numerical results have been compared with those carried out from experimental tests. We can summarize the results as follows.

- The proposed numerical model is general and can be adopted to simulate different phenomena involving a progressive damaging of composite materials.

- The power-law adopted to link the damage *D* to the Tsai-Wu index Ψ well suits to simulate a fast-damaging process with small non-linearities (as usual in CFRP), when conveniently high values are used for the exponent α.
- The damage model is isotropic (one value for the exponent α is enough to follow degradation of the composite material in its principal directions) and irreversible (the damage *D* grows monotonically from 0 to 1).
- Experiments of buckling of clamped-clamped composite specimens revealed a great inaccuracy of the Euler's theory for the prediction of the critical load. The overestimation of the load obtained with this approach can cause a wrong design of a structure.
- The good agreement between experimental results and FE results, both for unidirectional and cross-ply laminates, gives reliability to this numerical procedure and affords an accurate prediction of the behaviour of composites when dealing with compression-driven instability.
- Analyses and experiments have been performed on unidirectional and cross-ply laminates. Angle-ply configurations could also be studied with no modification of the formulation. Other materials should be tested in order to understand the general validity of this damage model and the relation between the exponent α and the elastic properties of the material.

References

[1] Kardomateas G. A., Dancila D. S.: Buckling of moderately thick orthotropic columns: comparison of an elastic solution with the Euler and Engesser/Haringx/Timoshenko formulae. International Journal of Solids and Structures, **34**, 341–357 (1997).

[2] Chen H. P.: Shear deformation theory for compressive delamination buckling and growth. AIAA Journal, **29**, 813–819 (1991).

[3] Shu D.: Buckling of multiple delaminated beams. International Journal of Solids and Structures, **35**, 1451–1465 (1998).

[4] Kyoung W. M., Kim C. G.: Delamination buckling and growth of composite laminated plates with transverse shear deformation. Journal of Composite Materials, **29**, 2047–2068 (1995).

[5] Kyoung W. M., Kim C. G., Hong C. S.: Buckling and postbuckling behavior of composite cross-ply laminates with multiple delaminations. Composite Structures, **43**, 257–274 (1998).

[6] Hwang S. F., Liu G. H.: Buckling behavior of composite laminates with multiple delaminations under uniaxial compression. Composite Structures, **53**, 235–243 (2001).

[7] Hwang S. F., Mao C. P.: Failure of delaminated interply hybrid composite plates under compression. Composites Science and Technology, **61**, 1513–1527 (2001).

[8] Cappello F., Tumino D.: Numerical analysis of composite plates with multiple delaminations subjected to uniaxial buckling load. Composites Science and Technology, **66**, 264–272 (2006).

[9] Agarwal B. D., Broutman L. J.: Analysis and performance of fiber composites. John Wiley & Sons, New York (1980).

[10] Swanson S. R.: Introduction to design and analysis with advanced composite materials. Prentice Hall, Upper Saddle River (1997).

[11] Lemaitre J., Chaboche J. L.: Mechanics of solid materials. Cambridge University Press, Cambridge (2000).

[12] de Borst R.: Fracture in quasi-brittle materials: a review of continuum damage-based approaches. Engineering Fracture Mechanics, **69**, 95–112 (2002).

[13] Simo J. C., Ju J. W.: Strain and stress-based continuum damage models, Part I: Formulation. International Journal of Solids and Structures, **23**, 821–840 (1987).

[14] Kwon Y. W., Liu C. T.: Study of damage evolution in composites using damage mechanics and micromechanics. Composite Structures, **38**, 133–139 (1997).

[15] Peerlings R. H. J., Brekelmans W. A. M., de Borst R., Geers M. G. D.: Gradient-enhanced damage modelling of high-cycle fatigue. International Journal for Numerical Methods in Engineering, **49**, 1547–1569 (2000).

[16] Raghavan P., Ghosh S.: A continuum damage mechanics model for unidirectional composites undergoing interfacial debonding. Mechanics of Materials, **37**, 955–979 (2005).

[17] ASTM D3039/D3039M–93. Standard test method for tensile properties of polymer matrix composite materials (1993).

[18] ASTM D3410–87. Standard test method for compressive properties of unidirectional or crossply fiber-resin composites (1987).

[19] ASTM D3846. Test method for in-plane shear strength of reinforced plastics (1994).

eXPRESS Polymer Letters Vol.1, No.1 (2007) 24–26
Available online at www.expresspolymlett.com
DOI: 10.3144/expresspolymlett.2007.5

Cyclic polyesters prepared by poly(oxypropylene oxymaloyl) ring-chain reactions

M. I. Ferrahi[*], M. Belbachir*

Laboratoire de Chimie des Polymères, Département de Chimie, Faculté des Sciences, Université d'Oran Es-Sènia BP N° 1524 El M'Naouar, 31000 Oran Algerie

Received 17 October 2006; accepted in revised form 11 December 2006

Abstract. The synthesis of cyclic polyesters of poly(oxypropylene oxymaloyl) from a ring-chain reaction was carried out at 40°C with 'Maghnite' an acid exchanged montmorillonite as acid solid ecocatalyst (Mag–H$^+$). 'Maghnite' is already used as catalyst for polymerization of many vinylic and heterocyclic monomers [1]. The effect of amount of catalyst on yield and molecular weight of polymer was studied.
A typical reaction product was analyzed by gel permeation chromatography (GPC) as well as by nuclear magnetic resonance spectroscopy (^{1}H–NMR) and the existence of cyclic species was proven.

Keywords: *polymer synthesis, molecular engineering, maleic anhydride, maghnite, montmorillonite, oxypropylene*

1. Introduction

As clay catalysts, montmorillonites a class of inexpensive and non-corrosive solid acids, have been used as efficient catalysts for organic reactions. Montmorillonite catalysts are easily recovered and reused [2–8]. In continuation of our studies on environmentally bening methods using solid supports, we report that acid-exchanged montmorillonite (Mag–H$^+$) is a novel, efficient solid catalyst for the synthesis of cyclic polyesters from ring-chain reaction of poly(oxypropylene oxymaloyl) 'Figure 1'.

In contrast to the more usually used catalyst, Mag–H$^+$ can be easily separated from the polymer and regenerated by heating to a temperature above 100°C. The effect of the relative amounts of Mag–H$^+$ was discussed.

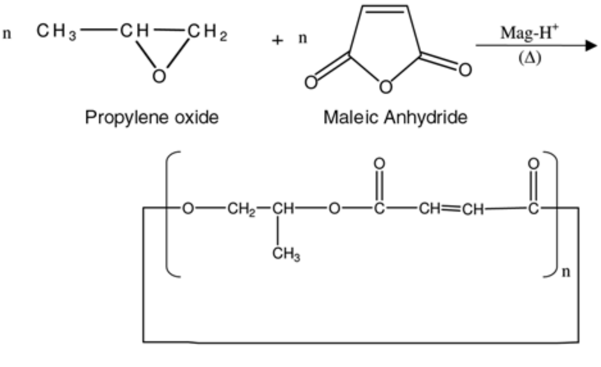

Figure 1. Synthesis of Cyclo Poly(oxypropylene oxymaloyl) by Mag–H$^+$ catalyst

2. Experimental

2.1. Materials

1) 'Maghnite–H$^+$ 0.25M': The preparation of the Mag–H was carried out by using a method similar to that described by Belbachir and al. [1]. Indeed, the raw-Maghnite (20 g) was crushed for 20 min using a Prolabo ceramic balls grinder. It was then dried by baking at 105°C for 2 h. The Maghnite was then weighed and placed in an Erlenmeyer flask together with 500 ml of distilled water. The

---

[*] Corresponding author, e-mail: mohammed.ferrahi@caramail.com

Maghnite/water mixture was stirred using a magnetic stirrer and combined with sulfuric acid, until saturation was achieved over 2 days at room temperature, the mineral was washed with water until it became sulfate free and then dried at 150°C.

The concentration 0.25M of sulfuric acid treatment solution was used to prepare 'Maghnite–H$^+$ 0.25M'.

2) Propylene oxide (99%), Maleic anhydride (99%), Ethanol (99%) and Acetone (99%) were used as received.

2.2. Procedure and Polymer characterization

Polymerizations were carried out in stirred flasks at 40°C. The catalyst was dried in a muffle at 120°C over night and then transferred to a vacuum desiccator containing P_2O_5. After cooling to room temperature under vacuum, the mineral was added to the Propylene oxide (10.85 mol/l), Maleic anhydride(8.54 mol/l) mixture preliminary kept in stirred flask at 40°C. At the required time, an aliquot of the reaction mixture was then taken in such manner as to exclude any clay mineral and slowly added to ethanol with stirring. The precipitated polymer was filtered off and dried under vacuum and weighed. The polymers were redissolved in acetone and precipitated into ethanol for characterization and molecular weight measurement.

Molecular weights were determined by a Waters high pressure GPC instrument (Model 6000A Pump) having a serie of ultra-Styragel columns (100, 500, 103, 104, 105 Å), a Differential Refractometer 2401 and a UV absorbance Detector Model 440. The flow rate of tetrahydrofuran (THF) was 1 ml/min. The calibration curve was made with well-fractionated Poly(oxybutylene oxymaleoyl) standards.

^{1}H–NMR spectra were recorded on an AM 300 FT Bruker instrument using deuterated acetone as solvent, and tetramethylsilane (TMS) as internal standard.

3. Results and Discussion

3.1. Polymerization and Product Characterization

The results of bulk polycondensation experiments of 10.85 M Propylene oxide with 8.54 M maleic anhydride induced by 'Maghnite–H$^+$ 0.25M' are reported in Table 1. For all these experiments the temperature was kept constant at 40°C for 6 hours.

Table 1. Polycondensation of Propylene oxide with maleic anhydride induced by 'Maghnite–H$^+$ 0.25M'

Experiment	'Maghnite–H$^+$ 0.25M' [%]	Yield [%]	Mn	M_w	M_w/M_n
1	15	50.2	549	1825	3.32
2	10	42.7	641	2971	4.63
3	5	31.5	735	3758	5.11
4	2.5	17.2	823	4685	5.69

3.2. Effect of the amount of Mag–H on the polymerization

We can see from Table 1 that the yield increases as the proportion of 'Maghnite–H$^+$ 0.25M' increases. However the molecular weight decreases (experiments 1, 2, 3, 4). Table 2 shows the effect of the amount of Mag–H on the polymerization yield. Indeed, using various amounts of Mag–H: 2.5, 5, 10 and 15% by weight, the polymerization was carried out in bulk at 40°C. The polymerization yield increased with the amount of Mag–H, thus clearly showing the effect of Mag–H as a catalyst. This phenomenon is probably the result of an increase in the number of 'initiating active sites' responsible of inducing polymerization, a number that is prorata to the amount of catalyst used a reaction.

3.3. Characterization of products

An investigation was devoted to the analysis of the polymer from experiment 4 in Table 1 by 300 MHz ^{1}H–NMR spectroscopy (Figure 2).

According to the work published by Hamilton and Semlyen [9] and Vivas and Contreras [10] the 300 MHz ^{1}H–NMR spectra (in deuterated acetone, Figure 2) showed four sets of peaks, corresponding to the methyl group at 1.45 ppm, the β methylene

Table 2. Yields with time for 10.85 mol/L of Propylene oxide, 8.54 mol/L of maleic anhydride, the amounts of Maghnite–H$^+$ 0.25M were: a) 2.5%, b) 5%, c) 10%, d) 15%

Yields [%]	Time [hours]					
	1	2	3	4	5	6
a	8.5	10.8	12.7	13.5	15.2	17.2
b	12.5	16.7	21.6	24.8	28.4	31.5
c	21.7	24.5	28.7	32.8	37.2	42.7
d	27.8	30.5	34.3	39.9	46.2	50.2

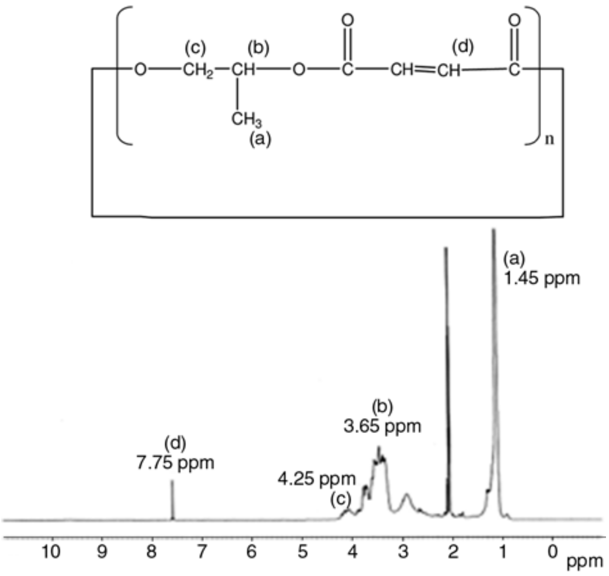

Figure 2. ^{1}H–NMR spectra of the cyclic poly(oxypropylene oxymaloyl)product of experiment 4 in Table 1

groups at 3.65 ppm, the α methylene groups at 4.25 ppm, and the ethylene groups at 7.75 ppm, respectively.

4. Conclusions

The present work shows that the preparation of cyclic polyesters of poly(oxypropylene oxymaloyl) can be induced in heterogenous phase by proton exchanged montmorillonite clay called Maghnite (Mag–H$^+$). The catalytic activity of this catalyst measured by the yield and the molecular weight of the formed polymer, depends on the proportion of catalyst in the reaction medium, cyclic polyesters of poly(oxypropylene oxymaloyl) was produced by a very simple procedure, just by filtering, the clay can be separated from the reaction mixture, and acidic clay is inexpensive, stable and non corrosive.

References

[1] Belbachir M., Bensaoula A.: Composition and method for catalysis using bentonites. US6274527, U.S.Patent (2001).

[2] Yahyaoui A., Belbachir M., Hachemaoui A.: Cationic polymerization of 1,2-epoxypropane by an acid exchanged montmorillonite clay in the presence of ethylene glycol. International Journal of Molecular Science, **4**, 572–585 (2003).

[3] Ballantine J. A., Davies M., Purnell H.: Chemical yields using sheet silicates: novel interlamellar dehydrations of alcohols to ethers and polymers. Journal of Chemical Science. Chemistry Communications, **6**, 427–428 (1981).

[4] Odian G.: Principles of polymerization. Wiley, New York (1991).

[5] Madejovà J., Bednànikovà E., Komadel P., Cicel, B.: in Proc. 11th Conference of Chemistry, Miner and Petrol, Ceske Budéjovica 1990. Ed. J. Konta. Charles University, Prague, 267 (1993).

[6] Ferrahi M. I., Belbachir M.: Polycondensation of tetrahydrofuran with phthalic anhydride induced by a proton exchanged montmorillonite clay. International Journal of Molecular Science, **4**, 312–325 (2003).

[7] Ferrahi M. I., Belbachir M.: Synthesis of cyclic polyesters of poly(oxybutylene oxymaleoyl). Journal of Polymer Research, **12**, 167–171 (2005).

[8] Ferrahi M. I., Belbachir M.: Preparation of poly(oxybutyleneoxymaleoyl) catalyzed by a proton exchanged montmorillonite clay. Molecules, **9**, 968– 977 (2004).

[9] Hamilton S. C., Semlyen J. A.: Cyclic polyesters: 5. Cyclics prepared by poly(decamethylene terephthalate) ring-chain reactions. Polymer, **38**, 1685–1691 (1997).

[10] Vivas M., Contreras J.: Ring-opening polymerization of ε-caprolactone initiated by diphenylzinc. European Polymer Journal, **39**, 43–47 (2003).

eXPRESS Polymer Letters Vol.1, No.1 (2007) 27–31
Available online at www.expresspolymlett.com
DOI: 10.3144/expresspolymlett.2007.6

On the friction and sliding wear of rubber/layered silicate nanocomposites

*K. G. Gatos, K. Kameo, J. Karger-Kocsis**

Institut für Verbundwerkstoffe GmbH (Institute for Composite Materials), Kaiserslautern University of Technology,
Erwin Schrödinger Str. 58, D-67663 Kaiserslautern, Germany

Received 26 October 2006; accepted in revised form 11 December 2006

Abstract. The dry sliding and friction behaviors of organoclay modified hydrogenated nitrile (HNBR) and ethylene/propylene/diene (EPDM) rubbers were studied using a pin (steel)-on-plate (rubber sheet) test configuration. It was found that the organoclay modification may improve or deteriorate the resistance to wear of rubbers. The resistance to wear was adversely affected by pronounced intercalation/exfoliation and two-dimensional alignment of the clay layers (i.e. normal to the moving pin). This result is in analogy with the directional dependence of the wear performance of fiber-reinforced composite laminates.

Keywords: *nanomaterials, polymer composites, rubber, wear, organoclay*

1. Introduction

In recent years the research devoted to rubber/layered silicate nanocomposites was focused mainly on different compounding techniques, identifying the mechanisms involved in intercalation/exfoliation, improving the properties (like mechanical, gas barrier, thermal stability) and modifying the vulcanization (e.g. [1–10]). Although the wear of rubber components is of both practical relevance and scientific interest, the wear performance of rubber/layered silicate nanocomposites has scarcely been addressed [11]. By contrast, several papers addressed already the wear performance of 'organoclay'-modified thermoplastics (e.g. [12–13]) and thermosets (e.g. [14–15]).

Unlike to the sliding wear of metals, ceramics or hard polymers, the mechanisms involved in rubber tribology are peculiar [16–17]. As a hard slider (indenter) passes continuously over a rubber surface, it generates a complicated compression-tension strain cycling at the contact and a corresponding stress distribution around the indenter [17–19]. This creates regular folds, which cross the area of contact from compressive (front part) to the tensile zone (rear part), like wrinkles in a carpet. After the slider has passed and the rubber relaxes, the region around these folds turns back creating a characteristic abrasive pattern which is usually observed for rubbers. These 'waves of detachment', hampering true sliding between the surfaces, are often called 'Schallamach's waves' [17–19]. By this way, a saw tooth profile (crack growth) on the abraded rubber surface may form which is also termed 'tongue-like' pattern. The 'tongue-tip' bends backwards during sliding, ruptures and finally, it is peeled off completely. Consequently, as the sliding process of a hard slider on the soft rubber surface is not continuous, stick-slip motion or self-excited frictional vibration can be generated. Therefore, the tribology of elastomers encompasses complex wear mechanisms, which are affected by numerous parameters including also the type of the filler.

---

*Corresponding author, e-mail: karger@ivw.uni-kl.de

2. Experimental

2.1. Materials

For the investigation of the wear performance of rubber/layered silicate nanocomposites, a hydrogenated acrylonitrile/butadiene rubber (HNBR) and an ethylene/propylene/diene rubber grafted with maleic anhydride (EPDM-MA) were selected as matrices. Montmorillonites, unmodified (MMT) and modified with various intercalants (i.e. octadecylamine – ODA; octadecyltrimethylammonium salt – ODTMA; and methyl-tallow-bis(2-hydroxyethyl) quaternary ammonium salt – MTH), served as organoclays. In all rubber composites, produced by melt mixing, the filler content was fixed at 10 parts per hundred rubber (phr). As the compositions of the rubbers were different, 10 phr organoclay in the HNBR and EPDM mixes corresponds to 7.8 and 8.4 wt%, respectively. Characteristics of the materials used, their compounding procedure, the sulfur curing recipes, the characterization techniques along with the related results are described elsewhere for the rubber nanocomposites produced [20–22].

2.2. Tests

The wear characteristics were determined in a pin-on-disk type sliding wear test, where the disk was the rubber specimen and the counterpart was a steel pin (316L stainless steel, 17-12 Mo). This configuration is also referred as 'pin-on-plate'. The pin ended in a hemisphere with a radius of curvature of 1.5 mm. The applied normal force and sliding velocity were 3 N and 0.25 m/s (144 revolutions per minute on the related tribometer), respectively. Tests were run at T=23°C at 50–70% relative humidity. The density of the rubbers was determined by the Archimedes buoyancy method and their hardness with a Zwick Shore A tester (Ulm, Germany). The specific wear rate, given by the ratio of volume loss to the constant normal load (i.e. 3 N) multiplied by the overall sliding distance, was computed accordingly.

3. Results and discussion

3.1. HNBR micro- and nanocomposites

As presented in Table 1, the HNBR/organo-MMT nanocomposites present enhanced tensile and tear strength values compared to the plain HNBR or the HNBR/MMT vulcanizates. Additionally, an increase in the hardness was observed owing to the clay reinforcement. On the other hand, the high elongation at break values of the compounds were maintained. The damping at 30°C, as it is expressed by the mechanical loss factor value (delivered by dynamic mechanical thermal analysis, DMTA), is increasing for the HNBR/organoclay nanocomposites. The friction coefficient, representing a steady-state value, seems to be comparable for all rubber compounds, which contain MMT regardless of its modification. It is usually claimed that the abrasion of rubber correlates with the ultimate properties (i.e. tensile strength, elongation at break, tear resistance), whereas in respect to wear their fatigue and dynamic mechanical properties are of great importance [16]. Based on this rule of thumb the HNBR/organo-MMT nanocomposites (which fulfill these requirements) should possess excellent resistance to wear. As shown in Figure 1, this is not the case as the specific wear rate increased considerably for the HNBR/organoclay nanocomposites (especially for the HNBR/MMT-ODTMA and HNBR/MMT-MTH systems). The latter nanocomposites present intercalated/exfoliated structures opposed to the intercalated/deintercalated clay populations found in the HNBR/MMT-ODA vulcanizate [20]. On the contrary, for the HNBR/MMT microcomposite (the latter term is due to the fact that in this mixture the MMT was neither intercalated nor exfoliated) a reduced specific wear rate was measured. It was speculated that the reason for

Table 1. Characteristics of HNBR/layered silicate vulcanizates

Property	HNBR	HNBR/MMT	HNBR/MMT-ODA	HNBR/MMT-ODTMA	HNBR/MMT-MTH
Density [g/cm^3]	1.018	1.064	1.051	1.046	1.053
Hardness [Shore A]	60	64	76	75	78
Tensile strength [MPa]	15.2±1.8	19.8±2.0	31.5±1.4	27.6±2.0	31.8±1.0
Elongation at break [%]	675±107	660±26	780±26	707±45	756±40
Tear strength [kN/m]	8.8±1.3	10.3±1.0	42.6±0.6	24.7±1.0	38.6±2.0
tanδ (at 30°C)	0.06	0.09	0.13	0.16	0.19
Friction coefficient	0.41	0.50	0.53	0.53	0.49
Wear test duration [h]	20	20	20	2	3.5

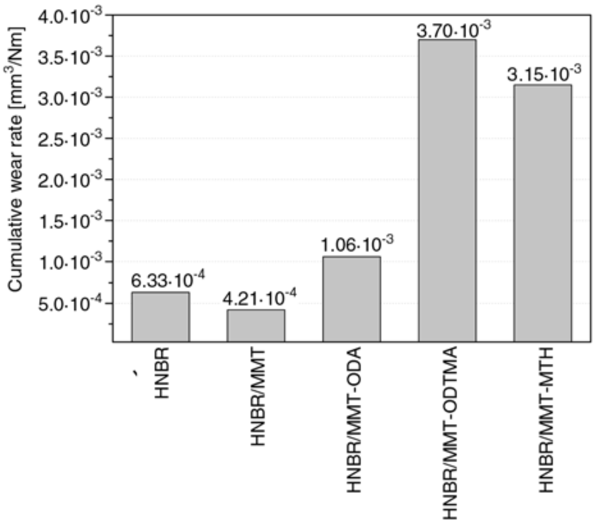

Figure 1. Specific wear rate of HNBR and HNBR containing various (organo)clay fillers in 10 phr amount

this unexpected finding is the dispersion of the silicate layers in the HNBR matrix, which renders the rubber orthotropic owing to a two-dimensional (2D; in-plane) alignment of the clay layers and stacks. The silicate platelets were preferentially aligned parallel to the sliding direction according to transmission electron microscopic (TEM) inspection. This alignment is favored by the sheeting and compression molding of the calendered rubber during vulcanization. The 2D structuring of the clay platelets triggers a mechanism which is similar to a can opening procedure. 'Can-opening' mechanism is at work during the compression-extension strain cycle at the slider contact, and especially at the tensile zone at the rear part of the pin. Albeit the HNBR/MMT microcomposite has a similar friction coefficient as the corresponding nanocomposites (cf. Table 1), it has a lower wear rate compared to the nanocomposites. Note, that in this compound the dispersion of clay agglomerates yields a far less orthotropic behavior compared to the silicate dispersion of the nanocomposites. Additionally, this vulcanizate showed a hardness comparable with that of the pristine HNBR and a relatively low mechanical loss factor above room temperature (however, which is still higher than that of the plain HNBR). Thus, a lower hardness along with an 'isotropic reinforcement' (i.e. a 3D-type instead of a 2D version) may improve the wear performance of rubber/layered silicate systems. It is worth of noting that the above discussion presumes that the state of cure of the HNBR stocks is the same. This was, however, not checked. Further, the HNBR recipe contained substantial amount of plasticizer which might have affected the wear behavior.

3.2. EPDM micro- and nanocomposites

In order to get a clearer picture on this issue additional sliding wear tests were performed on EPDM-MA/organoclay nanocomposites. Table 2 lists the characteristics of the EPDM-MA compounds tested. Note that their hardness is comparable. The ultimate properties of the EPDM-MA/organoclay nanocomposites are enhanced compared to the plain EPDM-MA. Moreover, the distribution of the silicate layers in the EPDM-MA matrix is more random (i.e. 3 D-type yielding an isotropic mechanical behavior) than in the case of the above-mentioned HNBR compounds (cf. TEM images in Refs. [20] and [22]). The reason for this difference is linked with the compression molding procedure. To produce the EPDM-MA compounds attention was paid during sheeting on a two-rolls mill to work with a large opening between the rolls. Thus, a better resistance to abrasive wear was expected via suppressing the processing-induced 2D layering of the organoclay particles causing the above mentioned 'can-opening' mechanism. The slight increase of the hardness of the EPDM-MA nanocomposites contributes additionally to a better resistance to abrasion. Interesting to observe the drastic decrease in the steady-state friction coefficient for the nanocomposites. For the EPDM-MA compound some adhesion between the hard metal slider and the polar EPDM-MA matrix (because of

Table 2. Characteristics of EPDM-MA/layered silicate vulcanizates

Property	EPDM-MA	EPDM-MA/MMT-ODA	EPDM-MA/MMT-ODTMA
Density [g/cm^3]	0.915	0.956	0.965
Hardness [Shore A]	70	74	74
Tensile strength [MPa]	2.7±0.8	12.8±2.1	9.1±0.6
Elongation at break [%]	174±10	292±50	473±20
Tear strength [kN/m]	5.8±0.6	9.4±1.5	9.3±1.2
tanδ (at 30°C)	0.003	0.029	0.053
Friction coefficient	1.05	0.61	0.42
Wear test duration [h]	10	10	8

the maleic anhydride groups) can be supposed. When the EPDM-MA is compounded with the organoclay, the polar maleic anhydride groups are involved in the interactions with the organoclay and thus they affect the adhesion with the metal slider in lesser extent. If this speculation holds then this aspect should also be considered for rubber compounds apart from the abrasive and fatigue type wear contributions. As shown in Figure 2, the specific wear rate of the EPDM-MA/organoclay nanocomposites is below that of the plain EPDM rubber. Scanning electron microscopic (SEM) images taken from the worn surfaces of the rubber plates are very informative (cf. Figure 3). The sliding direction of the pin is indicated in the figures by an arrow. The abraded surface of the EPDM-MA vulcanizate shows a track with rough ridges and dimples. The worn track even suggests the occurrence of some kind of stick-slip mechanism during sliding (cf. Figure 3a). By contrast, the EPDM-MA/organoclay vulcanizates present nicely the ‘Schallamach’s waves’ (cf. Figure 3b and 3c). Note that on the worn surface of EPDM-MA/MMT-ODTMA these ‘waves of detachment’ are smaller and closer packed than for EPDM-MA/MMT-ODA. This may suggests a finer dispersion of the silicate sheets in the former system which was proved, in fact [22]. Recall that the EPDM-MA/MMT-ODA nanocomposite contained also deintercalated organoclay stacks [21]. Swelling tests indicated that the state of cure of the EPDM stocks was practically the same. As a consequence, the effects listed above are likely correctly traced to the dispersion and orientation of the clay layers and aggregates.

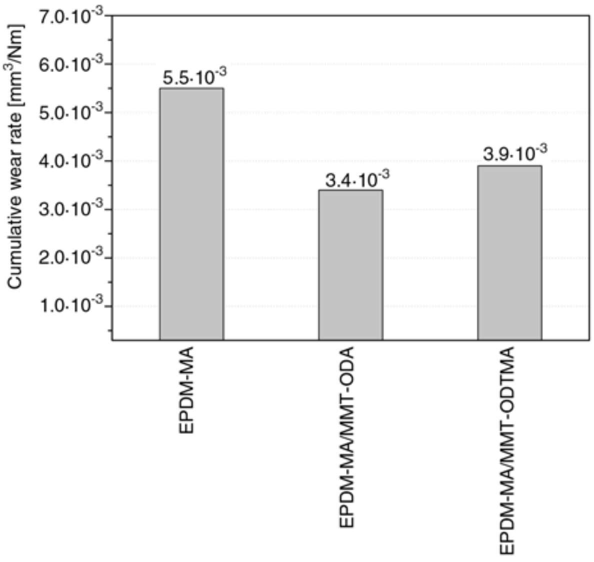

Figure 2. Specific wear rate of EPDM-MA and EPDM-MA/organoclay containing 10 phr filler

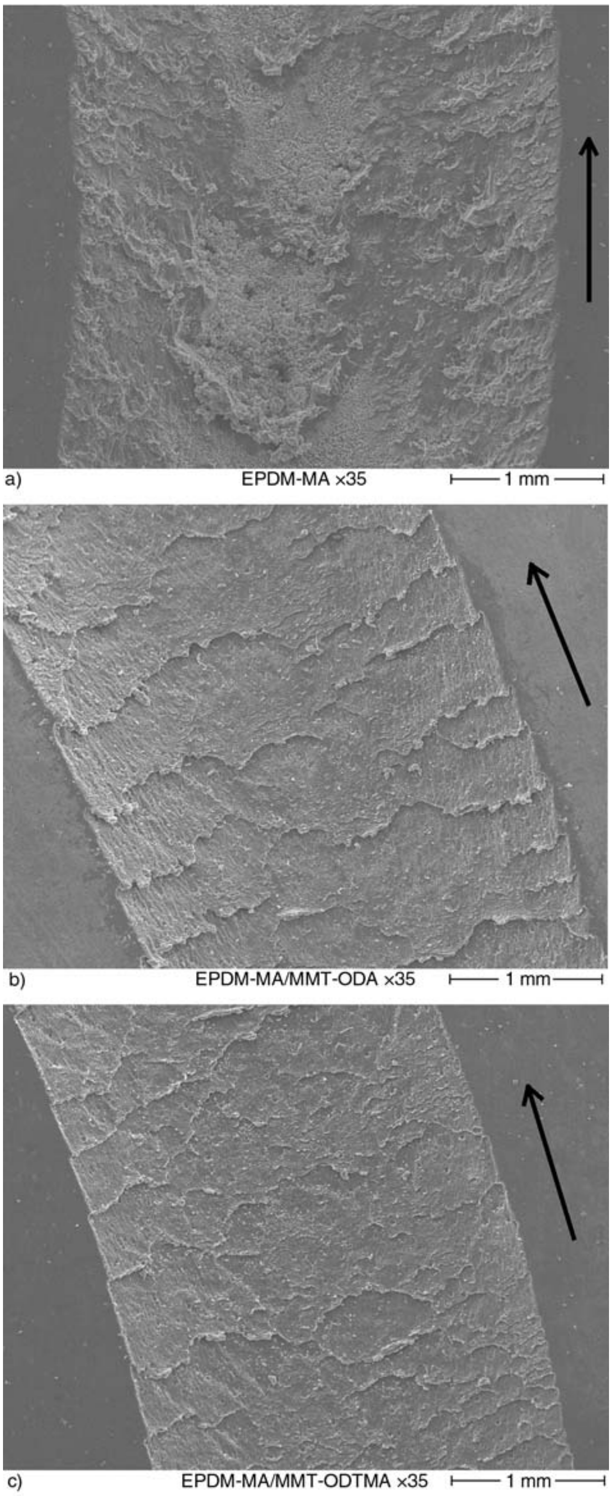

Figure 3. Wear track of EPDM-MA/layered silicate vulcanizates: (a) EPDM-MA, (b) EPDM-MA reinforced with MMT-ODA and (c) EPDM-MA reinforced with MMT-ODTMA.
Note: organo-MMT content is 10 phr

4. Conclusions

Incorporation of layered silicates in rubber can affect the wear performance of the related vulcanizate favorably or unfavorably. The final outcome depends on those parameters, which affect the abrasive, fatigue and adhesive wear components. Note that this is the state-of-wisdom with rubbers containing 'traditional' fillers. Our preliminary results suggest that the dispersion and especially the orientation of the silicate platelets in the rubber matrix are crucial. Alignment of the clay platelets in plane (2D resulting in an orthotropic character), i.e. parallel to the sliding direction may be disadvantageous. The 2D clay alignment triggers a mechanism during sliding, which has some similarities with a 'can-opening' process. This may reduce the resistance to wear markedly.

Acknowledgements

This work was performed in the framework of an Integrated Project of the EU (KRISTAL; Contract Nr.: NMP3-CT-2005_515837)

References

[1] Ganter M., Gronski W., Semke H., Zilg T., Thomann C., Mühlhaupt R.: Surface-compatibilized layered silicates – A novel class of nanofillers for rubbers with improved mechanical properties. Kautschuk, Gummi, Kunststoffe, **54**, 166–171 (2001).

[2] Joly S., Garnaud G., Ollitrault R., Bokobza L., Mark J. E.: Organically modified layered silicates as reinforcing fillers for natural rubber. Chemistry of Materials, **14,** 4202–4208 (2002).

[3] Arroyo M., López-Manchado M. A., Herrero B.: Organo-montmorillonite as substitute of carbon black in natural rubber compounds. Polymer, **44**, 2447–2453 (2003).

[4] Varghese S., Karger-Kocsis J., Gatos K. G.: Melt compounded epoxidized natural rubber/layered silicate nanocomposites: structure-properties relationships. Polymer, **44**, 3977–3983 (2003).

[5] Zheng H., Zhang Y., Peng Z., Zhang Y. X.: Influence of clay modification on the structure and mechanical properties of EPDM/montmorillonite nanocomposites. Polymer Testing, **23**, 217–223 (2004).

[6] Zheng H., Zhang Y., Peng Z, Zhang Y. X.: A comparison between cure systems for EPDM/montmorillonite nanocomposites. Polymers & Polymer Composites, **12**, 197–206 (2004).

[7] Wu Y-P., Ma Y., Wang Y-Q., Zhang L-Q.: Effects of characteristics of rubber, mixing and vulcanization on the structure and properties of rubber/clay nanocomposites by melt blending. Macromolecular Materials and Engineering, **289**, 890–894 (2004).

[8] Karger-Kocsis J., Wu C-M.: Thermoset rubber/layered silicate nanocomposites. Status and future trends. Polymer Engineering and Science, **44**, 1083–1093 (2004).

[9] Hwang W-G., Wei K-H., Wu C-M.: Mechanical, thermal, and barrier properties of NBR/organosilicate nanocomposites. Polymer Engineering and Science, **44**, 2117–2124 (2004).

[10] Liang Y-R., Lu Y-L., Wu Y-P., Ma Y., Zhang L-Q.: Pressure, the critical factor governing final microstructures of cured rubber/clay nanocomposites. Macromolecular Rapid Communications, **26**, 926–931 (2005).

[11] Karger-Kocsis J.: Dry friction and sliding wear behavior of organoclay reinforced thermoplastic polyurethane rubbers. Kautschuk, Gummi, Kunststoffe, **59**, 537–543 (2006).

[12] Lai S-Q., Li T-S., Liu X-J., Lu R-G.: A study on the friction and wear behavior of PTFE filled with acid treated nano-attapulgite. Macromolecular Materials and Engineering, **289**, 916–922 (2004).

[13] Srinath G., Gnanamoorthy R.: Effects of nanoclay reinforcement on tensile and tribo behaviour of nylon 6. Journal of Materials Science, **40**, 2897–2901 (2005).

[14] Jawahar P., Gnanamoorthy R., Balasubramanian M.: Flexural and tribological properties of polyester-clay nanocomposites. Journal of Materials Science, **40**, 4391–4393 (2005).

[15] Lin J-C.: Compression and wear behavior of composites filled with various nanoparticles. Composites: Part B, **38**, 79–85 (2007).

[16] Grellmann W., Heinrich G., Cäsar T.: Crack initiation, wear and molecular structure of filled vulcanized materials. in 'Deformation and fracture behavior of polymers' (eds.: Grellmann W. and Seidler S.), Springer, Berlin, 479–492 (2001).

[17] Zhang S–W.: Tribology of elastomers. Elsevier, Amsterdam, 2004.

[18] Schallamach A.: How does rubber slide? Wear, **17**, 301–312 (1971).

[19] Barquins M.: Adherence, friction and wear of rubber-like materials. Wear, **158**, 87–117 (1992).

[20] Gatos K. G., Sawanis N. S., Apostolov A. A., Thomann R., Karger-Kocsis J.: Nanocomposite formation in hydrogenated nitrile rubber (HNBR)/organo-montmorillonite as a function of the intercalant type. Macromolecular Materials and Engineering, **289**, 1079–1086 (2004).

[21] Gatos K. G., Thomann R., Karger-Kocsis J.: Characteristics of ethylene propylene diene monomer rubbers/organoclay nanocomposites resulting from different processing conditions and formulations. Polymer International, **53**, 1191–1197 (2004).

[22] Gatos K. G., Karger-Kocsis J.: Effects of primary and quaternary amine intercalants on the orgnoclay dispersion in a sulfur-cured EPDM rubber. Polymer, **46**, 3069–3076 (2005).

eXPRESS Polymer Letters Vol.1, No.1 (2007) 32–36
Available online at www.expresspolymlett.com
DOI: 10.3144/expresspolymlett.2007.7

Surface properties of latex film and solvent-borne film resulted from fluorinated acrylate copolymers prepared by emulsion polymerization

*W. Zhang, H. G. Ni, X. P. Wang**

Key Laboratory of Advanced Textile Materials and Manufacturing Technology of Education Ministry, Department of Chemistry, Zhejiang Sci-Tech University, Hangzhou 310018, China

Received 24 October 2006; accepted in revised form 19 December 2006

Abstract. The fluorinated acrylate copolymer, poly (BMA-co-DFHMA), was prepared by emulsion polymerization using a preemulsified monomer addition process. The FTIR and ^{1}H–NMR were used to characterize the copolymer structure. The contact angle of water on the solvent-borne film increased dramatically and reached an equilibrium value (103°) when the PDFHMA content in the copolymer was only 0.97 mol%. However, the contact of water on the latex film increased slowly, and reached the equilibrium value of 99° until the fluorinated component content was as highly as 9 mol%. A similar result was observed for the oil contact angle on the two types of films. XPS results showed that when the F/C ratio on film surfaces reached equilibrium, the required content of fluorinated component in the copolymer for the solvent-borne film was much lower than that for the latex film.

Keywords: *coatings, fluorinated acrylate, surface property, emulsion polymerization*

---

1. Introduction

Due to their low surface free energy and chemical stability in a variety of environments, fluorinated polymers have been widely used as surface coatings of solid materials, such as water and oil repellents for the textile, protection materials for leather and stone, mold releasing agent, and so on [1–4]. Generally, the fluorinated polymers were prepared traditionally by solution polymerization for the theoretical research. However, from the viewpoint of practical applications, it is more desirable to synthesize fluorinated polymer latex. Compared to traditional solvent-base fluorinated polymers, the latex containing fluorine exhibits a variety of advantages such as non-inflammability, non-toxicity, and environmental friendly properties. Until recently, however, the preparation and film-formation of fluorinated polymer or copolymer latex has been paid attention [5–9].

It is well known that the monomers containing fluorine have relatively high price, the incorporation of large amount of fluorinated monomers in the copolymers would impair their market competition. Therefore, it is of great importance to reduce fluorinated component content in copolymers while keeping the excellent surface properties of the resulting copolymer films. Furthermore, it is very necessary to know the influence of the types of the obtained film, i.e. latex film and solvent-borne film, on their surface properties. Unfortunately, such investigation is seldom reported according to our knowledge.

In this paper, a series of fluorinated acrylate copolymers with different content of fluorinated components were prepared by emulsion polymer-

---

*Corresponding author, e-mail: wxinping@yahoo.com

ization, and the surface properties of the latex film and solvent-borne film were examined. The results showed that the solvent-borne film exhibited much more excellent water and oil repellency than the latex film.

2. Experimental

2.1. Materials

Dodecafluorheptyl methylacrylate (DFHMA) was purchased from XEOGIA Fluorine-Silicon Chemical Company, Harbin, China. Its purity was above 97% and used without further purification. The structure of DFHMA was shown in Figure 1. Butyl methacrylate (BMA) was washed by 5 wt% sodium hydroxide solution to remove inhibitor, and then was distilled under reduced pressure. The water-soluble initiator (potassium persulfate, $K_2S_2O_8$) and emulsifiers including sodium dodecyl sulfate (SDS) and dodecyl polyoxy ethylene (OP–10) were used without further purification. The dionized water was obtained by ion exchange. Other chemicals were of reagent grade and used without further purification.

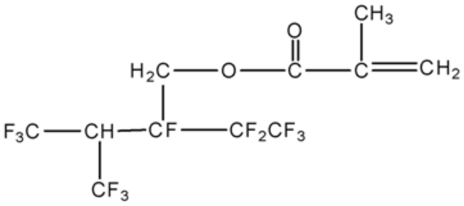

Figure 1. Schematic representation of the DFHMA

2.2. Emulsion polymerization

Emulsion polymerization was carried out in a 100 ml reactor using a typical preemulsified monomer addition process [10]. A typical recipe is: BMA, 20 g; $K_2S_2O_8$, 0.115 g; SDS, 0.07 g; OP–10, 0.18 g; dionized water, 46.7 g. The mol ratio of DFHMA to BMA was changeable and the solid content of the final latex remained about 25 wt%. The synthesis of the poly (BMA-co-DFHMA) latex was performed as follows: part of water, emulsifiers and initiator, and all monomers were emulsified for 30 min by stirring. The obtained monomer emulsion was then charged successively for 2 h into the reactor containing the remaining water, emulsifiers, and initiator at 80°C. After completion of monomer feeding, the reaction lasted for another 2 h.

2.3. Film formation

Latex films were prepared by spreading latexes directly on pre-cleaned glass slides. The films were allowed to dry at 60°C for at least 12 h. For the preparation of the solvent-borne film, the obtained latex particles were firstly precipitated in 5 wt% $CaCl_2$ solution. The obtained precipitates were washed with water several times after filtration. Next, the precipitates were dried under reduced pressure at 40°C. Finally, the dried precipitates were dissolved in cyclohexanone, and the resultant solution was cast on the glass slide. After evaporating the solvent, the solvent-borne film was obtained.

2.4. Characterization

The chemical compositions of the latex particles were determined by a Nicolet Aratar 370 FTIR spectrometer and a Bruker Advance AMX-400 NMR instrument using $CDC1_3$ as solvents. The contact angle on the film surface was measured by the sessile drop method [11] using a KRÜSS (Hamburg, Germany) DSA 10 goniometer. The contact angle reported in this work is the average of the values obtained from at least 8 different points on the film surface. The experimental error for contact angle measurement is within the range of ±1°. The surface chemical compositions of the films were determined by X-ray photoelectron spectroscopy (XPS, PHI 5000C ESCA system, Perkin-Elmer) with a Mg Kα X-ray source (1253.6 eV).

3. Results and discussion

3.1. Characterization of the fluorinated acrylate copolymers

Figure 2 shows the FTIR spectra of (a) poly (BMA-co-DFHMA) and (b) PBMA, respectively. Comparing the FTIR spectra (a) with (b), two new absorption bands are emerged at 692 and 706 cm^{-1}, which was due to the rocking and wagging vibrations of CF_2 groups [12]. In addition, the absorption bands at 1180 and 1220 cm^{-1} are attributed to the C–F bond stretching vibrations [5, 8]. Figure 3 shows the ^1H–NMR spectrum of poly (BMA-co-DFHMA). The peak at 4.3 and 3.9 ppm are observed, which is assigned to the $–OCH_2–$ of DFHMA and BMA, respectively [12]. By evaluating the peak intensities at 4.3 and 3.9 ppm, the mol

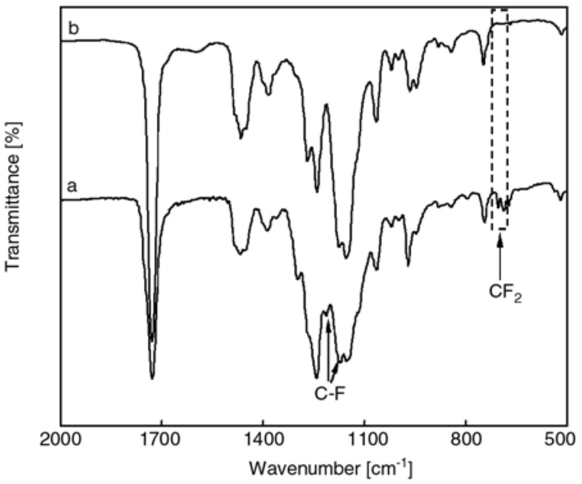

Figure 2. FTIR spectra of (a) poly (BMA-co-DFHMA) and (b) PBMA. The content of DFHMA in the copolymers is 9.5 mol%

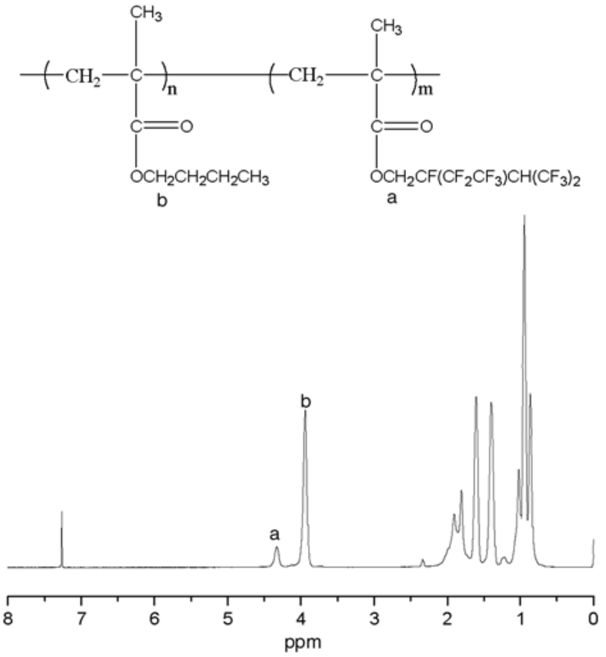

Figure 3. ^{1}H–NMR spectrum of poly (BMA-co-DFHMA). The content of DFHMA in the copolymers is 9.5 mol%

fraction of PDFHMA components in the copolymers can be determined. Moreover, it was found that the prepared poly(BMA-co-DFHMA) was soluble in tetrahydrofuran (THF). This suggested the polymer used in this study was a copolymer since the DFHMA homopolymer could not be dissolved in THF. These results above also indicate that the DFHMA have copolymerized with BMA.

3.2. Surface property of fluorinated acrylate copolymer film

It is well known that fluorinated components content in the copolymers has a significant effect on their surface properties. Figure 4 presents the contact angle of water and paraffin oil on the latex film and solvent-borne film as a function of DFHMA content in the resulting copolymers. As shown in Figure 4a, the contact angle of water on solvent-borne film enhances dramatically from 88.1 to 103° when the DFHMA content increases from 0 to 0.97 mol%, in which the contact angle of water on latex film shows a little increase, i.e. from 81 to 84°. On the other hand, the contact angle of water on solvent-borne film reaches equilibrium when the

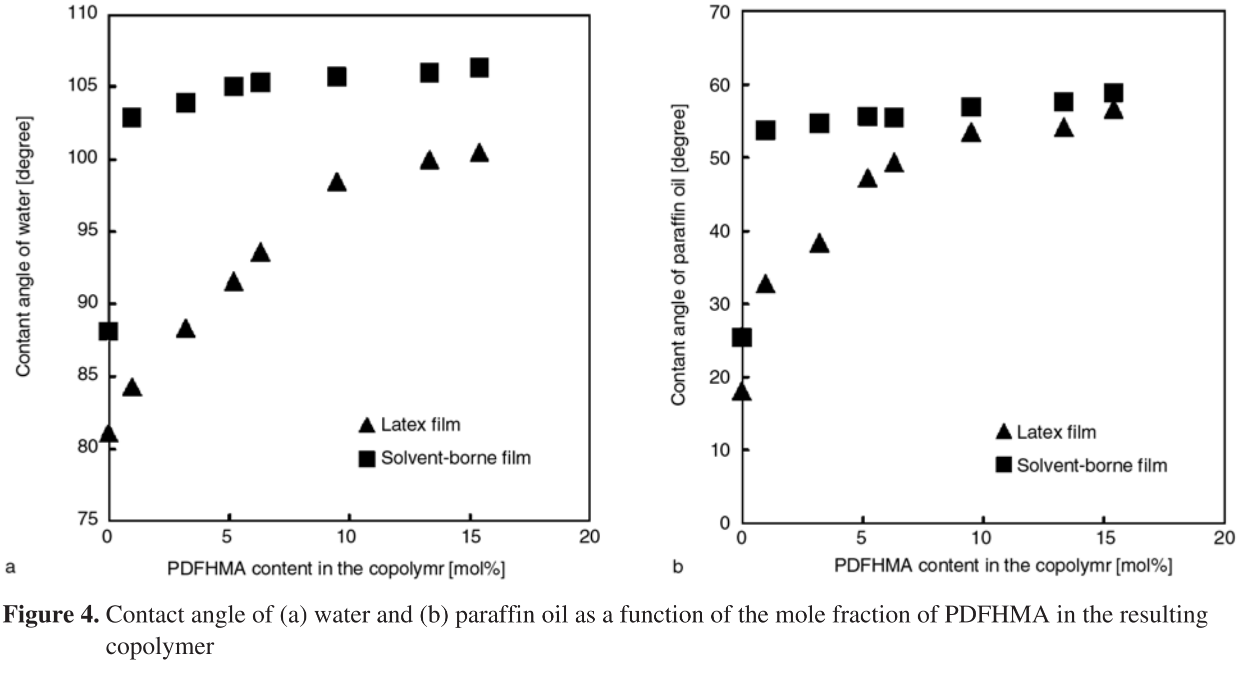

Figure 4. Contact angle of (a) water and (b) paraffin oil as a function of the mole fraction of PDFHMA in the resulting copolymer

DFHMA content is about 5 mol%. However, 9 mol% of DFHMA is required for the contact angle of water on latex film to reach equilibrium. When reaching equilibrium, the contact angle of water for the solvent-borne film is about 103°, whereas that for the latex film is only 99°. Similar results are observed for the contact angle of paraffin oil on the two types of films (see Figure 4b). Obviously, there exists a great difference in surface properties between the solvent-borne film and latex film. Furthermore, it is noted that at low level of fluorinated components, (e.g. lower than 5 mol%), the solvent-borne film exhibits much more excellent water and oil repellency than latex film although both of them have the same chemical composition.

Surface properties of materials are usually governed by the structure and chemical composition of the surface layer. In order to understand well the water and oil repellency of the resulted fluorinated acrylate film, the surface chemical compositions on the two types of films were examined by XPS. Shown in Figure 5 are F/C ratios for a series of poly (BMA-co-DFHMA) copolymers with various content of DFHMA, in which the F/C ratio represents the relative magnitude of fluorine concentration at the film surface. It is clear that the F/C ratios for the solvent-borne film are remarkably higher than that for the latex film at any a given DFHMA content. These differences between the solvent-borne film and latex film may be attributed to their film-formation mechanism. During the film-formation of latex, the perfluoroalkyl groups may be embedded in the latex particle. This limits greatly the occupation of perfluoroalkyl groups on the film surface, and thus the efficiency of fluorine is decreased. Furthermore, F/C ratios for the solvent-borne film remain almost constant when the amount of DFHMA in the copolymers exceeds about 5 mol%, whereas for the latex film, 9.5 mol% PDFHMA is needed. These results correspond well with the contact angle results as shown in Figure 4.

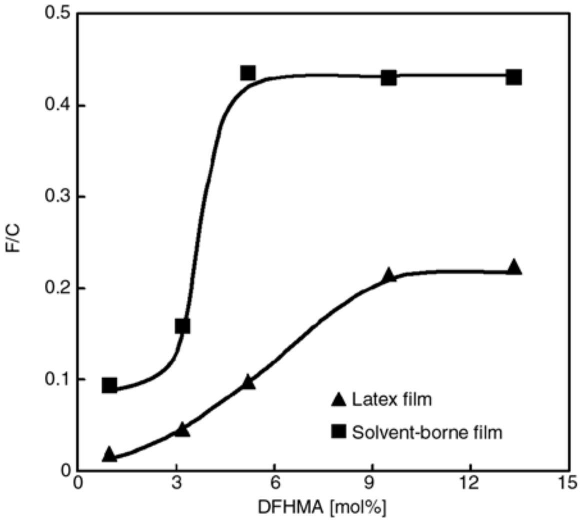

Figure 5. F/C rations at the surface of a series of poly (BMA-co-DFHMA) copolymers with different amount of PDFHMA

As well known, it is of more practical importance to enhance the hydrophobicity and olephobicity of latex film containing fluorine. The contact angle value on the solvent-borne film may be considered as the highest value that the latex film could achieve. The significant surface property gap between the solvent-borne film and latex film provides a potential possibility that the surface property of latex film could be greatly improved. How to improve the surface properties of latex film composed of low level of fluorinated components to the level of the corresponding solvent-borne film will be the focus of the next work.

4. Conclusions

The fluorinated acrylate copolymer, poly (BMA-co-DFHMA), was successfully synthesized by emulsion polymerization using a preemulsified monomer addition process, which was confirmed by FTIR and ^{1}H–NMR. It was found that when the water and oil contact angle reached equilibrium, the required DFHMA content for the solvent-borne film was much lower than that for the latex film. The F/C ratios on the two types of films showed a similar changing trend with the increase of the fluorinated component content. Furthermore, the solvent-borne film, especially at the low level of fluorinated component content, exhibited much more excellent water and oil repellency than the latex film.

The significant surface property gap between the solvent-borne film and latex film indicates that the surface property of the latex film containing lower content of fluorinated components could be further improved to a great degree, which is very important for the practical application of fluorinated acrylate copolymer latex.

Acknowledgments

The authors are grateful for the financial support from the National Natural Science Foundation of China (Grant No. 50573069), the Natural Science Foundation of Zhejiang Province (Grant No. Y405490) and Education Committee of Zhejiang Province (Grant No. 20050785).

References

[1] Hochart F., De Jaeger D., Levalois-Grutzmacher J.: Graft-polymerization of a hydrophobic monomer onto PAN textile by low-pressure plasma treatments. Surface & Coatings Technology, **165**, 201–210 (2003).

[2] Yang S., Wang J. G., Ogino K., Valiyaveettil S., Ober C. K.: Low-surface-energy fluoromethacrylate block copolymers with patternable elements. Chemistry of Materials, **12**, 33–40 (2000).

[3] Benedetti E., D'alessio A., Zini M. F., Bramanti E., Tirelli N., Vergamini P., Moggi G.: Characterization of acrylic resins and fluoroelastomer blends as potential materials in stone protection. Polymer International, **49**, 888–892 (2000).

[4] Gu G., Zhang Z., Dang H., Wu Z.: Preparation of hydrophobic thin films based on PTFE/acrylic resin/ SiO_2 complex. Journal of Materials Science, **39**, 5613–5615 (2004).

[5] Dreher W. R., Singh A., Urban M. W.: Effect of perfluoroalkyl chain length on synthesis and film formation of fluorine-containing colloidal dispersions. Macromolecules, **38**, 4666–4672 (2005).

[6] Ha J-W., Park I. J., Lee S-B.: Hydrophobicity and sliding behavior of liquid droplets on the fluorinated latex films. Macromolecules, **38**, 736–744 (2005).

[7] Sacanna S., Koenderink G. H., Philipse A. P.: Microemulsion synthesis of fluorinated latex spheres. Langmuir, **20**, 8398–8400 (2004).

[8] Chen Y., Cheng S., Wang Y., Zhang C.: Chemical components and properties of core-shell acrylate latex containing fluorine in the shell and their films. Journal of Applied Polymer Science, **99**, 107–114 (2006).

[9] Dreher W. R., Jarrett W. L., Urban M. W.: Stable non-spherical fluorine-containing colloidal dispersions: Synthesis and film formation. Macromolecules, **38**, 2205–2212 (2005).

[10] Yang M-J., Zhang W.: Preparation and properties of silicone-acrylate copolymer latex. Chinese Journal of Polymer Science, **22**, 215–218 (2004).

[11] Sharma A., Thampi S. P., Suggala S. V., Bhattacharya P. K.: Pervaporation from a dense membrane: Roles of permeant-membrane interactions, Kelvin effect, and membrane swelling. Langmuir, **20**, 4708–4714 (2004).

[12] Li K., Wu P., Han Z.: Preparation and surface properties of fluorine-containing diblock copolymers. Polymer, **43**, 4079–4086 (2002).

eXPRESS Polymer Letters Vol.1, No.1 (2007) 37–43
Available online at www.expresspolymlett.com
DOI: 10.3144/expresspolymlett.2007.8

Application of percolation model on the brittle to ductile transition for polystyrene and polyolefin elastomer blends

*Z. Guo, Z. Fang**, *L. Tong*

Institute of Polymer Composites, Zhejiang University, Hangzhou 310027, P. R. China

Received 14 October 2006; accepted in revised form 25 December 2006

Abstract. The percolation model was applied in the study of brittle to ductile transition (BDT) of polystyrene (PS) and polyolefin elastomer (POE) blends. Based on the interparticle distance and percolation model, stress volume (V_s) can be expressed by volume fraction (V_r) and ratio of the diameter of stress volume and the diameter of the domain (S/d). The percolation threshold (V_{sc}) varied from π/6 to 0.65. From the results of the Charpy impact strength of the blends, the percolation threshold for the brittle to ductile transition of PS/POE blend is 14 wt% POE, corresponding to $V_{sc}\approx0.5$, which is consistent with the calculated value of π/6. Morphology observations show that the percolation point is correlated with the phase inversion of the blend.

Keywords: *polymer blends and alloys, percolation phenomenon, brittle to ductile transition (BDT), polystyrene (PS), polyolefin elastomer (POE)*

1. Introduction

The fracture toughness of polymeric materials is a decisive factor in material selection, which is one of the most important mechanical properties that determine whether a polymer can be used as an engineering material. Many effective toughening methods for polymeric materials have been developed in the last years. Rubber toughening is one of the methods successful in toughening brittle or notch sensitive polymers. A great amount of experimental data is available to reveal the toughening mechanism. Many aspects of fracture behavior in polymer blends have been explained phenomenologically on the basis of the Ludwik-Davidenkov-Orowan (L-D-O) hypothesis [1, 2]. On this basis, brittle fracture and plastic flow are viewed as independent processes, giving separate characteristic relations for the brittle fracture stress σ_b and the yield stress σ_y, and the intersection of the σ_b/σ_y curves defines the brittle-ductile transition (BDT) point.

Jang et al. [3–7] attributed the fracture toughness of rubber toughened polymers to a competition between two deformation mechanisms: crazing and shear yielding. When the craze initiation stress σ_{cr} is lower than the shear initiation stress σ_{sh} the failure mode is crazing and brittle fracture occurs. Otherwise, when $\sigma_{sh}<\sigma_{cr}$ shear yielding will be the main deformation mechanism and large energy absorption takes place, resulting in a tough fracture. The test conditions where $\sigma_{sh}=\sigma_{cr}$ define the BDT of the material [8].

Compared with the dispersed particle content and dispersed particle size, Wu [9–12] and Borggreve [13–16] proposed the ‘interparticle distance (*ID*, also called matrix ligament thickness)’ model and found that *ID* is a more important morphology parameter that dominates the BDT of polymer

---

*Corresponding author, e-mail: zpfang@zju.edu.cn

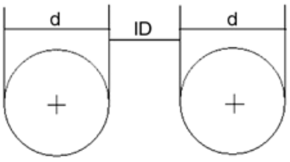

Figure 1. Definition of the interparticle distance (*ID*)

blends. The definition of *ID* is shown in Figure 1, and can be determined from:

$$ID = d\left[\left(\frac{k\pi}{6V_r}\right)^{1/3} - 1\right] \qquad (1)$$

where V_r is the rubber volume fraction, $k = 1$ for cubic packing, d is the rubber particle diameter.

According to Wu, there is a critical value of the interparticle distance (ID_c) when supposing that d is independent of V_r, which can be expressed by:

$$ID_c = d\left[\left(\frac{\pi}{6V_{rc}}\right)^{1/3} - 1\right] \qquad (2)$$

If *ID* is smaller than ID_c, then the blend is tough, otherwise the blend is brittle, namely, the change in *ID* can induce the BDT of polymers. Generally, the ID_c not only depends on the properties of the matrix materials [11, 12, 14], but also depends on the properties of the dispersed phase [13, 15–17]. Moreover, ID_c is also dependent on temperature and rate of deformation [18–20]. At a given mode, rate and temperature of deformation, however, ID_c is independent of particle size and rubber volume fraction and is characteristic for a given matrix [21]. In spite of comprehensive experimental and theoretical studies, the causes why ID_c exist remains unexplained up to now.

Rubber toughened polystyrene has received much attention from both academia and industry for a number of years. [22–33] However, the study on percolation phenomenon of PS and their blends was seldom reported. In this paper, polyolefin elastomer (POE) toughened polystyrene (PS) was used as a model system to explain the percolation phenomenon. SEM and TEM were performed to show the morphology behaviors before and after the percolation threshold. The selective dissolution was used to determine the continuity of POE in the blends.

2. Experimental part

2.1. Materials

Polystyrene (PS, code 666D) was obtained from Yanshan Petrochemical Co. China with a density of 1.05 g/cm^3 (M_w = 310 000; M_n = 87 000; M_w/M_n = 3.6).

Polyolefin Elastomer (POE, code Engage 8150) is a copolymer of octylene and ethylene, obtained from Du Pont-Dow Chemical Co. America with a octylene content of 25% and a density of 0.868 g/cm^3 (M_w = 382 000, M_n = 134 000, M_w/M_n = 2.9).

All the materials and reagents were commercial products and were used without further purification.

2.2. Preparation of the PS/POE blends

Melt blending process was carried out with a twin-screw extruder. The temperatures of the feeding zone, the mix zone, the reaction zone, and the die were 150, 170, 180 and 175°C, respectively. The rotation speed of the screw was 30 rpm. The samples were evacuated at 80°C for one night for drying. Then, the blends were preheated at 170°C in a mold for 5 min followed by compression under 14 MPa for 5 min at the same temperature and subsequently cooled down to room temperature under this pressure.

2.3. Measurements of the mechanical properties

The impact strengths were measured with an XCJ-4 impact instrument (Charpy) according to GB1043-93 (similar to ISO179-1993, 70×6×4 mm^3). All the tests were performed at 25°C. Results of five measurements for each sample were averaged.

2.4. Morphological observations

An SIRION-100 (FEI, USA) scanning electron microscope (SEM) was used to observe the morphology development of PS/POE blends. The specimens were prepared by cryofracture in a liquid nitrogen cooling unit. Then they were covered with a layer of gold to avoid electrical charging to increase contrast during observation.

2.5. Selective dissolution and continuity calculation

The samples were compressed into slices and extracted with *n*-heptane at a bath temperature of 80°C for 48 h in order to dissolve the POE. After dissolution the samples were separated from the solution, dried in a vacuum oven at 70°C for 24 h, and then weighed. Three pieces of each sample were used to obtain an average value.

The percent continuity can be defined as the weight ratio of the POE phase involved in the continuous path divided by the total weight of the theoretical POE phase [34]. The POE phase involved in the continuous path is the dissolved phase:

$$\text{Continuity of POE}\,[\%] = \frac{\text{weight dissolved POE}}{\text{weight of initial POE}} \times 100 \tag{3}$$

where weight of dissolved POE is the weight difference of the sample before and after *n*-heptane dissolution.

3. Results and discussion

3.1. Theory

According to the theory of Wu, the ID_c as a critical thickness for the plane stress to plane strain transition [11]. If the sufficiently neighbored particles automatically lead to a stimulation of local plastic deformations due to overlapping of the local stress concentrations, the material between the particles is in plane stress resulting in macroscopically tough behaviors. However, the dimensions at which the plane stress to plane strain transition occur are of the order of millimeters [35] rather than fractions of a micron as implied by Wu. At sufficiently small particle distances, moreover, the transition from plane strain to plane stress in the matrix ligaments between the particles is also connected with the phenomena of cavitation for the rubber particles. In this context it has been shown by Borggreve and Sjoerdsma et al. [13–17] that cavitation inside the disperse phase and matrix/particle delaminations influence the toughness of the blend together. The original concept by Wu is only related to the matrix but not the characteristics of the disperse phase.

Therefore, the explanation of BDT by Wu's theory is not fully satisfactory. Based on the theory of interparticle distance, in 1988 Margolina [21] proposed the percolation model for brittle-ductile transition in nylon/rubber blends. Margolina theory is based on the assumption that the critical stress necessary for initiation of plastic flow in the matrix is significantly reduced by transition from plane strain to plane stress inside the thin matrix ligaments. Each stress volume centers at a rubber particle and includes a concentric annular shell of the matrix of constant thickness $ID_c/2$, which is the critical ligament thickness, as defined before. When the volume fraction of stress volumes approaches the percolation threshold, stress volumes tend to overlap, allowing the yielding process to propagate and pervade over the entire matrix. Therefore, the diameter of a stress volume as shown in Figure 2 is

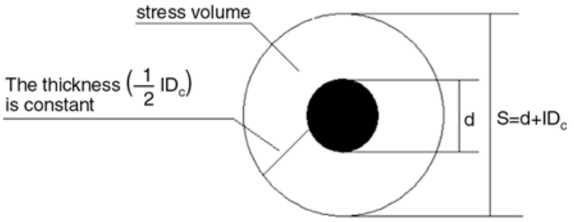

Figure 2. Schematics of stress volume around a rubber particle. The rubber particle is shaded

$$S = d + ID_c \tag{4}$$

where *d* is the diameter of the rubber particle, *S* is the diameter of a stress volume. Moreover, the volume fraction of the rubber particle (V_r) and the volume fraction of the stress volume (V_s) can be calculated by:

$$V_r = \frac{4}{3}\pi\left(\frac{d}{2}\right)^3 \tag{5}$$

$$V_s = \frac{4}{3}\pi\left(\frac{S}{2}\right)^3 \tag{6}$$

Therefore, V_s can be given as:

$$V_s = \left(\frac{S}{d}\right)^3 \cdot V_r \tag{7}$$

Continuum percolation of stress volumes will occur when the volume fraction of the stress volume is at its critical value (V_{sc}).

From Equation 2, 4 and 7, we can obtain

$$V_s = \left(\frac{\pi}{6V_{rc}}\right) V_r \tag{8}$$

when $V_r = V_{rc}$, V_s can obtain a critical value as $V_{sc} = \pi/6 \approx 0.52$ [36].

From Equation 7, we can also obtain that the V_{sc} values tend to vary with S/d rapidly. At $S/d = 1$, the V_{sc} increases to the limit value for random close packing (0.65), i. e. the saturated stress volume. Therefore, the percolation threshold V_{sc} varies from 0.52 to 0.65.

3.2. Brittle to ductile transition in PS/POE blends

Figure 3 reveals the relationship between the mechanical properties and the fraction of POE in PS/POE blends. As shown in the figure, an obvious brittle-ductile transition of PS/POE blends occurs in the Charpy impact tests with the increase of POE content. The value of impact strength nearly unchanged at first and then increased remarkable with increasing POE content. The point where the rubber content was 0.14 by weight, before and after which the impact strength enhanced about 3 folds, seems a critical point at which the transition from brittle to ductile behavior in PS/POE blends occurred.

PS and POE are immiscible. PS/POE blends show sea-iceland structure with PS matrix and POE domain. The volume fraction V_r of the POE can be given by

$$V_r = \frac{W_{POE}\rho_{PS}}{W_{POE}\rho_{PS} + W_{PS}\rho_{POE}} \tag{9}$$

where W_{POE}, ρ_{POE} and ρ_{PS} refer to the weight fraction of the POE rubber, density of the POE and density of the matrix, respectively. For PS/POE blends, $\rho_{POE} = 0.87$ g/cm^3 and $\rho_{PS} = 1.05$ g/cm^3. As shown in Figure 3, the point where the rubber content was 0.14 by weight is a critical point. Therefore, we can estimate from Equation 9 that $V_{rc} = 0.16$. Then, from Equation 8, a curve of the relation between impact strength and V_s can be achieved, as shown in Figure 4. According to the plots, it can be found that the critical V_s, i.e. the percolation threshold V_{sc}, is about 0.53, which is proximate to the theoretical value $\pi/6$, that is, the onset of percolation phenomenon will be observed when POE content was 14 wt%. Moreover, the rapid increase tendency of impact strength with V_s stopped at $V_s = 0.64$, corresponding to the limit value for random close packing (0.65). Thus it is believed that the percolation model is appropriate for the BDT behavior of PS/POE blends and the percolation threshold was between 0.53 and 0.64.

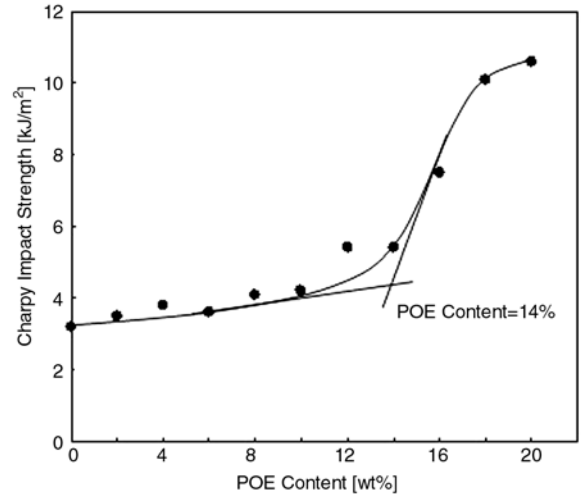

Figure 3. Variation of Charpy impact strength with the POE content [wt%] for PS/POE blends

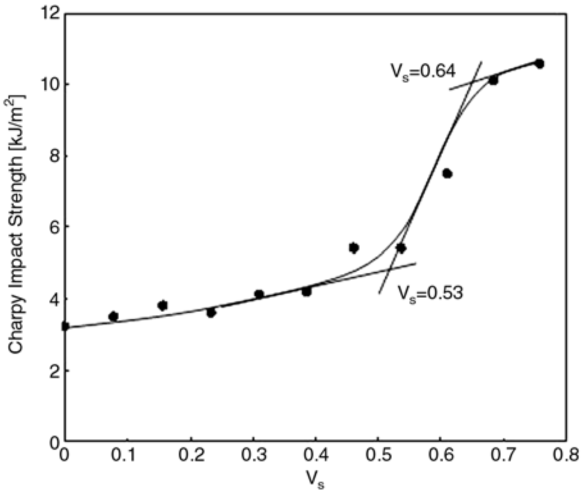

Figure 4. Variation of Charpy impact strength with the fraction of stress volume (V_s)

3.3. Morphology observations

There was an indication of heterogeneous phase structure of PS/POE blends. For this reason, such a blend can be considered as having two phases. Because of poor compatibility between PS and POE components, the dimensions of most POE droplets were big and the size distributions were very wide. The POE phase presents droplets with different sizes in the blend and poor adhesion between phases can be observed. The degree of shear yielding is relatively low; therefore, the crazing mechanisms contribute significantly to the deformation of PS/POE blends.

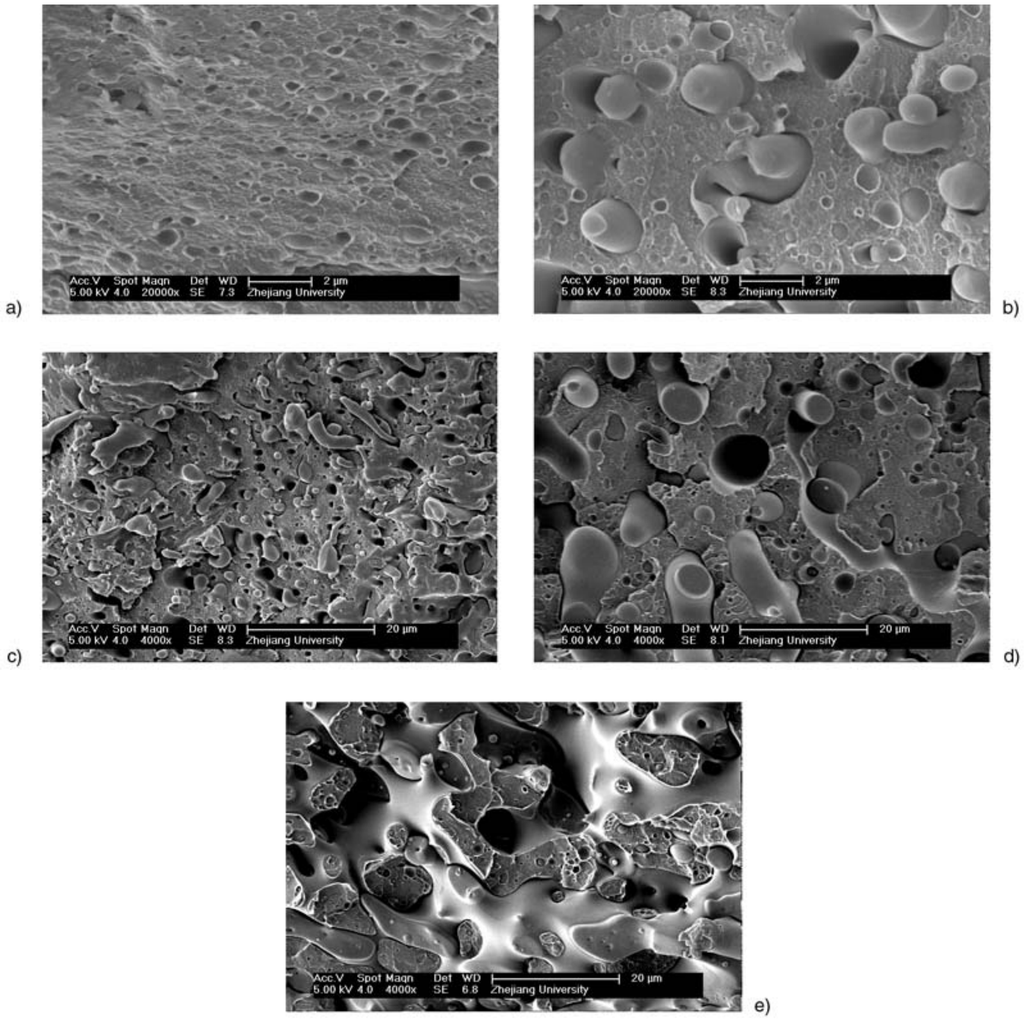

Figure 5. SEM micrographs of PS/POE blends: a) PS/POE = 90/10; b) and c) PS/POE = 80/20; d) PS/POE = 70/30; and e) PS/POE = 60/40

It can be seen for all blend compositions (Figure 5a–5d) that the phase structure of these blends is inhomogeneous and that the blend composition influences the extent of dispersion of the two phases. Figure 5a showed a micrograph of the surface of the 90/10 PS/POE blend. In this blend, PS forms a continuous phase, while the POE forms a discrete phase, indicating immiscible behavior of the blends. The POE phase presents droplets with different sizes in the blend and poor adhesion between phases can be observed. Figure 5b and 5c depicts the morphology of 80/20 PS/POE blend. It can be seen that the POE phases change partially continuous long fibrils and the POE domain size becomes bigger. The micrograph revealed a change in the distribution of the dispersed POE particles, with many of them starting to form aggregate-like elongated structures. According to the differences of the structure and shape between Figure 5a, 5b and 5c, therefore, when POE content is about 20 wt%, the volume fraction of stress volumes has already exceeded the percolation threshold, and the stress volume has overlapped. With the composition of PS/POE increasing to 70/30 (Figure 5d), the aggregates were more obvious and the fiber diameters were coarser. The percolation phenomenon went on in the blends. However, when POE content increased to 40%, POE phase became completely continuous and PS/POE blends showed the co-continuous structures, as shown in Figure 5e.

3.4. The continuity of POE

POE can be well dissolved in *n*-heptane and PS is not dissolved in *n*-heptane. Therefore, the continuous POE phase in PS/POE blends can be extracted by *n*-heptane and we can calculate the continuity of POE from Equation 3. Figure 6 presents the evolution of the continuity of POE with the composition of the PS/POE blends. At 90/10 PS/POE the level

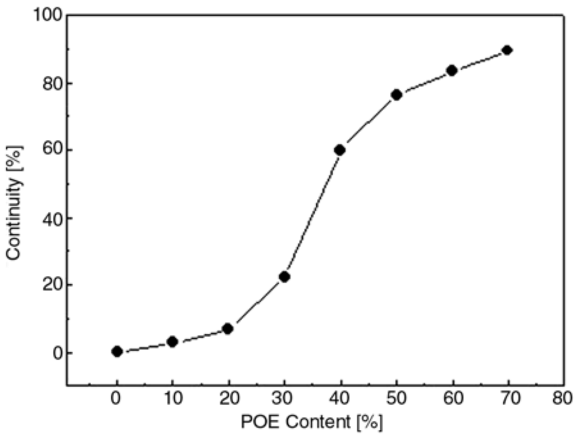

Figure 6. Continuity of POE phase as a function of the composition after solvent dissolution

of continuity of POE is nearly zero, consisting with the typical matrix-droplet structure in morphology as shown in Figure 5a. As the content of POE increasing, the continuity is also increasing, reflecting in morphology (Figure 5c and 5d) as the POE particles elongating. When the content of POE is about 40%, the continuity has been beyond 50%, corresponding to the co-continuous morphology structure in Figure 5e. The content of 20% POE seems a threshold of continuity increasing dramatically, indicating that the percolation phenomenon has already started. This result gives the additional evidence to the morphology observation for the gradual coarsening of fiber diameters up to the phase inversion region.

4. Conclusions

The percolation model has been applied to the study on brittle to ductile transition (BDT) of the PS/POE blends. According to the interparticle distance theory and percolation model, the relations of stress volume (V_s), volume fraction (V_r) and S/d were achieved. It was predicted that the percolation threshold (V_{sc}) varied from $\pi/6$ to 0.65. The curve of Charpy impact strength and content of POE showed a typical brittle to ductile transition phenomenon. The 14 wt% POE content was a critical point at which the BDT in PS/POE blends was induced and the percolation threshold of PS/POE blends was showed within 0.53 ~ 0.64, corresponding to the theoretical value. It was well shown the percolation point and phase inversion through morphology observations of SEM and TEM and continuity of POE by selective dissolution.

References

[1] Vincent P. I.: The tough-brittle transition in thermoplastics. Polymer, **1**, 425–444 (1960).
[2] Beardmore P.: Temperature dependence of yield and fracture in polymethylmethacrylate. Philosophical Magazine Letters, **19**, 389–394 (1969).
[3] Jang B. Z., Uhlmann D. R., Vander Sande J. B.: Ductile-brittle transition in polymers. Journal of Applied Polymer Science, **29**, 3409–3420 (1984).
[4] Vu-Khanh T., Yu Z.: Mechanisms of brittle-ductile transition in toughened thermoplastics. Theoretical and Applied Fracture Mechanics, **26**, 177–183 (1997).
[5] Gaymans R. J., Hamberg M. J. J., Inberg J. P. F.: The brittle-ductile transition temperature of polycarbonate as a function of test speed. Polymer Engineering and Science, **40**, 256–262 (2000).
[6] Chang F. C., Wu J. S., Chu L. H.: Fracture and impact properties of polycarbonates and MBS elastomer-modified polycarbonates. Journal of Applied Polymer Science, **44**, 491–504 (1992).
[7] Matsushige K., Radcliffe S. V., Baer E.: The pressure and temperature effects on brittle-to-ductile transition in PS and PMMA. Journal of Applied Polymer Science, **20**, 1853–1866 (1976).
[8] Yin J. H., Mo Z. S.: Medern polymer physics. Science Publishing Company, Beijing (2001).
[9] Wu S.: Phase structure and adhesion in polymer blends: A criterion for rubber toughening. Polymer, **26**, 1855–1863 (1985).
[10] Wu S., Margolina A.: Percolation model for brittle tough transition in nylon rubber blends – Replay to comments. Polymer, **31**, 972–974 (1990).
[11] Wu S.: A generalized criterion for rubber toughening: The critical matrix ligament thickness. Journal of Applied Polymer Science, **35**, 549–561 (1988).
[12] Wu S.: Chain structure, phase morphology, and toughness relationships in polymers and blends. Polymer Engineering and Science, **30**, 753–761 (1990).
[13] Borggreve R. J. M., Gaymans R. J., Schuijer J., Housz J. F. I.: Brittle-tough transition in nylon-rubber blends: effect of rubber concentration and particle size. Polymer, **28**, 1489–1496 (1987).
[14] Gaymans R. J., Borggreve R. J. M., Spoelstra A. B.: Ductile transition in nylon-rubber blends: Influence of water. Journal of Applied Polymer Science, **37**, 479–486 (1989).
[15] Borggreve R. J. M., Gaymans R. J.: Impact behaviour of nylon-rubber blends: 4. Effect of the coupling agent, maleic anhydride. Polymer, **30**, 63–70 (1989).
[16] Borggreve R. J. M., Gaymans R. J., Schuijer J.: Impact behaviour of nylon-rubber blends: 5. Influence of the mechanical properties of the elastomer. Polymer, **30**, 71–77 (1989).
[17] Sjoerdsma S. D., Heikens D.: The effect of varying the polyethylene content and the co-polymer content on crazing in polystyrene/low-density-polyethylene blends. Journal of Materials Science, **17**, 2605–2612 (1982).

[18] Jiang W., Tjiong S. C., Li R. K. Y.: Brittle-tough transition in PP/EPDM blends: effects of interparticle distance and tensile deformation speed. Polymer, **41**, 3479–3482 (2000).

[19] Jiang W., Liu C. H., Wang Z. G., An L. J., Liang H. J., Jiang B. Z., Wang X. H., Zhang H. X.: Brittle-tough transition in PP/EPDM blends: effects of interparticle distance and temperature. Polymer, **39**, 3285–3288 (1998).

[20] Yang J. H., Zhang Y., Zhang Y. X.: Brittle-tough transition of PP/POE blends in both impact and high speed tensile tests. Polymer, **44**, 5047–5052 (2003).

[21] Margolina A., Wu S. H.: Percolation model for brittle-tough transition in nylon/rubber blends. Polymer, **29**, 2170–2173 (1988).

[22] Saleem M., Baker W. E.: In situ reactive compatibilization in polymer blends: Effects of functional group concentrations. Journal of Applied Polymer Science, **39**, 655–678 (1990).

[23] Eklind H., Maurer F. H. J.: The effect of interfacial interactions on the rheo-optical behaviour of compatibilized PS/LDPE/SEBS copolymer blends. Polymer, **37**, 4465–4471 (1996).

[24] Li J. X., Chan C. M., Gao B. H., Wu J. S.: Effects of Thermal History on the Interfacial Layer of PS/HDPE/SBS Blends. Macromolecules, **33**, 1022–1029 (2000).

[25] Xu S. A., Tjong S. C.: Deformation mechanisms and fracture toughness of polystyrene/high-density polyethylene blends compatibilized by triblock copolymer. Journal of Applied Polymer Science, **77**, 2024–2033 (2000).

[26] Kim W. N., Burns C. M.: Thermal behavior, morphology, and the determination of the Flory-Huggins interaction parameter of polycarbonate-polystyrene blends. Journal of Applied Polymer Science, **34**, 945–967 (1987).

[27] Cho K., Ahn T. O., Ryu H. S., Seo K. H.: Mechanical effects according to the type of poly(styrene-co-methyl methacrylate) copolymers at polystyrene/poly(methyl methacrylate) interfaces. Polymer, **37**, 4849–4852 (1996).

[28] Li H. P., Li Z. M.: Investigation of phase morphology, thermal behavior, and impact properties of polyamide-1010/polystyrene blends compatibilized by lightly sulfonated polystyrene ionomers. Journal of Applied Polymer Science, **67**, 61–69 (1998).

[29] Park C. D., Jo W. H., Lee M. S.: Effect of molecular weight of functionalized polystyrene on the compatibility of blends of polyamide 6 and polystyrene. Polymer, **37**, 3055–3063 (1996).

[30] Wu J. S., Guo B. H., Chan C. M., Li J. X. Tang H. S.: Synergistic toughening effect of SBS and HDPE on the fracture of the PS/HDPE/SBS blends. Polymer, **42**, 8857–8865 (2001).

[31] Fang Z. P., Xu C. W., Xiang Y. C., Wu J. H., Xu H. C.: Crosslinking and compatibilization in blends of polystyrene and polyethylene. Chinese Journal of Polymer Science, **16**, 207–218 (1998).

[32] Fang Z. P., Guo Z. H., Zha L. L.: Toughening of Polystyrenewith Ethylene-Propylene-Diene Terpolymer (EPDM) Compatibilized by styrene-Butadiene-Styrene Block Copolymer (SBS). Macromolecular Materials and Engineering, **289**, 743–748 (2004).

[33] Guo Z. H., Tong L. F., Fang Z. P.: In Situ Compatibilization of Polystyrene/Polyolefin Elastomer Blends by Friedel-Crafts alkylation reaction. Polymer International, **54,** 1647–1652 (2005).

[34] Jaziri M., Kallel T. K., Mbarek S., Elleuch B.: Morphology development in polyethylene/polystyrene blends: the influence of processing conditions and interfacial modification. Polymer International, **54**, 1384–1391 (2005).

[35] Williams J. G.: Fracture mechanics of polymers. Ellis Horwood Ltd, Chichester (1984).

[36] Zheng Q., Feng J. M., Peng M.: Percolation phenomenon in SAN toughened by core-shell polymer MBS. Journal of Materials Science Letters, **19**, 623–625 (2000).

eXPRESS Polymer Letters Vol.1, No.1 (2007) 44–50
Available online at www.expresspolymlett.com
DOI: 10.3144/expresspolymlett.2007.9

Miscibility and specific interactions in blends of poly[(styrene)-co-(cinnamic acid)] with poly(methyl methacrylate) and modified poly(methyl methacrylate)

N. Bouslah[*], *F. Amrani*

Faculty of Sciences, University of Sciences and Technology Houari Boumediene, B.P. 32, El Alia, Algiers, 16111, Algeria

Received 21 November 2006; accepted in revised form 30 December 2006

Abstract: The miscibility behavior of poly(styrene-co-cinnamic acid) (PSCA) with poly(methyl methacrylate) (PMMA), poly[(methyl methacrylate)-co-(4-vinylpyridine)] (PMMA4VP) and poly[(methyl methacrylate)-co-(2-vinylpyridine)] (PMMA2VP) was studied. DSC measurements indicated that PSCA23 containing 23 mol% of carboxylic acid units was miscible with PMMA, PMMA2VP and PMMA4VP as established from the observation of a single composition dependent glass transition temperature. Miscibility was induced via hydrogen bonding as evidenced by IR frequency shifts of the hydroxyl stretching vibrations of the acid copolymer in the blends. Interpolymer hydrogen bonding formation within the binary systems was also investigated by viscosimetric study of dilute solutions in toluene. For PMMA/PSCA5 blends the viscosity of the mixtures was close to the weight average viscosities of the individual polymer while for blend solutions of PSCA5 with PMMA2VP and PMMA4VP, the interactions were sufficiently strong to form interpolymer complexes with a decrease in viscosity in comparison to the additivity rule.

Keywords: *polymer blends and alloys, miscibility, DSC, FTIR, viscosimetry*

1. Introduction

Polymer blending[1–3] is a fast and common way to develop new polymeric materials with a desirable combination of properties. The main advantage of this method is simplicity of preparation and control of the properties by varying the blend compositions. Miscibility plays a decisive role in controlling the properties of the final product and generally requires the presence of intermolecular interactions. Specific interactions most often generate a negative heat of mixing and contribute favorably to the free energy of mixing. Among all the interactions examined in the literature, hydrogen bonding[4–6]seems very attractive since it quite efficiently improved the miscibility.

In this work, we first report on the compatibilization of an immiscible[7] polymer pair, polystyrene (PS) and poly(methyl methacrylate) (PMMA), by incorporating cinnamic acid (CA) groups into the PS chains capable of participating in specific interactions with unmodified PMMA. In a second time, we examine the miscibility and specific interactions in blends of poly(styrene-co-cinnamic acid) PSCA with PMMA modified by basic comonomers. 4-vinylpyridine (4VP) and 2-vinylpyridine (2VP) groups were chosen to be incorporated into the PMMA chains because there are known to be stronger hydrogen bond acceptors than the ester carbonyl of PMMA. We have introduced approximately the same number of 4VP and 2VP units into PMMA chains for comparative purpose.

---

[*] Corresponding author, e-mail: bouslah_naima@yahoo.fr

The DSC study has been used to investigate the miscibility of the polymer blends using the single composition dependent glass transition criterion. Specific interactions between the blend components have been investigated by Fourier transform infrared spectroscopy and compared to the calorimetric results. Viscosimetric technique based on the study of interactions in dilute solutions of the polymer blends has also been used as a complementary technique to prospect the effect of the position of the nitrogen atom in the pyridine ring on the interactions developed within PMM4VP/PSCA5 and PMM2VP/PSCA5 blends. The variation of the reduced viscosity of dilute polymer blend solutions with blend composition has been used as a criterion[8–9] of hydrogen bonding interaction formation.

2. Experimental section

2.1. Polymer synthesis and Characterizations

MMA, 2VP and 4VP monomers were distilled under reduced pressure before use. PMMA, PMMA4VP and PMMA2VP copolymers were synthesized in solution by free radical copolymerization using 2,2'-azobisisobutyronitrile (AIBN) as initiator at 60°C, under N_2 blanket. The conversions were kept less than 15% to prevent composition drift. The polymers were purified by repeated dissolution/precipitation in THF/methanol, isolated by filtration, vacuum dried at room temperature and then at 40°C for several days. The synthesis of poly(styrene-co-cinnamic acid) (PSCA) copolymers containing 5, 10, 15 and 23 mol% of cinnamic acid (CA) content has been described previously[10]. Weight-average molecular weight M_w were determined from THF solutions by size exclusion chromatography using polystyrene or poly(methyl methacrylate) standards with a Waters GPCII. The acid content in the PSCA copolymers was determined by titration of the corresponding polymer solution in benzene-methanol (20 vol% methanol) with a standardized sodium hydroxide solution. The 4VP and 2VP chromophore contents in the PMMA4VP and PMMA2VP copolymers respectively were determined by UV spectroscopy. The main molecular characteristics of the polymers are listed in Table 1.

2.2. DSC measurements

Binary blends of different weight ratios were prepared in the desired composition by dissolving the appropriate amounts of each polymer in THF, at room temperature. The resulting solution was stirred for one day to ensure thorough mixing, followed by precipitation into a large excess of petroleum ether. The resulting blend was isolated by filtration and repeatedely washed with several portions of non-solvent. The powder samples were then vacuum dried at 50°C for several days. Thermal analysis was conducted on a Perkin-Elmer DSC-7 differential scanning calorimeter previously calibrated with indium. Small quantities of the samples, 10–15 mg, were scanned at a heating rate of $20\ \mathrm{K{\cdot}min^{-1}}$ under N_2. The T_g was recorded as the temperature corresponding to the midpoint of the heat capacity change at the second thermal scan. All samples were preheated to 200°C and kept for 10 mn at that temperature to ensure complete removal of any trace of residual solvent.

2.3. FTIR measurements

Infrared spectroscopic measurements were recorded on a Nicolet 560 Fourier tansform infrared spectrometer at a resolution of $2\ \mathrm{cm^{-1}}$ and were averaged from 64 scans at minimum.

The polymer blends were prepared in different weight ratios by codissolution of required amounts of the components in a common solvent at a concentration of $1.2\ \mathrm{g{\cdot}dl^{-1}}$. The resulting solutions were stirred for 1 day to ensure thorough mixing and then casted onto potassium bromide discs. The samples were first dried at room temperature to reduce the evaporation rate and to avoid film cracking and then placed in a vacuum oven at 60°C for several days.

2.4.Viscosity measurements

Viscosity measurements were carried out using an AVS360 automatic Ubbelohde-type capillary viscosimeter from Schott Geräte. Intrinsic viscosities of the different copolymers listed in Table 1, were determined at 25°C in butanone by extrapolation to zero concentration of the plot of the reduced viscosity versus concentration.

Table 1. Main characteristics of the copolymers

Polymer	Composition [mol%]	η [dl·g⁻¹.]	M_w	T_g [°C]
PMMA	–	0.59	376 146	117
PMMA4VP15	14.56	0.52	216 652	125
PMMA2VP16	16.48	0.77	231 000	121
PSCA5	4.70	0.37	163 300	116
PSCA10	9.97	0.34	–	132
PSCA15	14.70	0.29	–	141
PSCA23	23.20	0.26	115 300	174

3. Results and discussion

3.1. Calorimetric analysis

All PMMA-PSCA23, PMMA2VP-PSCA23 and PMMA4VP-PSCA23 blends exhibited a single T_g, intermediate between that of the parent polymers, indicating the miscibility of these systems. T_{gs} of PSCA copolymers with CA content lower than 23 mol% are too close to those of PMMA, PMMA 2VP and PMMA4VP to investigate the miscibility of their blends by convenionnel DSC. As illustrated in Figure 1, the T_g-composition curve was S-shaped for PMMA-PSCA23 system. The strength of the interactions involved in such a case is considered being less important than in PMMA2VP/PSCA23 and PMMA4VP/PSCA23 systems presenting positive deviations from the calculated weight average T_g values. Indeed, it is well established that when interactions between blend components are strong, such as those affected by Hydrogen bonding, the experimentally determined T_g of the blends are higher than those calculated from the additivity rule as a result of the reduction of polymer chains mobility in the blend.

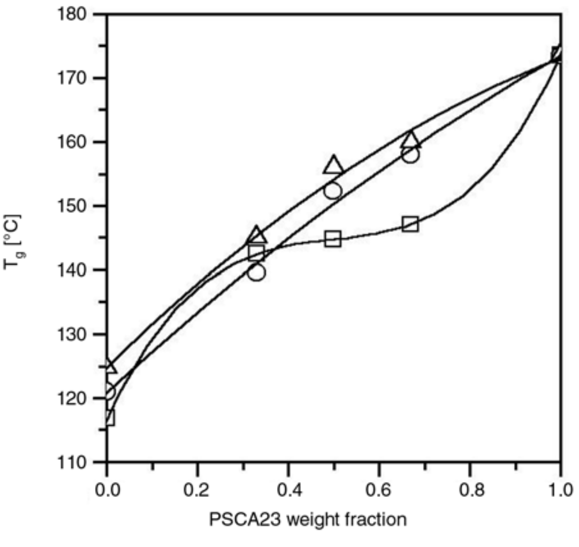

Figure 1. T_g-composition curves of blends of PSCA23 with (□)PMMA, (O)PMMA2VP and (Δ)PMMA4VP

In order to estimate the strength of the intermolecular interactions developed within the PMMA2VP/PSCA23 and PMMA4VP/PSCA23 systems we used the Kwei [11] equation where the quadratic term qW_1W_2 provides an indication on the number and the strength of specific interactions within the blend:

$$T_{g(\text{blend})} = \frac{W_1T_{g1} + KW_2T_{g2}}{W_1 + KW_2} + qW_1W_2 \quad (1)$$

Where W_1 , W_2 and T_{g1}, Tg_2 are the weight fractions and the glass transition temperatures of pure components 1 and 2 respectively. K and q are fitting constants. To fit T_g data to the Kwei equation with only one adjustable parameter, it is useful to set K equal to unity. The Kwei equation can be written in a reduced version as:

$$T_g = W_1T_{g1} + W_2T_{g2} + qW_1W_2 \quad (2)$$

The best fitted curves of the Kwei equation for the experimental data are obtained for q values of 10 and 21 for PMMA2VP/PSCA23 and PMMA4VP/PSCA23 systems respectively. The higher q value obtained for PMMA4VP/PSCA23 suggests that the interpolymer interaction in this system is somewhat stronger than that in the PMMA2VP/PSCA23. This is probably due to the fact that the former suffers less steric effect than the latter since the nitrogen atom of the 2VP is too close to the backbone which limits the formation of hydrogen bonding between the acid hydrogen of PSCA23 and the nitrogen atom of the 2VP units in the PMMA2VP.

3.2. FTIR study

The assignments of various infrared bands in styrene copolymers containing carboxylic acid groups have been published [12–13]. The dimeric form presents as found in the literature in the hydroxyl region a characteristic infrared broad band at about 3000 cm^{-1} and a satellite one which generally appears at 2650 cm^{-1}. The corresponding carbonyl groups are usually seen at 1700 cm^{-1}. Infrared band attributed to unassociated carboxylic acid groups has been detected at 1742 cm^{-1}. Free hydroxyl groups are difficult to observe in the hydroxyl region and may appear as a weak shoulder at about 3520 cm^{-1}. In the first part of the FTIR study, we focus our attention on the PSCA copolymers. In the carbonyl region, Figure 2, the PSCA copolymer spectra are dominated by the characteristic band of self association attributed to the intermolecular carboxylic acid dimer at 1703 cm^{-1}. The band at 1743 cm^{-1} is assigned to C=O stretching for the cinnamic acid units where the carbonyl groups are not hydrogen bonded. As can be seen, the relative magnitude of the non-hydrogen bonded or free carbonyl groups at 1743 cm^{-1} increases with a decrease of the CA content in the PSCA copolymer, indicating that the self association in the copolymer increases when the CA copolymer composition is raised progressively from 5 to 23 mol%. Figure 3 shows FTIR spectra of pure PSCA15 and the PMMA/PSCA15 blends in the hydroxyl region. As can be seen, a broad band that extends over the 3400–2700 cm^{-1} range with a maximum at about 3000 cm^{-1} occurring beneath the CH stretching modes is assigned to self-associated hydrogen bonded acid groups in cyclic structures or dimeric form. The other characteristic band of self association is the broad band at about 2675 cm^{-1}, a satellite band, enhanced by Fermi resonance. Moreover, a weak band observed at 3442 cm^{-1} is attributed to carboxylic acid units that are intermolecularly hydrogen bonded to the π system of the phenyl groups in the PSCA copolymers. This band has already been observed by Paul [13] in the case of styrene/acrylic acid copolymers and Coleman [14] in the case of (styrene-co-methacrylic acid) copolymers. For illustrative purpose, the different hydroxyl bands of the PSCA spectrum illustrated in the same figure are obtained by performing a deconvolution procedure on the difference spectrum [(PSCA15)–(PS)] in order to eliminate the C–H bands. In the PMMA/PSCA15 blends, Figure 3, the broad band at about 3000 cm^{-1} corresponding to the dimeric hydroxyl groups decreases in intensity as compared to the pure PSCA15 spectrum indicating the dissociation of some of the dimeric groups. Furthermore, a new band at about 3295 cm^{-1}, can clearly be seen, and may be readely attributed to the stretching vibration of hydroxyl groups of PSCA15 copolymer hydrogen bonded to the PMMA carbonyl groups. It is then assigned to the ester-acid interaction. As illustrated in Figure 4, a little increase of the band corresponding to this interaction can also be detected for PMMA–PSCA23 blend in the 50/50 weight ratio and is

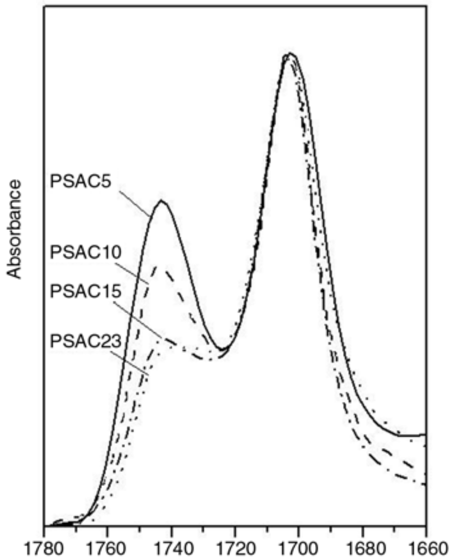

Figure 2. FTIR spectra of the PSCA copolymers in the carbonyl region

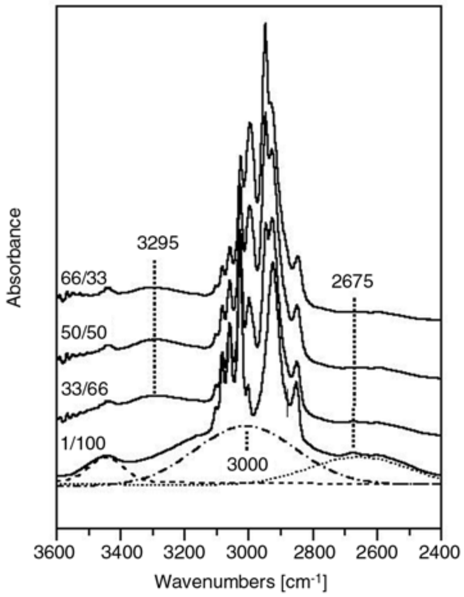

Figure 3. FTIR spectra of the PMMA/PSCA15 system in the hydroxyl region(blend composition indicated)

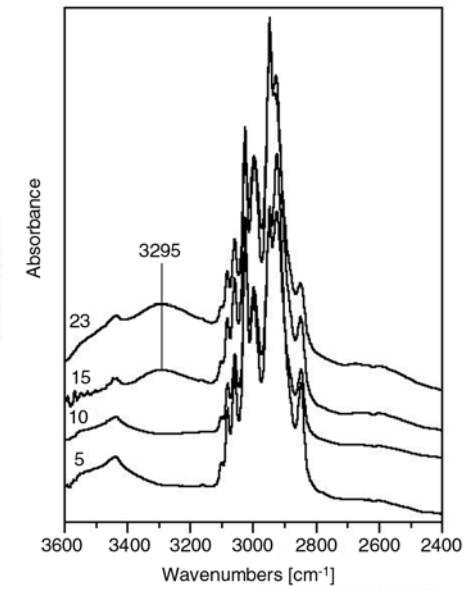

Figure 4. FTIR spectra of 50/50 weight ratio PMMA/PSCA blends with different compositions of CA content in the PSCA copolymer

related to the expected increase in the proportion of hydrogen bonds in the blend with CA content in the acid copolymer. However as the composition of acid groups in the PSCA copolymer is reduced from 15 to 10 and then to 5 mol% of CA content in the PSCA copolymer, no intermolecular hydrogen bonds between the two blend components is noticeable since this band disappears totally in the PMMA/PSCA10 and PMMA/PSCA5 blends. At these compositions, there is not a sufficient proportion of acid groups to allow formation of a measurable amount of interassociated hydrogen bonds between PMMA and PSCA copolymers.

The band at 3295 cm^{-1} has also been been observed for both PMMA4VP/PSCA and PMMA2VP/PSCA systems when the CA content in the PSCA copolymer was 15 or 23 mol% indicating the development of the ester-acid interactions in these blends.

Furthermore, the satellite band at about 2675 cm^{-1} in the pure PSCA15 spectrum, Figure 5., shifts slightly to the low frequency side in the PMMA4VP/PSCA15 and PMMA2VP/PSCA15 blends. This displacement reflects a redistribution of a part of the self-associated acid groups to heteroassociated ones in the blends. We may therefore assign this shift to the pyridine-acid interaction between the hydroxyl groups of PSCA copolymer and the nitogen atom of the 4VP or 2VP in the PMMA4VP or PMMA2VP copolymers respectively. One must note that this little displacement ($\Delta\nu$ = 60 cm^{-1}) is consistent with the moderate q values revealed by the DSC study.

3.3. Viscosimetry study

Because of its simplicity, the viscosimetric technique has been extensively used to investigate polymer-polymer interactions in solution. It is well known that the solvent selected for the study has a great influence on the polymer-polymer interactions in solution since the formation of hydrogen bonding in polymer blend solutions is governed by the interaction between the proton donating and

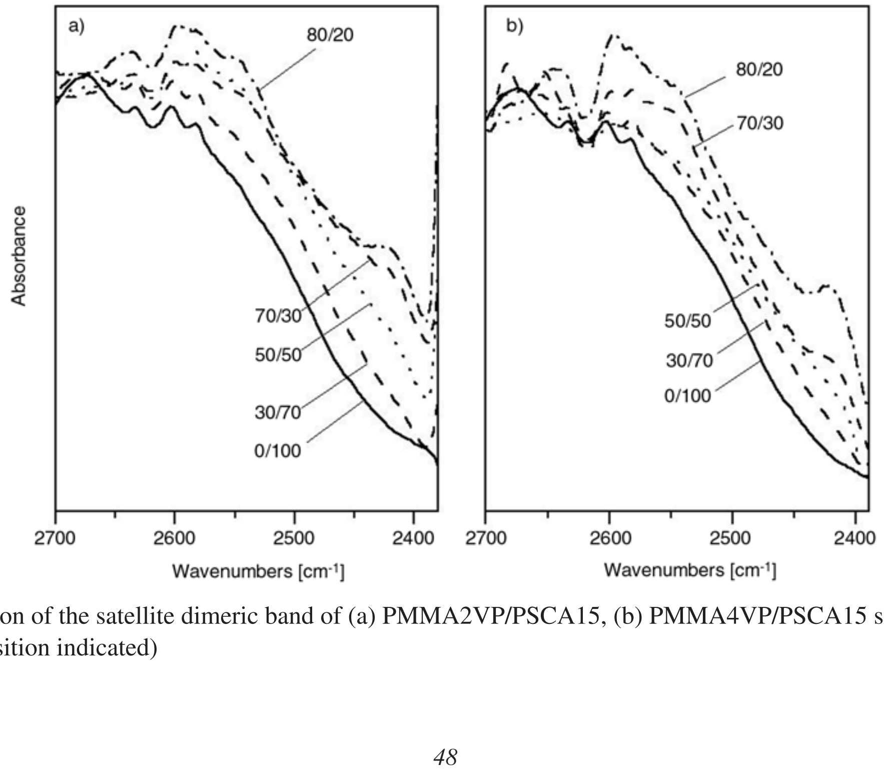

Figure 5. Evolution of the satellite dimeric band of (a) PMMA2VP/PSCA15, (b) PMMA4VP/PSCA15 systems(blend composition indicated)

proton accepting polymers and that between the polymers and the solvent. In this study, we used toluene which is inert to hyrogen bonding and then may have small affect on the formation of the ester/acid interaction and/or the pyridine-acid one. However toluene was not able to dissolve PSCA copolymers with CA content higher than 5 mol%. Prior to the study of the polymer blend solutions, it was necessary to characterize the polymer blend components. The plot of the reduced viscosity of the polymer solutions were fitted through the Huggins equation and the values of the intrinsic viscosities [η] were determined by linear regression analysis of the reduced viscosity *versus c*.

Measurements of the reduced viscosities η_{sp}/c of blend solutions were conducted as a function of blend composition with the original total concentration of 0.15 $g\cdot dl^{-1}$. This concentration value corresponds to a much lower concentration than the critical concentration C^* estimated by $C^* = 1/[\eta]$. Indeed, in absence of specific interactions within the blend, polymer coils are independent if the solution concentration is below the critical concentration. On the other hand, when the interpolymer interactions are sufficiently strong, we can observe polymer-polymer complexation which result in viscosity decrease, turbidity or even precipitation [15]. The mixed solutions in toluene of PMMA and PSCA5 were clear indicating that no strong interactions are taking place between the blend components chains. In contrast, turbid solutions were obtained for PMMA4VP/PSCA5 and PMMA2VP/PSCA5 blends. This behaviour indicates the formation of strong interpolymer interactions in solution. In this case, the viscosities were measured after filtrating the polymer blend solutions so the measured viscosities have apparent values. In Figure 6, the reduced viscosities of PMMA/PSCA5 blend solutions follow the additivity law indicating that CA content in the PSCA5 copolymer is too low to develop interactions with PMMA as suggested by the FTIR study. However, the introduction of the 4VP or 2VP units in the PMMA chains leads to negative deviations indicating that hydrogen bonding accompanies contraction of the components polymer coils in the PMMA2VP/PSCA5 and PMMA4VP/PSCA5 systems. Furthermore, the deviation observed for the PMMA4VP/PSCA5 is more important confirming that the 4VP-acid interaction is stronger than the 2VP-acid as demonstrated with the calorimetric results.

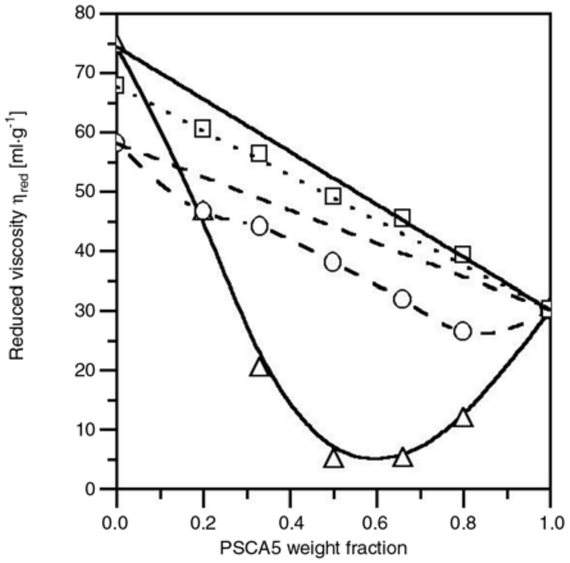

Figure 6. Reduced viscosity versus blend composition of PSCA5 with (□)PMMA, (O)PMMA2VP and (Δ)PMMA4VP

4. Conclusions

The enhancement of poly(methyl methacrylate)/polystyrene miscibility has been achieved by introducing cinnamic acid units along the polystyrene chains. The introduction of the 4VP or 2VP groups into the PMMA chains results in an increase of the interpolymer specific interactions between the PS and the PMMA as revealed by the DSC study. The FTIR spectra showed that PMMA4VP and PMMA2VP interact with PSCA through their carbonyl and pyridine units. The viscosimetric results are in good agreement with the DSC measurements which revealed that PSCA copolymer develop stronger interactions with PMMA4VP than PMMA2VP and PMMA polymers.

Acknowledgments

N. Bouslah gratefully acknowledges Pr. S Djadoun for his helpful discussion and comments.

References

[1] He Y., Zhu B., Inoue Y.: Hydrogen bond in polymer blends. Progress in Polymer Science, **29**, 1021–1051 (2004).

[2] Wang J., Cheung M. K., Mi Y.: Miscibility and Morphology in crystalline/amorphous blends of poly(caprolactone)/poly(4-vinylphenol) as studied by DSC, FTIR and 13C solid state NMR. Polymer, **43**, 1357–1364 (2002).

[3] Huang H. L., Goh S. H., Wee A. T. S.: Miscibility and interactions in poly(2,2,3,3,3-pentafluoropropyl methacrylate-co-4-vinylpyridine)/poly(p-vinylphenol) blends. Polymer, **43**, 2861–2867 (2002).

[4] Coleman M. M., Graf J. F., Painter P. C.: Specific interactions and the miscibility of polymer blends. Technomic, Lancaster PA (1991).

[5] Luo X. F., Hu X., Zhao X. Y., Goh S. H., Li X. D.: Miscibility and interactions in blends and complexes of poly(4-methyl-5-vinylthiazole) with proton donating polymers. Polymer, **44**, 5285–5291 (2003).

[6] Kuo S. W., Chen S. C., Chang F. C.: Miscibility enhancement on the immiscible binary blends of poly(vinyl acetate) and poly(vinyl pyrrolidone) with bisphenol A. Polymer, **43**, 3653–3660 (2002).

[7] Fekete E., Foldes E., Pukanszky B.: Effect of molecular interactions on the miscibility and structure of polymer blends. European Polymer Journal, **41**, 727–736 (2005).

[8] Zhang G., Jiang M., Zhu L., Wu C.: Intermacromolecular complexation because of specific interactions 11. Ionic interaction complexation and its comparison with hydrogen bonding complexation. Polymer, **42**, 151–159 (2001).

[9] Liu S., Pan Q., Xie J., Jiang M.: Intermacromolecular complexes due to specific interactions. 12. Graft-like hydrogen bonding complexes based on pyridyl-containing polymers and end-functionalized polystyrene oligomers. Polymer, **41**, 6919–6929 (2000).

[10] Bouslah N., Hammachin R., Amrani F.: Study of the compatibility of poly[styrene-co-(cinnamic acid)]/poly[(ethyl methacrylate)-co-(2-dimethyl aminoethyl methacrylate)] blends. Macromolecular Chemistry and Physics, **200**, 678– 682 (1999).

[11] Lin A. A., Kwei T. K., Reiser A.: On the physical Meaning of the Kwei Equation for the glass transition temperature of polymer blends. Macromolecules, **22**, 4112–4119 (1989).

[12] Motzer H. R., Painter P. C., Coleman M. M.: Interactions in miscible blends of poly(styrene-co-methacrylic acid) with copolymers containing vinylpyrrolidone and vinylpyridine groups. Macromolecules, **34,** 8390–8393 (2001).

[13] Jo W. H., Cruz C. A., Paul D. R.: FTIR investigation of interactions in blends of PMMA with styrene/acrylic acid copolymer and their analogues. Journal of Polymer Science Part B-Polymer Physics, **27**, 1057–1076 (1989).

[14] Cleveland C. S., Fearnley S. F., Hu Y., Wagman M. E., Painter P. C., Coleman M. M.: Infrared characterization and determination of self-association equilibrium constants for methacrylic acid copolymers. Journal of Macromolecular Science-Physics, **B39**, 197–223 (2000).

[15] Xiang M., Jiang M., Zhang Y., Wu C., Feng L.: Intermacromolecular complexation due to specific interactions. 4. The hydrogen-bonding complex of Vinylphenol-containing copolymer and vinylpyridine-containing copolymer. Macromolecules, **30**, 2313–2319 (1997).

eXPRESS Polymer Letters Vol.1, No.1 (2007) 51–58
Available online at www.expresspolymlett.com
DOI: 10.3144/expresspolymlett.2007.10

Peroxydisulfate initiated synthesis of potato starch-graft-poly(acrylonitrile) under microwave irradiation

V. Singh[1*], *A. Tiwari*[2], *S. Pandey*[1], *S. K. Singh*[1]

[1]Department of Chemistry, University of Allahabad, Allahabad-211 002, India
[2]Division of Engineering Material, National Physical Laboratory, Dr. K. S. Krishnan Road, New Delhi-110 012, India

Received 21 October 2006; accepted in revised form 27 December 2006

Abstract. Potato starch-graft-poly(acrylonitrile) could be efficiently synthesized using small concentration of ammonium peroxydisulfate (0.0014 M) in aqueous medium under microwave irradiation. A representative microwave synthesized graft copolymer was characterized using Fourier Transform Infrared Spectroscopy, X-ray Diffraction, Scanning Electron Microscopy and Thermo gravimetric Analysis. Under microwave conditions oxygen removal from the reaction vessel was not required and the graft copolymer was obtained in high yield using very small amount of ammonium peroxydisulfate, however using the same amount of ammonium peroxydisulfate (0.0014 M) on thermostatic water bath no grafting was observed up to 98°C (even in inert atmosphere). Raising the concentration of the initiator to 0.24 M resulted into 10% grafting at 50°C but in inert atmosphere.

The viscosity/shear stability of the grafted starch (aqueous solution) and water/saline retention ability of the microwave synthesized graft copolymer were also studied and compared with that of the native potato starch.

Keywords: *polymer synthesis, biopolymer, starch, peroxydisulfate, microwave irradiation*

1. Introduction

Starch which is a low cost abundantly available renewable biopolymer on modification may develop properties comparable to synthetic petroleum-based polymers [1, 2] Chemical grafting [3–7] is one of the popular methods for modifying structure and properties of biopolymers. Vinyl grafting on to the polysaccharides improves their shelf life against biodegradation, thermal stability and metal ion binding ability and therefore grafted polysaccharides have a wide range of industrial utility [8]. Considerable amount of research has been published on ceric ion initiated graft copolymerization of acrylic monomers onto starch [9–11]. Potassium permanganate [12] has also been used as initiator to graft poly(acrylonitrile) on to starch. Most of the studies have been focused on grafting of acrylonitrile due to: (a) its superior grafting efficiency [13] and (b) production of the starch-based superabsorbent hydrogels [14] by alkaline hydrolysis of the starch-graft-poly(acrylonitrile). So far voluminous reports are available on the synthesis of starch-graft-poly(acrylonitrile) using redox initiators where inert atmospheric condition is the requirement since O_2 is a very potent inhibitor for most of the common vinyl monomers.

Microwave irradiation [15–19], as efficient thermal energy source constitutes a very original method of heating materials, different from the classical ones. Main advantage is that it results in almost instantaneous bulk heating of materials in a homogeneous and selective manner. Under microwave irradiation grafting and homopolymerization have been studied without initiators [3, 4] or in the presence of very low concentration of initiator [20, 21] and this prompted us to undertake microwave promoted

---

[*]Corresponding author, e-mail: singhvandanasingh@rediffmail.com

grafting of poly(acrylonitrile) onto potato starch using small concentration of ammonium peroxydisulfate as initiator.

2. Experimental Section

2.1. Materials and Instruments

A Kenstar (Model No. MOW 9811) domestic microwave oven with a microwave frequency of 2450 MHz and a power output from 0 to 1200 W with continuous adjustment was used for all the experiments. The starch sample (Qualigen, Extra pure) containing 30% amylose and 70% amylopectin was used without purification. Acrylonitrile (Lancaster, synthesis grade) was distilled in a stream of nitrogen before use. Ammonium peroxydisulfate (Merck) was used without further purification and double distilled water was used for the grafting reactions. Infrared (IR) spectra were recorded on a Nicolet 5700 of FTIR spectrophotometer using KBr pellet. X-Ray Diffraction (XRD) was carried out on Rigaku D/MAX-2200 X ray powder diffractometer. TGA was done on Perkin Elmer SII Dimond TGA/DTA at a heating rate of 10°C per min under nitrogen atmosphere. For the characterization, sample with maximum grafting was used. The viscosity measurements (of the aqueous solutions) were made on Brookfield LVDVE viscometer at 25°C using small sample adapter (spindle no S-18).

2.2. Acrylonitrile grafting on to starch under microwave irradiation

A calculated amount of the starch was dissolved in minimum required amount of warm distilled water in a 150 ml open necked flask. To this solution, calculated amount of the ammonium peroxydisulfate and acrylonitrile were added and the total volume was made up to 25 ml. The flask was exposed to fixed microwave power and exposure time. The graft copolymer was separated from poly(acrylonitrile) (PAN) by pouring the reaction mixture into 100 ml dimethylformamide (DMF) [3]. The copolymer was repeatedly washed with DMF to remove adhered PAN. The grafting experiment was also repeated in presence of hydroquinone (20 mg). The grafting ratio and grafting efficiency were calculated from the increase in weight in the following manner [8].

$$\text{Grafting ratio [\%G]} = \frac{W_1 - W_0}{W_0} \cdot 100 \tag{1}$$

$$\text{Grafting Efficiency [\%E]} = \frac{W_1 - W_0}{W_2} \cdot 100 \tag{2}$$

Where W_1, W_0, and W_2 denote, respectively, the weight of the starch-graft-poly(acrylonitrile) (S-g-PAN) the weight of original starch, and weight of the acrylonitrile used.

2.3. Graft co-polymerization of starch on thermostatic bath

Starch (0.1 g) was dissolved in 10 ml of hot distilled water in a two-necked flask. To this acrylonitrile (0.17 M) was added and the total volume was made up to 25 ml. The reaction mixture was purged with purified nitrogen for about 30 min and thermostated at 50°C. Ammonium peroxydisulfate (0.0014 M) was added to the reaction flask and this time was taken as zero time and the graft copolymerization was carried out for one hour. Reaction mixture was finally poured in to 100 ml of DMF [3] to precipitate the graft copolymer. The copolymer was repeatedly washed with DMF to remove the adhered PAN if any and dried. The above experiment was repeated at 98°C. Under identical conditions the reaction was also performed in presence of O_2 at both the temperatures. Grafting was also done with different persulfate concentration ranging from 0.0020–0.24 M at 50°C.

2.4. Hydrolysis of grafted starch in aqueous alkali

Starch-graft-poly(acrylonitrile) (2 g on dry basis) was dispersed in 2% NaOH at 100°C for 1.5 h. After hydrolysis [8] the sample was precipitated in 600 ml methanol, washed with methanol followed by ethanol, dried and weighed.

2.5. Water and saline (1% NaCl) retention

The sample (0.5 g on dry basis) was swollen in 100 ml distilled water for 30 minutes. The suspension was poured into a G-4 sintered glass filter at 93.32 kPa pressure. Water retention [8] was calculated as gram of water absorbed per gram of dry material. Similarly saline retention [8] capacity was determined using 1% aqueous sodium chloride solution.

2.6. Viscosity measurement

A weighed quantity of the samples were dissolved separately (Starch was dissolved in hot distilled water by stirring while the graft copolymer and saponified graft copolymer were dissolved in cold water by soaking them overnight) and then the resulting solutions were made up to desired concentrations and agitated vigorously for about 15 min till they became viscous and homogeneous. Viscosities of starch, starch-graft-poly(acrylonitrile) and saponified starch-graft-poly(acrylonitrile) were measured after different time intervals.

3. Results and discussion

Using low concentration of the ammonium peroxydisulfate, poly(acrylonitrile) could be very efficiently grafted on to the potato starch under microwave irradiation. Maximum grafting ratio and efficiency (225% and 98% respectively) were obtained at 0.17 M acrylonitrile, 0.0014 M $(NH_4)_2S_2O_8$, 0.1 g potato starch, 70 seconds exposure and 1200 W microwave power keeping total reaction volume fixed at 25 ml. The temperature of the reaction mixture just after the microwave exposure was measured to be 98°C. However at same concentrations of acrylonitrile (0.17 M) and starch (0.1 g/25 ml) on thermostatic water bath at 98°C, 0.0014 M peroxydisulfate was unable to trigger graft copolymerization (both in the nitrogen as well as in oxygen atmosphere) indicating that under conventional conditions, 0.0014 M peroxydisulfate is unable to furnish sufficient primary free radicals required for the graft copolymerization. However when the peroxydisulfate concentration was raised to 0.24 M (in conventional procedure), 10% grafting in nitrogen atmosphere was observed.

O_2 is a very potent inhibitor for most of the common vinyl monomers since it combines with active primary free radicals to give relatively inactive radicals, which are incapable of propagating the chain reaction. Thus the reaction media are usually thoroughly purged with inert gas to remove O_2, otherwise the reaction may not work, however under microwave conditions presence of O_2 does not effect the normal graft copolymerization reaction. It can be assumed that under the influence of microwaves the oxygen reversibly combines with the primary free radicals and thus is unable to inhibit the chain propagation; however more investigations are required on this issue.

3.1. Characterization of the grafted starch

A representative microwave synthesized graft copolymer sample (sample with maximum grafting ratio), was characterized using IR, XRD and TGA.

IR spectrum (Figure 1) of pure starch has a broad strong absorption at 3310–3425 cm^{-1} (O–H stretching) and a peak at 2947 cm^{-1} (C–H stretching) while IR spectrum of starch-graft-PAN has additional absorption peaks at 2242 cm^{-1} (–CN stretching) and 1453 cm^{-1} (CH_2 deformation vibration) which can be attributed to grafted PAN chains at starch backbone. Physical blends of gum and PAN after selective removal of PAN with DMF showed no absorption in –CN stretching and $-CH_2$ bending region. This substantiates the formation of the graft copolymer.

TGA of Starch (Figure 2) and starch-graft-PAN showed that grafted starch to be more thermally stable than the pure Starch. Up to 650°C, 49% loss in total weight was observed for grafted starch in comparison to 58% weight loss in starch.

Comparison of XRD of the starch, poly(acrylonitrile) (PAN) and starch-graft-PAN further confirms grafting (Figure 3). XRD spectra of the grafted starch showed increased crystallinity in the region of 2θ 28–32° due to the presence of PAN grafts on starch backbone, while peak at 2θ 18° originally present in the starch has been significantly reduced after grafting.

Grafting is also evidenced by the SEM picture of the starch, picture clearly shows change in the surface topology of the starch after grafting due to the growing poly(acrylonitrile) grafts (Figure 4).

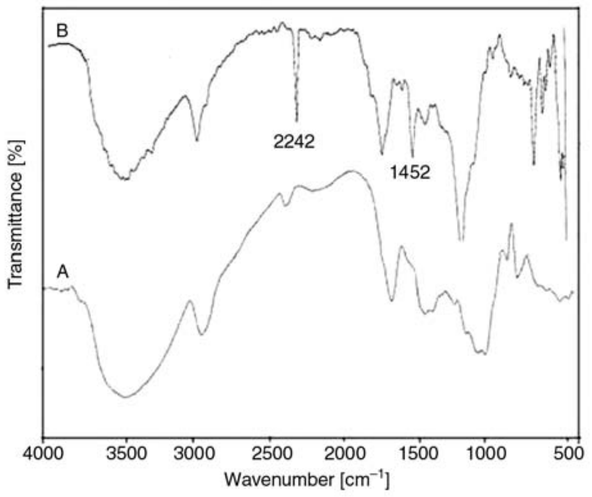

Figure 1. IR spectra of starch (A) and starch-graft-poly(acrylonitrile)

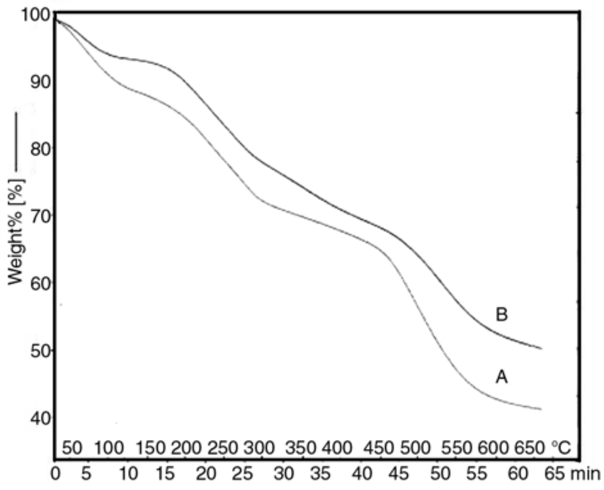

Figure 2. TGA of starch (A) and starch-graft-poly(acrylonitrile) (B)

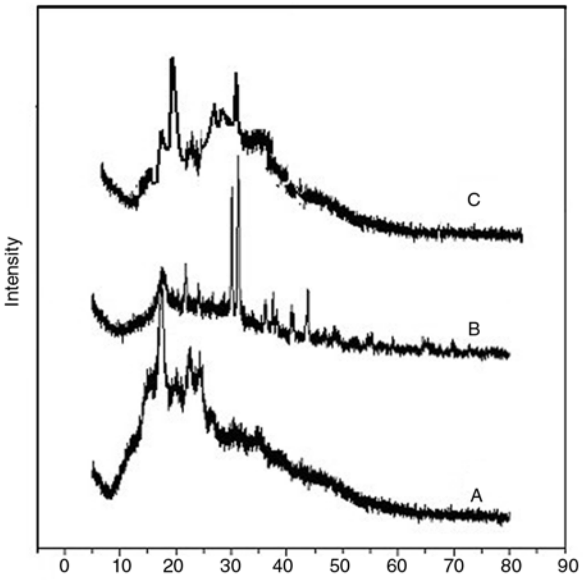

Figure 3. XRD of starch (A), starch-graft-poly(acrylonitrile) (B) and poly(acrylonitrile)

3.2. Mechanism of grafting

Since the grafting was not observed when the radical scavenger hydroquinone was added to the reaction mixture, a free radical mechanism for the grafting is the most probable and is proposed as under.

The grafting is being carried out in aqueous medium and the water being polar, absorbs microwave energy. This results in dielectric heating of the reaction medium. Microwaves are also reported to have the special effect [15] of lowering of Gibbs energy of activation of the reactions. These two effects cause quick decomposition of peroxydisulfate into sulphate ion radicals (Figure 5).

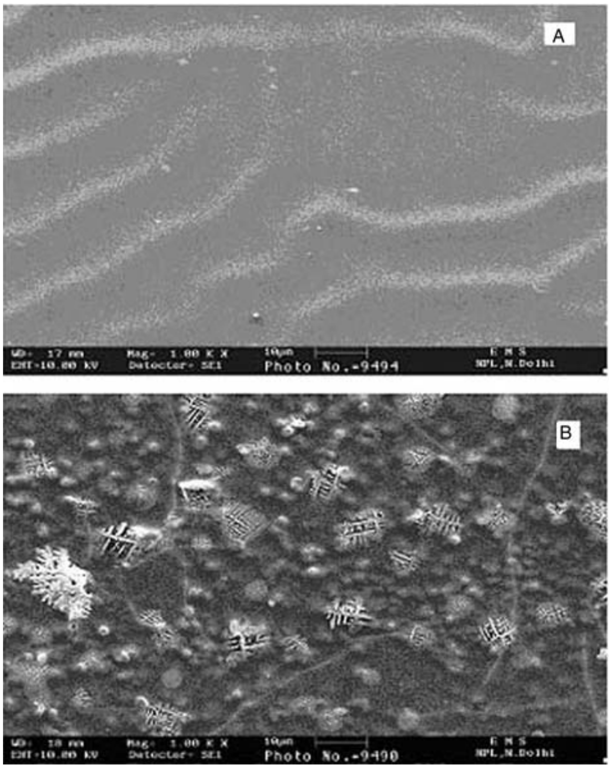

Figure 4. SEM picture of starch (A) and starch-graft-poly(acrylonitrile)(B)

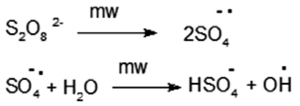

Figure 5. Generation of primary free radicals by $(NH_4)_2S_2O_8$ under microwave irradiation

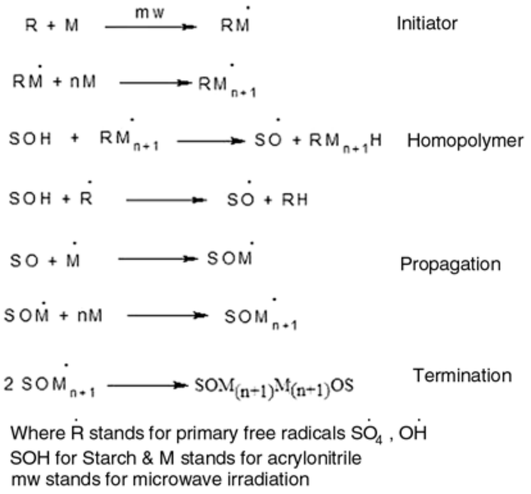

Figure 6. Graft copolymerization initiated by primary free radicals

$SO_4^{-\cdot}$ and $OH^{\cdot}$ are the primary radicals, generated in the above sequence of reaction, and are expressed as $R^{\cdot}$ in Figure 6. They initiate the vinyl polymerization as the vinyl polymerization is reported to be faster than the H abstraction from the polysaccharide starch backbone [5]. The macro radical ($SO^{\cdot}$) may be generated by abstraction of H by the growing vinyl polymer radical, which may add onto the vinyl monomer (M) generating new radical $SOM^{\cdot}$ and this chain will grow till it combines with other such chains to give the graft copolymer (Figure 6).

Since under identical reaction conditions, 0.0014 M persulfate could not initiate graft copolymerization in conventional grafting method (on thermostatic water bath) even at 98°C, some microwave effect cannot be ruled out in the microwave accelerated grafting procedure.

3.3. Determination of optimal grafting conditions under microwave irradiation

The microwave power, exposure time and concentration of the reactants (ammonium peroxydisulfate, acrylonitrile and starch) were varied keeping the total reaction volume fixed at 25 ml. The maximum grafting ratio and efficiency that could be reached were 225% and 98% respectively.

3.3.1. Effect of microwave power

On increasing microwave power from 240–1200 W, grafting ratio and efficiency increased (up to 1200 W microwave power) at fixed concentration acrylonitrile (0.17 M), $(NH_4)_2S_2O_8$ (0.0010 M), starch (0.1g), exposure time (30 sec) and reaction volume (25 ml) (Figure 7). Increase in %G and %E with increasing microwave power may be due to the formation of more $M^{\cdot}_n$ and $SO^{\cdot}$ radicals, resulting into more $SOM^{\cdot}_n$ radicals for graft co-polymerization.

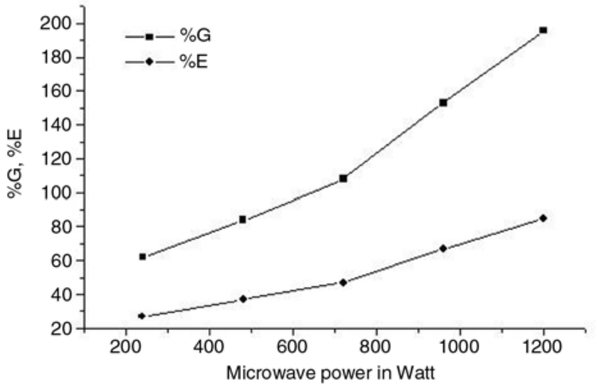

Figure 7. Effect of microwave power on %G and %E at $[(NH_4)_2S_2O_8]$·0.001 M; [acrylonitrile] 0.17 M; [starch] 0.1 g/25 ml and exposure time 30 sec

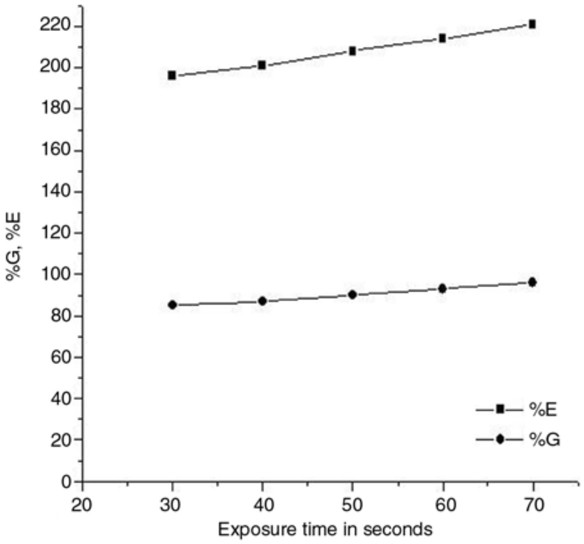

Figure 8. Effect of exposure time on %G and %E; at $[(NH_4)_2S_2O_8]$ 0.001 M; [acrylonitrile] 0.17 M; [starch] 0.1 g/25 ml and 1200 W microwave power

3.3.2. Effect of exposure time

Grafting increased with increase in exposure time and was most for 70 sec exposure at fixed concentration of acrylonitrile (0.17 M), $(NH_4)_2S_2O_8$ (0.0010 M), starch (0.1 g), microwave power (1200 W) and reaction volume (25 ml) (Figure 8). On increasing the exposure time, grafting ratio and efficiency increased. This may be due to the availability of more microwave energy resulting in to extra $SOM^{\cdot}_n$ radicals for the graft copolymerization.

3.3.3. Effect of monomer concentration

Grafting ratio increased on increasing the monomer concentration after 0.17 M; however efficiency decreases under the fixed concentration of starch (0.1 g/25 ml) at 1200 W microwave power and 70 sec exposure in 25 ml reaction volume (Figure 9). The increase in %G may be due to the formation of more $M^{\cdot}_n$, generating more grafting sites and due to availability of extra monomer for grafting. Decrease in efficiency on increasing the monomer concentration beyond 0.17 M may be probably due to more homopolymer formation.

3.3.4. Effect of ammonium peroxydisulfate concentration

The effect of ammonium peroxydisulfate on the copolymerization was studied in the concentration

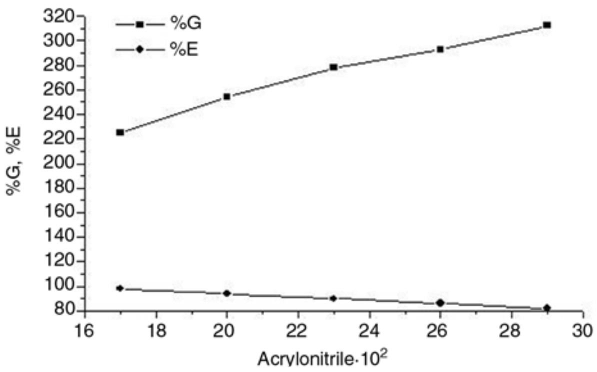

Figure 9. Effect of acrylonitrile concentration on %G and %E at [$(NH_4)_2S_2O_8$] 0.001 M: [starch] 0.1 g/25 ml: 1200 W microwave power and 70 seconds exposure

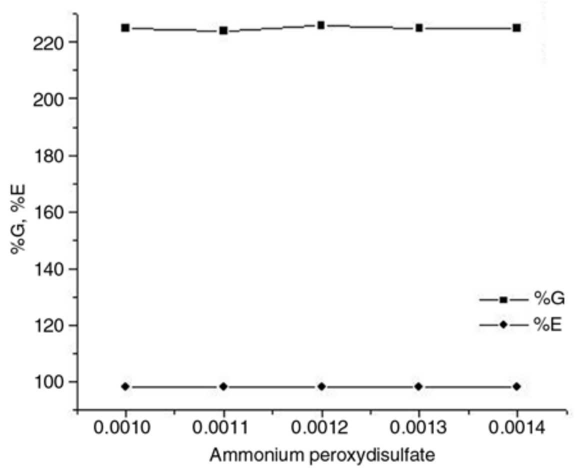

Figure 10. Effect of ammonium peroxydisulfate concentration on %G and %E at [acrylonitrile] 0.17 M; [starch] 0.1 g/25 ml; 1200 W microwave power and 70 seconds exposure

range 0.0010–0.0014 M at fixed concentration of acrylonitrile (0.17 M), starch (0.1 g/25 ml) at 1200 W microwave power and 70 sec exposure in 25 ml reaction volume (Figure 10). It was observed that the %G and %E was not significantly affected by change in peroxydisulfate concentration in the studied concentration range. This may be due to very fast reaction taking place under the influence of the microwaves so minor change in the initiator concentration does not affect grafting.

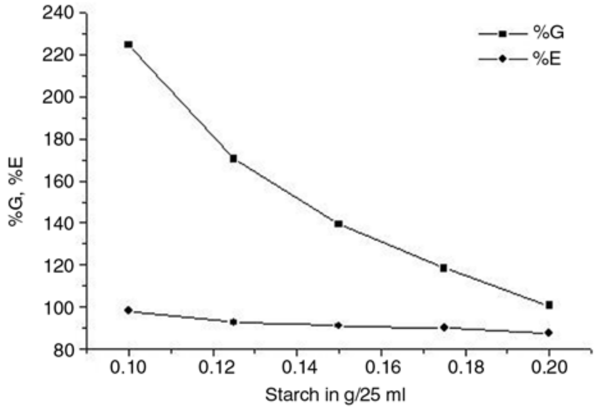

Figure 11. Effect of starch concentration on %G and %E at [$(NH_4)_2S_2O_8$] 0.0014 M, [acrylonitrile] 0.17 M, 1200 W microwave power and 70 sec exposure

3.3.5. Effect of starch concentration

The effect of Starch concentration was studied in the range of 0.1–0.2 g/25 ml at fixed concentration of ammonium peroxydisulfate (0.0014 M), acrylonitrile (0.17 M), microwave power (1200 W), exposure time (70 sec) and reaction volume (25 ml) (Figure 11). It was found that both %G and %E decrease with the increase in the concentration of starch, which may be due to the increase in the viscosity of the reaction medium causing hindrance of the normal reaction and also due to decrease in the monomer: starch ratio.

Overall maximum grafting ratio and efficiency that could be achieved was 225% and 98% respectively at 0.0014 M ammonium peroxydisulfate; 0.17 M acrylonitrile; 0.1 g/25 ml starch, 1200 W microwave power, 70 sec exposure keeping total reaction volume fixed at 25 ml.

3.4. Viscosity

Viscosity of 1% solution of starch, starch-graft-PAN (%G-225) and saponified starch-graft-PAN were found to be 0.008 Pas-s, 0.022 Pas-s and 0.203 Pas-s respectively (Table 1). The viscosity of the pure starch solution was found prone to biodegradation and its viscosity was lost slowly on

Table 1. Viscosity of starch, starch-graft-PAN and saponified starch-graft-PAN with time at 25°C

No.	Sample	%G	Viscosity of 1% solutions in Pas-s after different time intervals							
			Initial	8 h	12 h	24 h	48 h	86 h	128 h	250 h
1.	Starch	–	0.008	0.006	0.004	0.003	0.003	0.003	0.003	0.003
2.	S-g-PAN	225	0.022	0.022	0.022	0.022	0.022	0.022	0.022	0.022
3.	Saponified S-g-PAN	225	0.203	0.204	0.205	0.206	0.209	0.209	0.209	0.209

Where S-g-PAN stands for starch-graft-poly(acrylonitrile)

Table 2. Water and saline retention for starch, starch-graft-PAN and saponified starch-graft-PAN at 25°C

No.	Sample	%G	Water retention [g/g]	Saline (1% NaCl) retention [g/g]
1.	Starch	–	18.01	15.43
2.	S-g-PAN	225	11.93	8.17
3.	Saponified S-g-PAN	225	58.96	49.31

Where S-g-PAN stands for starch-graft-poly(acrylonitrile)

Table 3. %G and %E in microwave and conventional methods in atmospheric and inert conditions at different peroxydisulfate concentration using starch (0.1 g/25 ml), acrylonitrile (0.17 M), total reaction volume 25 ml

No.		Concentration Persulfate in M	Condition	Temperature in °C	%G	%E
1.	Microwave method	0.0014	Atmospheric	98	225	98
2.	Conventional method	0.0014	Atmospheric	50	Nil	Nil
		0.0014	N_2 atm	50	Nil	Nil
		0.0014	Atmospheric	98	Nil	Nil
		0.0014	N_2 atm	98	Nil	Nil
		0.014	N_2 atm	50	Nil	Nil
		0.028	N_2 atm	50	Nil	Nil
		0.14	N_2 atm	50	Nil	Nil
		0.24	N_2 atm	50	10	4

standing while the grafted and saponified grafted starch solutions retain their viscosity even after 250 h (Table 1).

3.5. Water retention and saline retention

The water retention property is due to the interaction of the hydroxyl groups of the starch through hydrogen bonding. The grafting of the vinyl monomers onto the starch occurs through the hydroxyl groups of its backbone thereby decreasing the number of available hydroxyl groups for water and saline retention. Thus water and saline retention ability of the graft copolymer proportionally decrease with the increase in the grafting ratio (Table 2 and 3). On hydrolysis with aqueous alkali, the –CN groups on the grafted chains get hydrolyzed to $-CONH_2$ and –COOH groups and this increases water-binding sites in the saponified starch-graft-PAN and thereby a larger volume of water is bonded.

4. Conclusions

Starch-graft-PAN was synthesized in very short time using low ammonium peroxydisulfate concentration under microwave irradiation and for grafting removal of oxygen from the reaction vessel was not required. The highest grafting ratio (225%) and efficiency (98%) were found at 0.17 M acrylonitrile; 0.0014 M ammonium peroxydisulfate; 0.1 g starch, 1200 W microwave power and 70 sec exposure keeping total reaction volume fixed at 25 ml. On grafting viscosity and shear stability of starch solutions increase while water and saline retaining ability decrease.

Acknowledgements

Authors are thankful to Department of Science and Technology, New Delhi, India for generous financial support to carry out this work.

References

[1] Athawale V. D., Lele V.: Graft copolymerization onto starch. 3: Grafting of acrylamide using ceric ion initiation and preparation of its hydrogels. Starch-Starke, **50**, 426–431 (1998).

[2] Pourjavadi A., Zouhuriaan-Mehr M. J.: Modification of carbohydrate polymers via grafting in air. 1. Ceric-induced synthesis of starch-g-polyacrylonitrile in presence and absence of oxygen. Starch-Starke, **54**, 140–147 (2002).

[3] Singh V., Tiwari A., Tripathi D. N., Sanghi R.: Microwave assisted synthesis of guar-g-polyacrylamide. Carbohydrate Polymers, **58**, 1–6 (2004).

[4] Singh V., Tiwari A., Tripathi D. N., Sanghi R.: Microwave promoted synthesis of chitosan-grafted-polyacrylamide. Polymer, **47**, 254–260 (2006).

[5] Singh V., Tiwari A., Sanghi R.: Studies on $K_2S_2O_8$/ascorbic acid initiated synthesis of Ipomoea dasysperma seed gum-g-poly(acrylonitrile): A potential industrial gum. Journal of Applied Polymer Science, **98**, 1652–1662 (2005).

[6] Singh V., Tiwari A., Tripathi D. N., Sanghi R.: Poly(acrylonitrile) grafted Ipomoea seed-gums: a

renewable reservoir to industrial gums. Biomacromolecules, **6**, 453–456 (2005).

[7] Athawale V. D., Rathi S. C., Lele V.: Graft copolymerization on to maize starch. I. Grafting of methacrylamide using ceric ammonium nitrate as an initiator. European Polymer Journal, **34**, 159–162 (1998).

[8] Singh V.: Poly(acrylonitrile)grafted Cassia pudibunda seed gum: a potential commercial gum from renewable source. Journal of Applied Polymer Science, **99**, 619–627 (2006).

[9] Lutfor M. R., Rahman M. Z. A., Sidik S., Mansor A., Haron J., Yunus W. M. Z. W.: Kinetics of graft copolymerization of acrylonitrile onto sago starch using free radicals initiated by ceric ammonium nitrate. Designed Monomers and Polymers, **4**, 253–260 (2001).

[10] Fanta G. F., Felker F. C., Shogren R. L.: Graft polymerization of acrylonitrile onto spherocrystals formed from jet cooked cornstarch. Carbohydrate Polymers, **56**, 77–84 (2004).

[11] Geresh S., Gilboa Y., Peisahov-Korol J., Gdalevsky G., Voorspoels J., Kost J.: Preparation and characterization of bioadhesive grafted starch copolymers as platforms for controlled drug delivery. Journal of Applied Polymer Science, **86**, 1157–1162 (2002).

[12] Hebeish I., Abd El-Thalouth I., El-Kashouti M. A., Abdel-Fattah S. H.: Graft copolymerization of acrylonitrile onto starch using potassium permanganate as initiator. Angewandte Makromolekulare Chemie, **78**, 101–108 (2003).

[13] Sugahara Y., Ohta T.: Synthesis of starch-graft-polyacrylonitrile hydrolyzate and its characterization. Journal of Applied Polymer Science, **82**, 1437–1443 (2001).

[14] Taylor N. W., Fanta G. F., Doane W. M., Russell C. R.: Swelling and rheology of saponified starch-g-polyacrylonitrile copolymers. Effect of starch granule pretreatment and grafted chain length. Journal of Applied Polymer Science, **22**, 1343–1357 (1978).

[15] Galema S. A.: Microwave chemistry. Chemical Society Reviews, **26**, 233–238 (1997).

[16] Deshayes S., Liagre M., Loupy A., Luche J. L, Petit A.: Microwave activation in phase transfer catalysis. Tetrahedron, **55**, 10851–10870 (1999).

[17] Loupy A., Petit A., Hamelin J., Texier-Boullet F., Jacquault P., Mathe D.: New solvent free organic synthesis using focused microwaves. Synthesis-Stuttgart, **9**, 1213–1234 (1998).

[18] Varma R. S.: Solvent-free organic synthesis using supported reagents and microwave irradiation. Green Chemistry, **1**, 43–55 (1999).

[19] Kappe C. O.: Controlled microwave heating in modern organic synthesis. Angewandte Chemie-International Edition, **43**, 6250–6284 (2004).

[20] Singh V., Tiwari A., Pandey S., Singh S. K.: Microwave accelerated synthesis and characterization of potato starch-g-poly(acrylamide). Starch-Starke, **58**, 536–543 (2006).

[21] Cheng Z. P., Zhu X. L., Chen M., Chen J. Y., Zhang L. F.: Atom transfer radical polymerization of methyl methacrylate with low concentration of initiating system under microwave irradiation. Polymer, **44**, 2243–2247 (2003).